All-Optical Ultrasound Transducers for High Resolution Imaging

A Thesis
SUBMITTED TO THE FACULTY OF
UNIVERSITY OF MINNESOTA
BY

Clay Smith Sheaff

IN PARTIAL FULFILLMENT OF THE REQUIREMENTS
FOR THE DEGREE OF
DOCTOR OF PHILOSOPHY

Shai Ashkenazi, Adviser

December 2014

Acknowledgements

I would like to begin by expressing my gratitude to Dr. Shai Ashkenazi for taking me on as his first student. Prior to our meeting, I had little idea of what path was right for me. At the last second of my visit to UMN, we had an impromptu chat about his research. It struck such a chord that afterwards I felt a security not experienced in years. Had that meeting not occurred or had I not been so accepted, I cannot imagine that the past six years would have been much less tumultuous than the previous three. I would also like to thank Dr. Ashkenazi for his patience, insight, and guidance during my time here at UMN. I consider the general problem-solving skills adopted as his understudy to be the most valuable asset attained in my graduate school career. Most importantly, I thank him for his genuine interest in the well-being of his students. It is easily assumed that a cordial and accomplished adviser is necessarily a supportive one. I consider myself lucky to have been advised by someone who is truly all three.

Secondly, I would like to thank my committee members, past and present, for their time in reviewing my work. They include Dr. Taner Akkin, Dr. Emad Ebbini, Dr. David Hunter, and Dr. James Leger.

Departmental and technical staff have been immeasurably helpful. I thank Rachel Jorgenson for her general advisement and her cheerful and reliable assistance with all things bureaucratic. I have also appreciated the staff of the Minnesota Nano Center, particularly Lage von Dissen, who never fails to be interested and helpful.

The support of friends gained along the way has been invaluable. To my comrades Ekaterina Morgounova and Mohammad Amin Tadayon, you have my gratitude for your assistance both inside and outside of the lab. From proofreaders to mock therapists, I would not have been as published or even-tempered without you. I cannot begin to thank Daisy Cross and her husband Nathan Lockwood for offering friendship that I will always hold dear. When it comes to tolerating bitterly cold winters, their inviting home has made the difference.

To my family, I thank my Aunt and Uncle Sinclair for always keeping their door open to me. They provided the slice of home that at times I so desperately needed. To my sisters Kim and Kelly, thank you for making such squeezable little rug rats whom have consistently brightened my return to the heartland. And certainly most of all, I thank my parents. I am confident that I would not have made it this far without the drive instilled in me by my father and the loving care so unwaveringly provided by my mother. Any virtues that I possess, I owe to them both.

Lastly, I extend a handshake to myself. Congratulations sir. Given the circumstances, you have done the impossible. You know of what I speak and always will.

.

Table of Contents

List of Figures

List of Tables

List of Abbreviations

Au	Gold
Au/Au	PI-etalon with PI/Au/SU-8/Au layers
BS	Beam Splitter
CCD	Charged-coupled device
CMUT	Capacitive Micromachined Ultrasound Transducer
CT	Computed Tomography
CW	Continuous Wave
DAQ	Data Acquisition
Die	Dielectric
Die/Au	PI-etalon with PI/Die/PI/Au layers
FIR	Finite Impulse Response
FOC	Fiber Optic Circulator
FPS	Frames Per Second
FSR	Free Spectral Range
FWHM	Full-width half-maximum
HFUS	High Frequency Ultrasound
IVUS	Intravascular Ultrasound
MEMS	Micro-electro-mechanical Systems
MM	Multi-mode
MRI	Magnetic Resonance Imaging
NA	Numerical Aperture
NEP	Noise-equivalent Pressure
NIR	Near-infrared
OS	Optical Switch
PAI	Photoacoustic Imaging
PAE	Photoacoustic Endoscopy
PBS	Polarizing Beam Splitter
PD	Photodetector
PDMS	Polydimethylsiloxane
PI	Polyimide
PRF	Pulse Repetition Frequency

PXI	PCI eXtensions for Instrumentation
SAFT	Synthetic Aperture Focusing Technique
SM	Single Mode
SNR	Signal-to-Noise Ratio
TUG	Thermoelastic Ultrasound Generation
UV	Ultraviolet

Chapter 1

Introduction

1.1 Clinical Significance of High Frequency Ultrasound

Within the past few decades, high frequency ultrasound (HFUS) (> 20 MHz) has increasingly been used to provide high resolution (< 200 µm) imaging in medical applications such as endoluminal imaging, intravascular imaging, ophthalmology, and dermatology. While clinical magnetic resonance imaging (MRI) and X-ray computed tomography (CT) systems continue to approach these resolutions (3T MRI scanners ~ 500 µm [1], CT ~ 400 µm [2]-[3]), their expense, safety, and bulkiness make them non-ideal candidates for routine interventional procedures. Furthermore, their limited temporal resolution – typically below a few frames per second (FPS) – inhibits the effective imaging of moving structures, guidance of interventional therapies, and rapid diagnosis of disease. The majority of ultrasound imaging systems are both portable and safe (no ionizing radiation), and they produce frame rates exceeding 25 FPS – the approximate threshold for real-time operation. Optical Coherence Tomography (OCT) can also provide real-time imaging and with better spatial resolution (< 10 µm) than ultrasound, however HFUS allows for larger penetration depth (~ 10 mm) and hence a larger field of view than OCT (< 1 mm). Photoacoustic imaging (PAI) has also derived from ultrasound technology – a modality wherein tissue is irradiated with high energy laser pulses to produce HFUS. This method combines the penetration depth of ultrasound with optical absorption contrast to differentiate between tissue types and map metabolic activity.

Due to the relatively limited field-of-view, clinical HFUS applications are either superficial or endoscopic. In the imaging of superficial structures, a single transducer is typically scanned across a linear or arced path that is parallel with the sample. Ultrasound Biomicroscopy (UBM) is the most notable example – a modality that can image the anterior structures of the eye in order to assess trauma, melanomas, glaucoma, and other ocular diseases [4]. Commercial UBM systems operate as high as 50 MHz (Optos

OTI-Scan 3000, Quantel Medical Aviso), but an experimental system using a 200 MHz transducer has been demonstrated [5]. Systems similar to those of UBM have been used to image pathologies of the skin, but only in a research environment. Examples of clinical studies include measuring the thickness of the dermis, examining cutaneous lesions, and assessing the depth and margins of skin tumors [4].

The spatial constraints imposed by lumens and arteries in endoscopic applications make the scanning of a single transducer across a linear path very difficult. Rotation of an outward facing transducer, or radial scanning, is therefore typically employed. Applications include searching for lesions in the wall layers of the gastrointestinal (GI) tract as well as the biliary/pancreatic ducts, with commercial devices operating as high as 25-30 MHz (Fujifilm P2625-M, Olympus UM-S30-20R). A modality under wide-spread investigation is side-viewing intravascular ultrasound (IVUS), which is used to observe the extent and composition of atherosclerotic plaque buildup in coronary and peripheral arteries. Commercial IVUS systems operate as high as 40-45 MHz (Volcano Revolutions, Boston Scientific Atlantis SR Pro), and experimental devices functioning as high as 80 MHz have been reported [6], [7]. In order to look in front of the catheter as opposed to the side, radially-scanning IVUS probes have been modified such that a conical mirror deflects the acoustic emission in the forward direction [8]. Known as forward-viewing/looking IVUS, this modality would allow characterization of occlusions without the need for penetration, which can restrict blood flow and increase the risk for ischemia. Forward-facing transducers have also been implemented for this purpose, relying on the rocking/tilting of a single element to perform a sector scan [9].

1.2 Endoscopic Transducer Arrays

The disadvantages of scanning a single element in an endoscopic environment include a fixed focus and the inability to employ beam-forming. As a result, there is a non-uniform depth of field with limited circumferential resolution in the case of radial scanning and limited lateral resolution when looking forward (> 200 µm). Furthermore, the inclusion of moving parts presents fabrication difficulties, adds bulk, and reduces flexibility. In the case of forwarding-facing transducers, this effectively disqualifies its use within the coronary arteries where the identification of vulnerable plaque is the most critical. Finally,

mechanical scanning can introduce image artifacts due to the non-uniform velocity of the scanning mechanism. This results from the mechanical strain induced by the bending of the device when inside the body [10].

The development of endoscopic phased arrays in order to compensate for the shortcomings of scanned transducers is extensive and ongoing. Cylindrical phased arrays have been employed as an alternative to radial scanning so as to eliminate the rotational mechanism, thereby providing more uniform resolution through dynamic focusing (Figure 1.1) [11]. A ubiquitous IVUS system using a cylindrical array is the Volcano Eagle Eye, which consists of 64 line elements circumferentially distributed about a 1.7 mm catheter, operating at 20 MHz. Several array configurations have also been developed for forward-looking IVUS. The most promising development to date is a 20 MHz, 1.4 mm array consisting of two concentric ring arrays of capacitive micromachined ultrasound transducers (CMUT) – one for transmitting and the other for receiving (Figure 1.2a) [12]. Linear arrays making use of the entire face of the catheter have also been developed, however the resultant gain in contrast comes at the expense of frequency response; linear arrays small enough for IVUS applications rarely exceed 10 MHz (Figure 1.2b) [13].

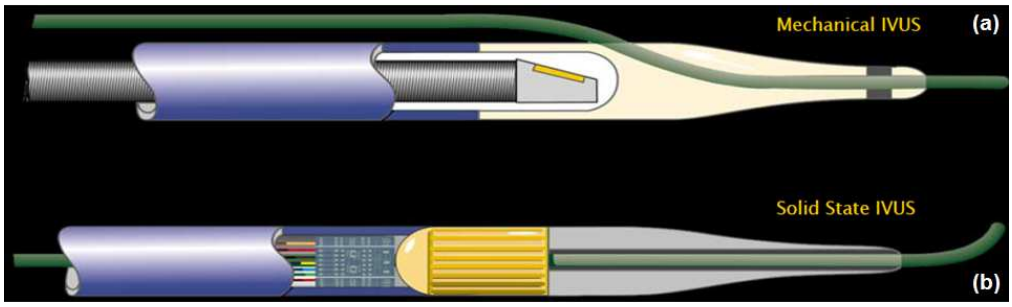

Figure 1.1. Side-looking IVUS using **(a)** single-element rotation and **(b)** a cylindrical phased array. A phased array avoids a rotational mechanism, provides beam forming, and allows a coaxial guidewire (Image by Boston Scientific).

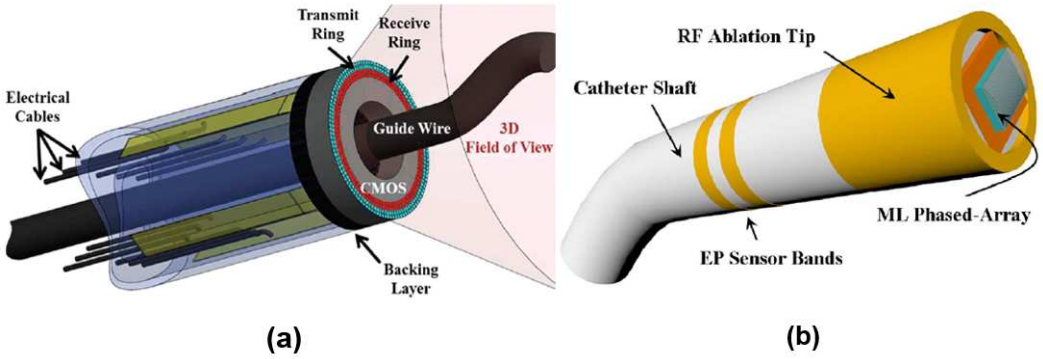

Figure 1.2. Designs for forward-looking IVUS imagers: **(a)** dual-ring CMUT array with hollow center for a guidewire [12] (© 2014 IEEE) and **(b)** a 1-D linear array combined with a mechanism for intracardiac RF ablation [13] (© 2008 IEEE).

Despite the broad appeal of ultrasound imaging, there exists a disconnect between commercial systems and high frequency operation. With respect to conventional piezoelectric ceramics and composites, dice-and-fill techniques used to fabricate transducers on the size scale required for high frequency transduction (< 100 μm) become difficult to implement. The development of thin film polyvinylidene fluoride (PVDF) and CMUTs has to some extent circumvented this problem, however these devices are still susceptible to the small scale effects found in traditional piezoelectric devices. Such effects include a lowered electromechanical coupling factor, increased noise due to small element capacitance, electrical crosstalk between channels, and RF interference. This often necessitates front-end electronics in small probes already dense with circuitry, which ultimately limits the ability to implement dense arrays of HFUS elements in a beam-forming capacity.

1.3 Optical Ultrasound Transduction

1.3.1 Etalon Receivers

1.3.1.1 Introduction

In concept, the optical detection and generation of HFUS using thin films offers numerous advantages over traditional piezoelectric technology. Circumvention of an

electronic interface with the device head is one of the most significant given the aforementioned problems that encumber small-scale electronic transducers. The prospect of using optical fibers as the sole means of communication with the imaging head raises the likelihood of meeting the size and flexibility requirements of endoscopic and intravascular devices. Furthermore, the active area of an optical element is determined by the optical spot size, therefore transducers on the order of 10 µm can be easily obtained by focusing the probe beam without any loss in sensitivity. Finally, arrays of all-optical elements can be easily formed either by multiple-beam interrogation or laser scanning.

Thin film Fabry-Perot interferometers – also known as etalons – are well suited for HFUS receivers on account of their high sensitivity, wide bandwidth, and ease of fabrication [14]-[16]. These devices consist of a thin and compressible optical resonator which, when exposed to acoustic waves, undergo a change in cavity thickness. As a result, the optical path length in the cavity is modulated. Because the resonance condition is dependent on this measure, the resonance wavelength will shift in response to this modulation (Figure 1.3). If the beam used to probe the etalon is programmed at a wavelength that falls on an edge of the resonance, a corresponding change in the intensity of that beam's reflection can be observed. To understand the key parameters that determine device performance, we turn to a theoretical analysis of etalon operation.

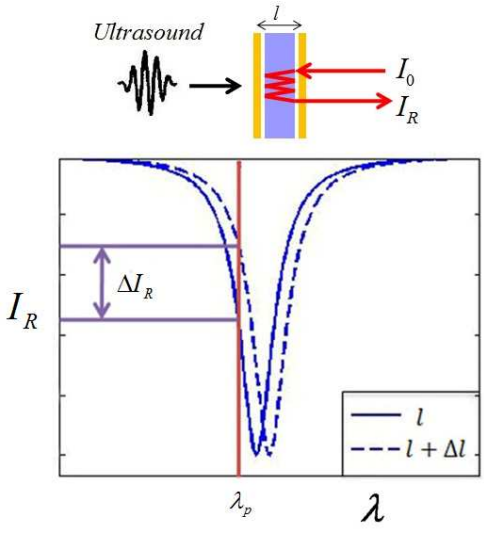

Figure 1.3. Mechanism for optical detection of ultrasound with a thin film etalon. Pressure from acoustic waves modifies the cavity thickness, $\boldsymbol{l}$, of a Fabry-Perot interferometer (etalon). When the reflected intensity of a probing beam is monitored, shifts in resonance wavelength occur due to an alteration in thickness, $\Delta\boldsymbol{l}$. If the input beam is programmed at a fixed wavelength, $\boldsymbol{\lambda_p}$, which occurs on a falling or rising edge of the resonance curve, a change in reflected intensity, $\boldsymbol{\Delta I_R}$, is observed due to this shift [17] (© 2010 IEEE).

1.3.1.2 Theoretical Model of Etalon Detection

The reflected intensity of the etalon probe beam can be expressed using an Airy function:

$$I_R = I_0\left(1 - \frac{1}{(2F/\pi)^2\, sin^2(\phi/2)}\right) , \qquad \text{(Eq. 1.1)}$$

where

$$\phi = \frac{4\pi nl}{\lambda}.$$

given normal incidence with intensity I_0, l as the etalon thickness, and n the index of refraction of the material between the mirrors. The coefficient F is defined as the optical finesse – a parameter indicating the sharpness of resonance. It can be expressed as

$$F = \frac{\pi \exp(-\alpha_r l/2)}{1 - \exp(-\alpha_r l)} , \qquad \text{(Eq. 1.2)}$$

where α_r is the energy loss coefficient of the cavity. Among other means, loss can result from optical absorption/scattering by the etalon material and the imperfect reflectivity of the mirrors. In this case

$$\alpha_r = \alpha_s + \frac{1}{2l}\ln\frac{1}{R_1 R_2} , \qquad \text{(Eq. 1.3)}$$

where α_s is the absorption/scattering coefficient and R_1 and R_2 are the respective reflectivities of the two mirrors, which can take on a value between 0 and 1. Substituting Equation 1.3 into Equation 1.2 when $\alpha_s = 0$ yields

$$F = \frac{\pi(R_1 R_2)^{1/4}}{1 - \sqrt{R_1 R_2}} .$$

Figure 1.4 shows the theoretical resonance plot for I_R/I_0 of Equation 1.1 versus λ for two different values of finesse in the case that $R_1 = R_2 = R = 0.95$, $n = 1.6$ and $l = 10\,\mu m$. A higher finesse results in a sharper resonance and is therefore preferable in order to maximize acoustic sensitivity. Note that

$$\lim_{R \to 1^-} F(R) = \infty .$$

Thus, finesse monotonically increases with mirror reflectivity.

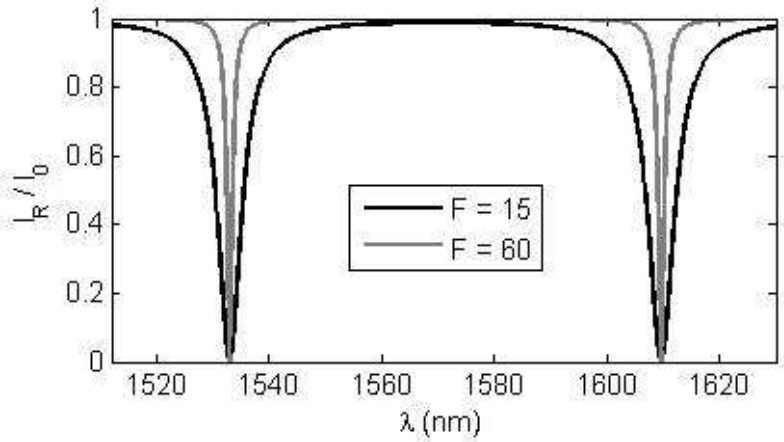

Figure 1.4. Theoretical resonance curves for two etalons of different optical finesse ($\boldsymbol{R = 0.95}$, $\boldsymbol{n = 1.6}$, and $\boldsymbol{l = 10\mu m}$).

Other characteristics of the optical system used also affect acoustic sensitivity. Hamilton et al. demonstrated that the signal of interest in the reflected intensity can be expressed as

$$I_{sig}(t) = \frac{1}{4} I_0 + \frac{9 I_0}{2\sqrt{3}} \left[\frac{Fn\Delta l(t)}{\lambda} \right] ,$$

where Δl is the time-varying change in the thickness of the etalon cavity due to the incident acoustic pressure [14]. It was also shown that the overall signal-to-noise ratio (SNR) after measurement by a photodetector (PD) becomes

$$SNR = \frac{\langle i_{sig}^2 \rangle}{i_{DC}^2} = \frac{27 S P_0}{4qB} \left(\frac{Fn\Delta l}{\lambda} \right)^2 , \qquad \text{(Eq. 1.4)}$$

where i_{sig}^2 is the signal current, S is the detector sensitivity in A/W, P_0 is the power of the incident beam, q is the charge of an electron, and B is the optical detection bandwidth. If we consider the time-varying acoustic pressure as a source of tensile stress that creates extensional strain, the modulus of the material is defined as

$$E = \frac{F/A}{\Delta l / l} = \frac{p_i}{\Delta l / l} ,$$

where A is the area of the applied force F, and p_i is the incident pressure. The change in etalon thickness then becomes:

$$\Delta l(t) = \frac{p_i(t) l}{E} ,$$

which can be substituted into Equation 1.4 to arrive at

$$SNR \propto \frac{SP_0}{B}\left(\frac{Fnp_i l}{\lambda E}\right)^2 . \qquad \text{(Eq. 1.5)}$$

The frequency response of the etalon as an acoustic receiver is primarily limited by the mechanical properties of the polymer film. We can think of the film attached to a substrate as a harmonic oscillator with spring constant k and frequency ω. In the case of fixed, elastic media of density ρ, we have

$$k = \frac{EA}{l} .$$

The central frequency (resonance) of the oscillator is then

$$f_c = \frac{1}{2\pi}\sqrt{\frac{k}{m}} = \frac{1}{2\pi l}\sqrt{\frac{E}{\rho}} . \qquad \text{(Eq. 1.6)}$$

A tradeoff therefore exists between SNR and f_c when changing the cavity thickness or modulus. Table 1.1 shows device parameters for three etalons reproduced from Wang et al [18]. As predicted, detection sensitivity decreases with decreased thickness among the two SU-8 etalons, but the central frequency increases. The influence of Young's Modulus on sensitivity is also demonstrated by comparing etalons made with SU-8 and polydimethylsiloxane (PDMS). A substantially decreased modulus results in increased compressibility, hence increased sensitivity. However, bandwidth is severely reduced, therefore a smaller thickness is required to match the frequency response of SU-8 etalons. For additional review of operational principles governing ultrasonic detection using thin film etalons, see [19].

Material	**SU-8**	**SU-8**	**PDMS**
E (GPa)	4.4	4.4	0.6
l (μm)	10	5	3
Detection area diameter (μm)	20	20	20
Sensitivity (W/MPa)	0.072	0.056	0.16
NEP (kPa)	2.8	3.8	1.3
f_c (MHz)	30	60	40
-6dB Bandwidth (MHz)	30	> 50	> 50

Table 1.1 Comparison of device parameters for three different etalons [18]. Etalon mirrors were 30 nm Au. Bandwidth was determined experimentally (NEP: Noise-equivalent pressure. f_c: theoretically determined central frequency).

1.3.2 Integrated All-optical Transducers

1.3.2.1 Introduction

Thin films can also be used to generate HFUS when irradiated with optical pulses – a method referred to as Thermoelastic Ultrasound Generation (TUG). In TUG, the rapid absorption of optical energy in the material induces a thermoelastic wave. This results in the launching of an acoustic wave with temporal characteristics directly related to the shape of the optical pulse. Highly photoabsorptive targets that have been developed for this purpose include simple metallic thin films (aluminum, chromium) [20]-[24], graphite-polymer mixtures [25], [26], elastomer films mixed with black dyes [27], [28], periodic gold nanostructures [29], and carbon nanotube-polymer composites [30]. Of these films, it is conceivable that those which can be fabricated with moderate ease are able to be integrated into etalon structures so as to provide an all-optical transducer. It is also useful to choose films that are dichroic in nature. By operating at two sufficiently distinct wavelengths, the two modes of transduction could function independently.

1.3.2.2 Previous Designs for All-optical Transducers

Hou et al. were the first to create an all-optical transducer by modifying a PDMS etalon with two gold mirrors [31], [32]. The mirror closest to the substrate was replaced with a periodic gold nanostructure that, when irradiated at the structure's plasmon resonance wavelength, conducts heat to the PDMS layer which in turn generates TUG (Figure 1.5a). The nanostructure is then capable of reflecting one wavelength and absorbing another. The disadvantages of using the gold nanostructure were determined to be poor conversion efficiency – only 30 % absorption at the excitation wavelength – and substantial transmittance at this wavelength to the etalon layers – approximately 20 %. As a result, high intensities are required for ultrasound generation using this configuration, and a significant portion of the incident energy is transmitted to the etalon thereby damaging the receiver and making long term use unviable. In addition, modification of the etalon mirror makes it less reflective at the probe beam wavelength resulting in lower detection sensitivity.

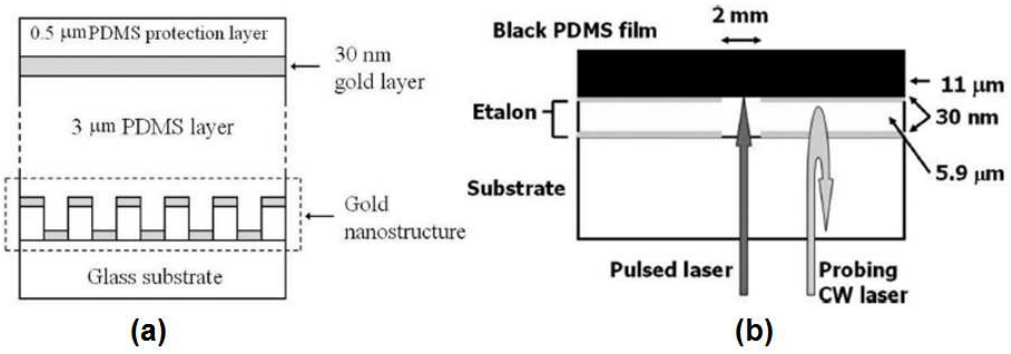

As an alternative, Hou et al. deposited a carbon black-PDMS mixture on top of a standard etalon. Hence, the absorbing layer was changed to a polymer and segregated from the etalon layers (Figure 1.5b). The disadvantage of this orientation is that the etalon mirrors must now be highly transparent ($R < 0.01$) at wavelengths used for TUG, otherwise thermal damage easily occurs. This was circumvented by patterning the etalon mirrors such they left an aperture through which the pulse could propagate [33]. Imaging of 50 μm metal wires was then performed by scanning the TUG beam in a line through this aperture and scanning the etalon beam around the aperture as shown in Figure 1.6a. Using an integrated transmit-receive device, the reconstruction in Figure 1.6b represents the best imaging result prior to the work presented in this thesis – a poor target reconstruction at a low dynamic range (10 dB). Hou et al. attributed this result to not being able to form fully-sampled 2-D arrays. Because receiving and transmitting elements cannot reside in the same location, one is only allowed a partial imaging aperture, which yields poor spatial resolution and contrast.

1.3.2.3 PI-etalon for All-optical Ultrasound Transduction

In this work, we have built upon the efforts of Hou et al. by integrating a polyimide (PI) film into an etalon sensor (Figure 1.7). PI films are (1) easily fabricated with a thickness on the order of microns, (2) highly photoabsorptive in a narrow and readily attainable spectrum, and (3) highly transparent to wavelengths used for etalon sensing. The first

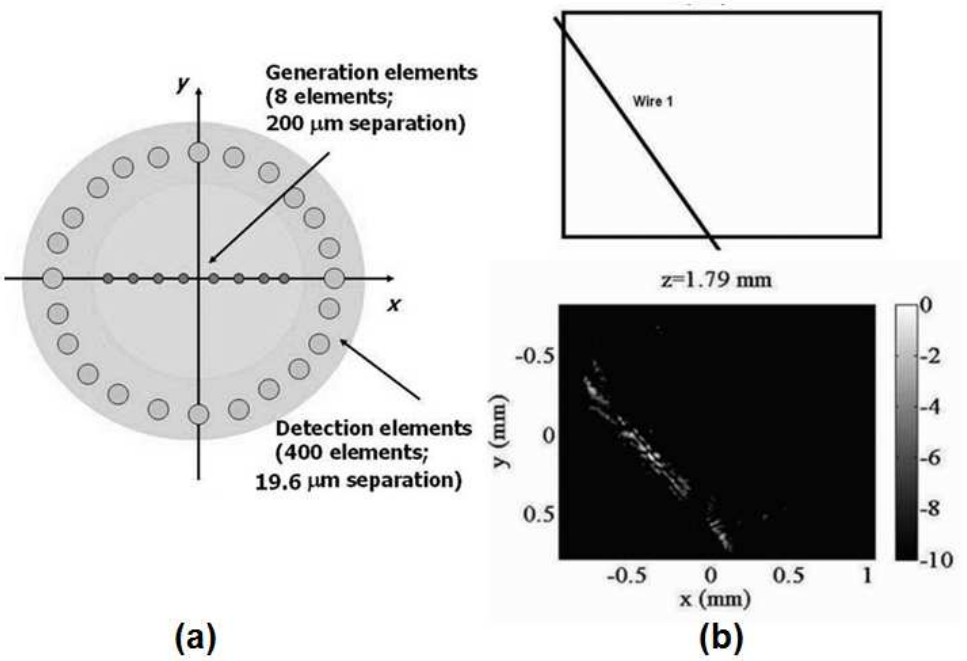

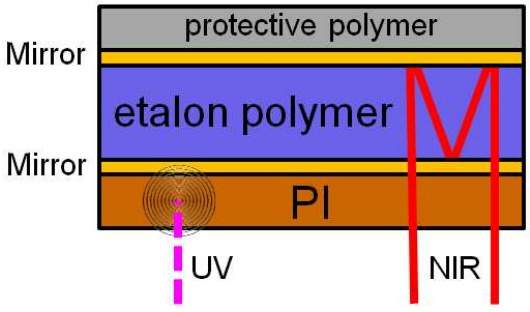

feature allows minimal addition to overall device thickness thereby preserving sensing bandwidth. Provided that the PI film is placed underneath the etalon, the second feature prevents the majority of the pulse energy for TUG from being transmitted to the receiver, which ensures a high damage threshold. The third feature allows sensing and transmitting elements to be in the same location, again, given that the TUG film is placed below the etalon. As a result, fully sampled 2-D arrays of arbitrary configuration are

allowed through either multiple-beam interrogation or beam scanning. We have achieved our aims using polyimide PI-2555/2525 (HD Microsystems) – a material known for its resistance to high temperatures and characteristic absorption in the UV spectrum [34]. Its mechanical and thermal properties along with those of other materials used in this work are presented in Table 1.2. Being able to use a polymer film instead of a metal for TUG takes advantage of their higher thermoelastic expansion coefficient and significantly lower heat conductivity.

Material	$\boldsymbol{\rho}$ (kg/m^3)	$\boldsymbol{v_a}$ (m/s)	$\boldsymbol{\beta}$ $(\mu m/m/K)$	$\boldsymbol{C_P}$ $(J/kg/K)$	$\boldsymbol{K}$ $(W/m/K)$	$\boldsymbol{E}$ (GPa)
Gold	19300	2030	14.2	129	318	79
Chromium	7200	5940	5	449	93.9	280
SU-8 2000	1187	2500	52	1500	0.3	4.4*
PI-2555/2525	1420	2620	40	1089	0.146	> 4.4*

1.3.2.4 Theoretical Model of TUG in Optically Thick Films

A theoretical expression relating the pressure generated during TUG to the incident laser intensity is found by combining the thermoelastic wave equation (Equation 1.7) – the inhomogeneous wave equation for pressure, p, assuming a temperature rise, T – with the heat equation assuming the laser pulse as a heat source with heating function, H (Equation 1.8). Specifically,

$$\left[\nabla^2 - \frac{1}{v_a^2}\frac{\partial^2}{\partial t^2}\right]p = -\frac{\alpha}{v_a^2}\frac{\partial^2 T}{\partial t^2} \ , \qquad \text{(Eq. 1.7)}$$

$$\frac{\partial T}{\partial t} = \frac{K}{\rho C_P}\nabla^2 T + \frac{H}{\rho C_P} \ , \qquad \text{(Eq. 1.8)}$$

where v_a is the material's speed of sound, $\alpha = \partial P/\partial T|_V$, ρ is the material density, C_P is the isobaric specific heat, and K is the thermal conductivity [35]. The specific heat ratio is assumed to be unity. In the case of a thin film as the optical medium, the thermal relaxation time of the material is defined as

$$\tau_{th} = \frac{l^2}{d_{th}} = \frac{l^2 \rho C_P}{K} \ ,$$

where d_{th} is the thermal diffusivity [36]. If the pulse width of the laser used for TUG, τ_p, is much smaller than τ_{th}, thermal confinement is assumed, resulting in K being negligible during the pulse. Equation 1.8 then becomes

$$\frac{\partial T}{\partial t} = \frac{H}{\rho C_P} ,$$

which can be substituted into Equation 1.7, yielding

$$\left[\nabla^2 - \frac{1}{v_a^2}\frac{\partial^2}{\partial t^2}\right] p = -\frac{\beta}{C_P}\frac{\partial H}{\partial t} , \qquad \text{(Eq. 1.9)}$$

after using the thermodynamic relation $\alpha = \rho v_a^2 \beta$ where $\beta = (1/V)\partial V/\partial T|_P$.

Because we have chosen PI as our material for TUG, we consider films with a thickness in the range of 1-15 μm, which cannot be considered optically thin. In other words, the film thickness is not substantially less than the optical penetration depth, and absorption is therefore non-uniform in the depth dimension. Shan et al. solved the 1-D form of Equation 1.9 for the pressure generated in a thick film by a laser pulse using the model

$$H(x,t) = I_0 \mu_a e^{-\mu_a x}\delta(t) ,$$

where μ_a is the optical absorption coefficient and $\delta(t)$ – the Dirac impulse function – approximates the temporal profile of the laser pulse [37]. The pressure waveform propagating forward, i.e. away from the incident pulse, includes (1) the initial wavefront followed by (2) the inverted reflection off of the rear film surface. Further reflections create additional pairs of these signals. Specifically, the ith pair is

$$p_i = \begin{cases} D\left[e^{-v_a\mu_a(t_1+l/v_a)} + e^{v_a\mu_a(t_1-l/v_a)}\right], & 0 \le t_1 < \dfrac{l}{v_a} \\ D\left[\left(\dfrac{v_b\rho_b - v_a\rho_a}{v_b\rho_b + v_a\rho_a}\right)e^{-v_a\mu_a(t_1-l/v_a)} + e^{-v_a\mu_a(t_1+l/v_a)}\right], & \dfrac{l}{v_a} \le t_1 < \dfrac{2l}{v_a} \\ 0, \quad else \end{cases} \qquad \text{(Eq. 1.10)}$$

where

$$t_1 = t - \frac{[2(i-1)h]}{v_a} - \frac{x}{v_b} ,$$

and

$$D = \frac{\mu_a \beta I_0 v_a^2}{C_P}\left(\frac{v_b\rho_b}{v_b\rho_b + v_a\rho_a}\right)\left(\frac{\rho_b v_b - \rho_a v_a}{\rho_a v_a + \rho_b v_b}\right)^{2(i-1)} .$$

v_b and ρ_b are the speed of sound and density of the medium between the film and the detector. The cumulative waveform is then the concatenation of all pairs

$$p = \sum_{i}^{N} p_i \ . \qquad \text{(Eq. 1.11)}$$

Figure 1.8a shows the pressure generated for $N = 3$ at the surface of a 10 µm photoabsorptive polymer film in water by a 1 µJ pulse with a beam diameter of 100 µm. It is suggested by Shan et al. that using a Dirac impulse function to approximate the temporal profile of the heat function is valid only if the duration of the laser pulse is much smaller than the propagation time of the acoustic wave across the absorption length (penetration depth) $1/\mu_a$. However, the derived expression for pressure can be considered the impulse response of the system, thus the temporal profile of the actual pulse can be convolved with Equation 1.10 to obtain the true result. In the case of a photoabsorptive polymer, $1/(\mu_a v_a)$ is typically less than 1 ns, therefore convolution is needed if using a laser emitting nanosecond pulsewidths. Figure 1.8b shows the convolution of Gaussian pulses of different pulsewidth with the pressure impulse response. It is clear that if the pulse-width is large enough, the secondary emission pairs will become completely integrated into the acoustic pulse. The acoustic bandwidth of the emission is then determined chiefly by the bandwidth of the optical pulse, which is inversely proportional to the pulsewidth. Figure 1.8c demonstrates the reduced bandwidth with increasing optical pulse width.

1.4 Statement of Objectives and Overview of this Thesis

The research reported in this dissertation focuses on the development, characterization, and application of two designs for a PI-etalon transducer. Chapter 2 presents the design and fabrication of the transducers as well as an evaluation of their optical and acoustic performance parameters. Chapter 3 explores the ability to perform high-resolution ultrasound imaging with synthetic 2-D arrays of PI-etalon transducers via beam scanning. To construct a device capable of minimally invasive imaging, a transition is then made towards achieving a fiber optic equivalent of the PI-etalon. In Chapter 4 we characterize a fiber optic receive-only etalon transducer in the context of photoacoustic imaging, and in Chapter 5 is presented work towards a fiber optic transmit/receive PI-etalon. Chapter 6 contains a synopsis of all results, presents methods for device and system improvement, and outlines future directions for the project.

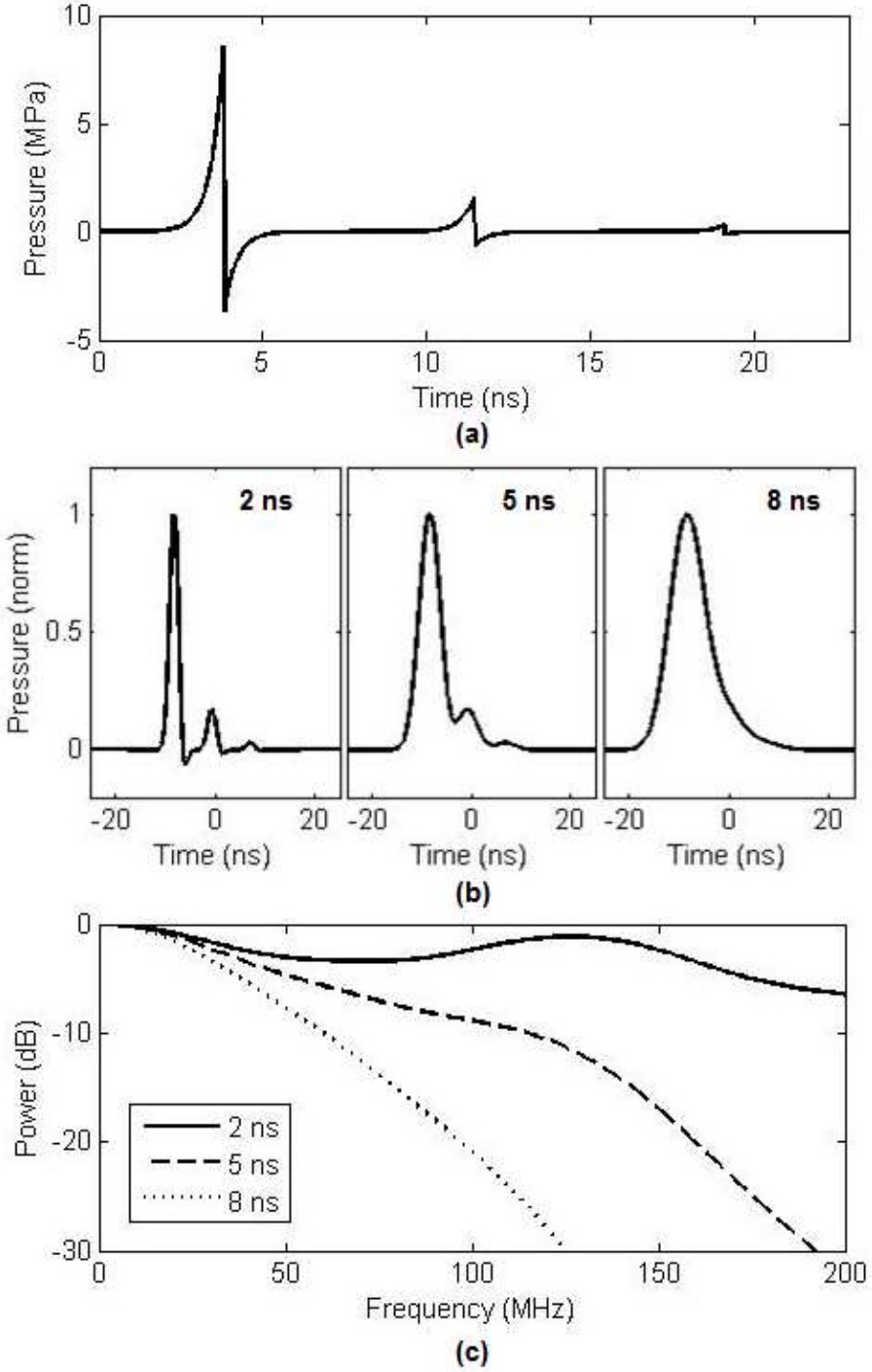
Pressure (MPa)
Time (ns)
(a)
2 ns
5 ns
8 ns
Pressure (norm)
Time (ns)
(b)
Power (dB)
2 ns
5 ns
8 ns
Frequency (MHz)
(c)

Chapter 2

Fabrication and Characterization of Wafer-based PI-etalons

2.1 Overview

Here we have characterized polyimide PI-2555/2525 as a thin film material for TUG and subsequently evaluated two designs for an all-optical transducer – both formed by integrating a PI film into an etalon receiver. Optical absorbance measurements of PI-2555/2525 indicate a penetration depth of 0.8 µm at the intended TUG wavelength (355 nm), yet acoustic output generated by a 8 ns, 25 mJ/cm^2 pulse with 43 µm spot size increased with film thickness up to 10 µm. The transducer design utilizing a larger amount of PI yielded a maximum pressure of 215 kPa. Including a dielectric mirror improved receive sensitivity, resulting in a noise-equivalent pressure of 3.3 kPa over a bandwidth of 47.5 MHz (0.48 Pa/Hz$^{1/2}$) when using a 35 µm NIR spot. Due to the added stiffness of the mirror, the transmit/receive center frequency increased from 37 to 49 MHz with a -6 dB bandwidth of 126 %. Finally, the 43 µm UV spot provided a -3 dB transmission angle of 30º and indicated a damage threshold of approximately 45 mJ/cm^2.

2.2 Introduction

All-optical transduction of ultrasound provides high frequency (> 20 MHz) operation in the absence of electrical noise and distortion that hinders small-scale piezoelectric probes. We have identified PI-2555/2525 polyimide precursor as a UV-absorbing film for TUG that is sufficiently transparent at wavelengths used for etalon operation. The first aim of this study is to quantitatively characterize the optical and acoustic properties of PI-2555/2525 for different film thicknesses in order to determine that which is optimal for acoustic transmission. Two different designs of the PI-etalon transducer model (Figure

1.7) are then evaluated, one of which allows for the integration of substantially more PI without drastically adding to the overall device thickness. This is facilitated by the inclusion of a dielectric mirror that reflects NIR and transmits UV, which also has the benefit of providing enhanced receive sensitivity via higher NIR reflectivity. We hypothesize that the added PI increases net UV absorption thereby providing higher pressure generation and preventing UV incidence onto the outer gold mirror, consequently raising the damage threshold.

2.3 Methods and Results

2.3.1 Characterization of PI-2555/2525

2.3.1.1 Optical absorbance and penetration depth

A 2.5 µm layer of PI was first created by spin coating PI-2555 onto a float glass substrate (thickness: 3mm; diameter: 1") and curing at 250°C in nitrogen. Absorbance of the layer was measured using a spectrophotometer (Beckman DU-640) and is shown in Figure 2.1a. The absorbance of the glass wafer was subtracted from the data prior to plotting. At 355 nm – the center wavelength of our excitation source for TUG – the measured absorbance indicates a transmittance of 4 %. Because reflection at the glass-polyimide interface is relatively small (less than 0.5% assuming that the refractive indices of glass and polyimide are 1.5 and 1.7, respectively), the majority of the 96 % not transmitted is likely absorbed. This ensures high conversion efficiency and minimal transfer of pulse energy to the etalon layers. The data also shows negligible absorbance in the NIR spectrum as demonstrated up to 2400 nm by French et al. [38]. Average transmittance of the film in the spectrum used for etalon operation (1510 – 1640 nm) was measured to be approximately 97 %.

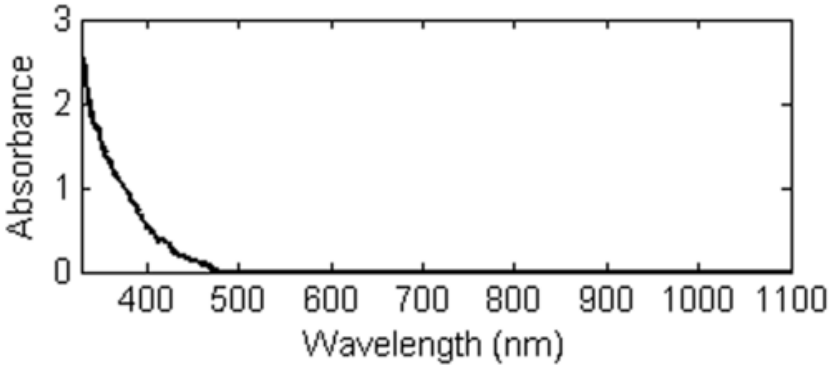

(a)

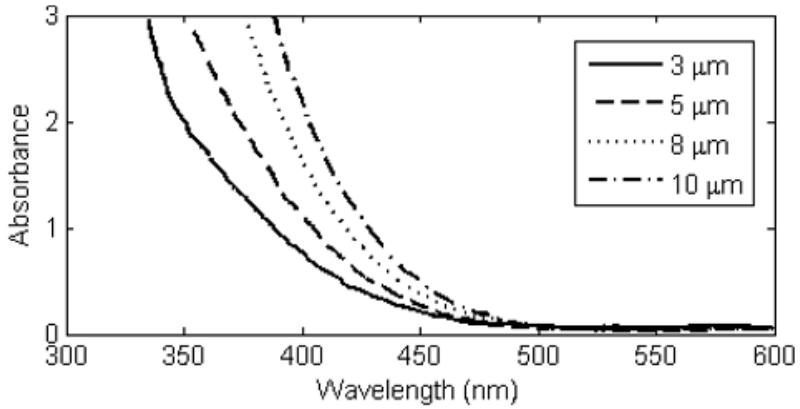

(b)

Absorbance curves for four polyimide layers of increasing thickness – [3, 5, 8, 10] µm – were also measured and are shown in Figure 2.1b where PI-2555 was used for the smallest thickness and PI-2525 for the remaining samples. It is clear that an absorbance value of 3 (T = 0.1%) at 355 nm is reached with a 5 µm layer of PI. Penetration depth at 355 nm is calculated by using the expression $l/\mathrm{A}\cdot\ln(10)$ where is the film thickness and is the absorbance. The absorbance and penetration depth for the 3 µm sample was 1.7 and 0.77 µm, respectively, and 2.7 and 0.80 µm for the 5 µm sample. Absorbance values at 355 nm for the thicker samples were outside the measurement range of the spectrophotometer.

2.3.1.2 TUG in Solitary PI Films

Despite obtaining greater than 99.9% absorption with a 5 μm sample, higher acoustic output was observed with films of greater thickness. Eight samples were prepared for acoustic measurements with layer thicknesses of [3, 5, 8, 10, 11, 13.1, 15.3, 16.2] μm. Larger thickness is not obtainable because of decreasing uniformity across the wafer (designed thickness range is 1.5-4 μm for PI-2555 and 5-13 μm for PI-2525). The first four samples were mounted adjacent to one another in a small plastic water tank such that they were approximately on the same UV focal plane (Figure 2.2a). The latter four were mounted adjacently in a second tank due to spatial constraints. Each tank was in turn mounted onto an x-y-z translation stage. Merely translating the tank to switch samples minimized differences in optical alignment which can confound the measurement. Adjustment of the tank in the depth dimension was made after translation to maintain the same time-of-arrival for the detected acoustic waveforms.

The combined 1064/532 nm output of a frequency-doubled Nd:YAG laser (LUCE, Bright Solutions) guided through a frequency-tripling crystal (LBO Type 1, Conex Systems Tech.) produced a 355 nm pulse (E = 0.4 μJ; width = 8 ns; PRF = 500 Hz) that was focused onto the samples. In Figure 2.2b can be see an image of the focused spot generated by a CCD camera with 20x objective (Sony XC-ST50). Because the illumination profile is non-Gaussian, determining the FWHM as a measure of spot size is not feasible. An alternative approach is to determine the effective spot size by integrating over the pixel values as described by Chalupský et al. [40]. We first consider the ideal circumstance in which the intensity is completely uniform:

$$I(x, y) = I_0 \ ,$$

where (x, y) are coordinates transverse to the beam propagation. In this case, the area of illumination is simply

$$A = \frac{E_{pulse}}{I_0} \ ,$$

where E_{pulse} is the energy of the pulse. For the case in which the intensity is not uniform, we can write

$$A_{eff} \equiv \frac{E_{pulse}}{I_{max}} \ ,$$

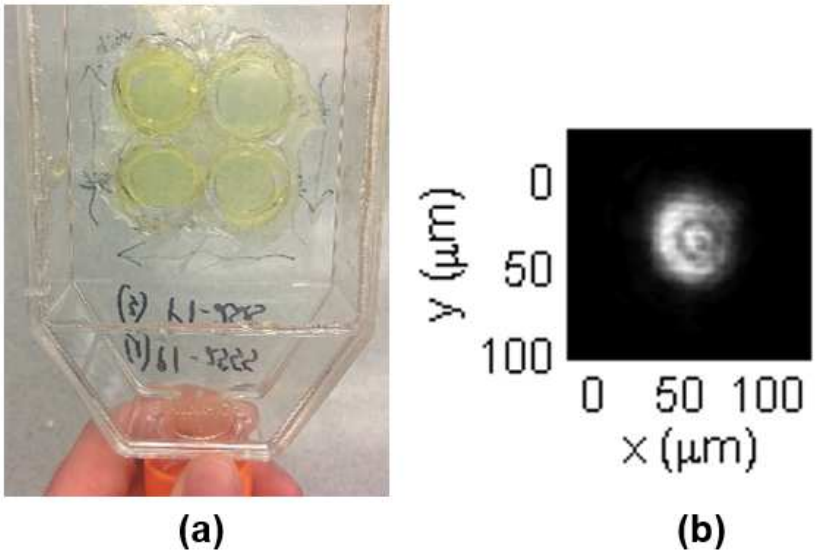

Figure 2.2. (a) Photograph of four PI samples of varying thickness mounted in a small water tank with **(b)** a CCD image of UV illumination, averaged 16 times [39] (© 2014 IEEE).

where is the maximum of . We can then expand this to

Therefore we can simply integrate over the intensity profile and normalize by the maximum to obtain the effective area of the spot. This can be easily validated by again assuming a uniform profile, in which case resulting in . The effective diameter of the spot is then . In the case of the data provided by a CCD image:

where is a value proportional to intensity that is generated by a pixel with position indices . The conversion factor from pixels to meters depends on the objective used with the camera. Using this method, the effective diameter of the UV spot in Figure 2.2b after nulling pixels under a $1/e^2$ threshold was 43 µm, which yields a UV intensity of 25 mJ/cm^2.

The acoustic waveform generated by the UV pulse was detected using a calibrated 40 MHz hydrophone with 20 dB preamplifier (aperture: 85 µm, HGL-0085/AH-2010, Onda

Corp.) positioned 1 mm from the film. Its output was sampled with an 8-bit digitizer at 250 MHz (PXI-5114, National Instruments Corp.) triggered by the output of a 1 ns PD (DET10A, Thorlabs Inc.) picking up ambient laser light. After 1024 averages, the amplitude of the waveform was recorded at four randomly-selected locations by translating the samples. In order to reduce the influence of any fluctuations in UV energy, this was performed three more times to provide a total of 16 measurements per sample. The average pressure produced by each PI film is shown in Figure 2.3. A change in orientation of the film plane with respect to the focal plane occurred when replacing the first tank with the second, therefore a discontinuity exists between data corresponding to the two sets. The result demonstrates over a 30 % increase in output pressure when the film thickness is raised from 3 μm to 10 μm followed by a plateau at higher thicknesses. It is presently unknown why pressure output continues to increase far past the 0.8 μm penetration depth. Thermal properties such as the thermal expansion coefficient for PI-2555 and PI-2525 are equal (40 ppm), so greater pressures caused by a difference in material properties is unlikely.

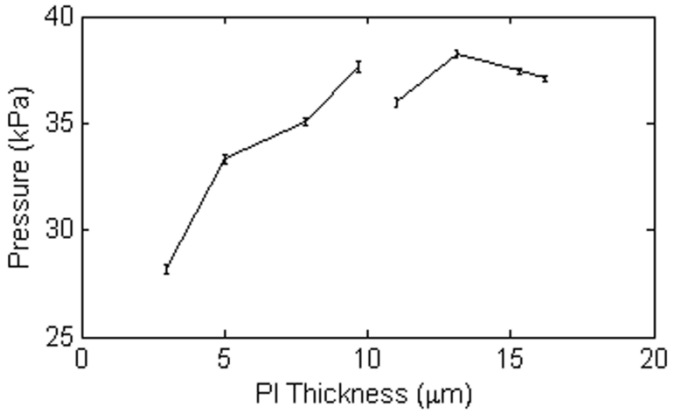

2.3.2 Transducer Fabrication

There are two designs implemented in this work as shown in Figure 2.4a and 2.4b, which will henceforth be referred to as the Au/Au and Die/Au designs, respectively. The Au/Au design allows for simple fabrication, small device thickness, and an etalon polymer of high compressibility (inversely proportional to modulus). The Die/Au design provides higher mirror reflectivity in the NIR range and transmission of UV. The latter feature accommodates the choice of PI for the etalon polymer. Any UV energy passing through the initial PI layer may then be absorbed by the etalon polymer. Given the aforementioned study on acoustic output versus PI thickness, we hypothesize that this will provide higher acoustic output and the prevention of UV incidence onto the second mirror – a layer susceptible to damage given that gold is not transparent in the UV range. Because the dielectric mirror is of much higher thickness than gold, it was not chosen to serve as the second mirror as well. This would make the device substantially thicker and increase the mismatch in acoustic impedance between the device and coupling medium.

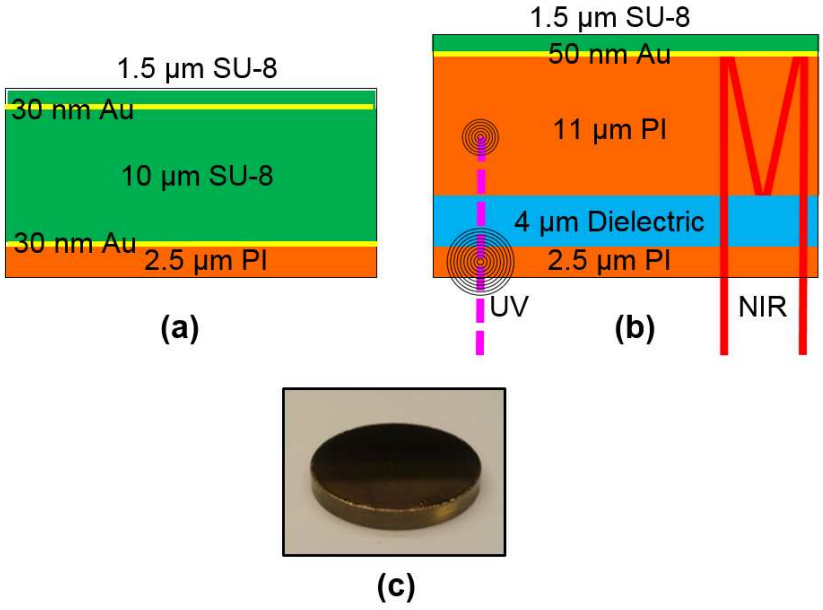

For both designs, polyimide adhesion promoter VM-651 (HD Microsystems) was spin-coated onto float glass optical windows having a diameter of 25 mm and a thickness of 3 mm. A 2.5 µm layer of PI-2555 was then spin-coated and cured in nitrogen. For design Au/Au, both etalon mirrors consisted of a titanium-gold-titanium tri-layer with thicknesses of 3 nm, 30 nm, and 3 nm, respectively, and were deposited using electron beam evaporation. Gold was chosen for its high reflectively in the NIR range and titanium was chosen to facilitate adhesion. For the resonator cavity, a 10 µm layer of SU-8 2010 photoresist (Microchem Corp.) was spin-coated in between deposition of the two mirrors and was cured and exposed to UV light for cross linkage. Finally, a 1.5 µm layer of SU-8 2002 photoresist was spin-coated on top of the second mirror to add a layer of protection to the device. Because air bubbles arose from the underlying PI film when curing the SU-8 layers on a hot plate, SU-8 films were cured in an oven. A photograph of an Au/Au sample is shown in Figure 2.4c.

For design Die/Au, a 4 µm dielectric stack designed to have high UV transmittance and high NIR reflectance was deposited on top of the 2.5 PI layer. The mirror was designed and fabricated by Evaporated Coatings, Inc., therefore the dielectric materials comprising the mirror remain proprietary. The transmittance of the film at 355 and 1550 nm – the operating wavelengths of the transducer – is 93 and 1.3 %, respectively, as seen in Figure 2.5. Data was provided by Evaporated Coatings, Inc. For the etalon medium, 11 µm of PI-2525 was spin-coated followed by electron-beam evaporation of a 50 nm gold mirror. Again, 1.5 µm of SU-8 photoresist was spin-coated to add a layer of protection. Given the high UV transmittance of the dielectric mirror, we initially excluded the 2.5 µm layer of PI. However, device breakdown without this layer was found to be initiated by damage to the mirror. We conclude that the non-negligible UV absorption by the dielectric mirror requires an initial layer of PI to absorb a large fraction of the energy. Finally, both the Au/Au and Die/Au designs were mounted on the same focal plane for proper comparison of the performance parameters

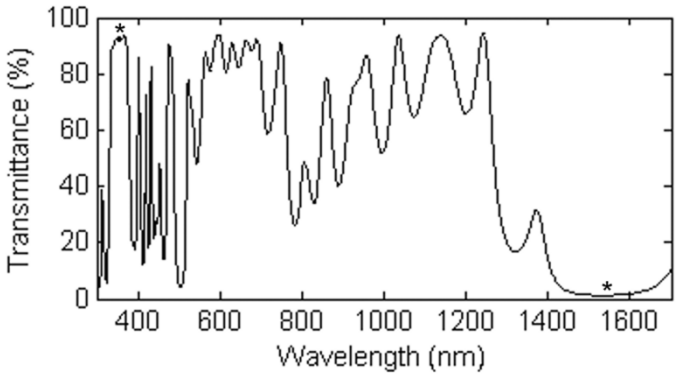

2.3.3 Transducer Characterization

2.3.3.1 Optical Resonance

To evaluate optical resonance, a continuous-wave (CW) NIR laser (output power: 5 mW, HP 8168F, Agilent Technologies) was fiber-coupled to a free-space circulator via a fiber collimator (F280FC-1550, Thorlabs, Inc.) and focused onto the etalon with a spot size of 35 µm in diameter using a lens of 60 mm focal length. The optical and DAQ system for the measurement is illustrated in Figure 2.6. The circulator is composed of a polarizing beam splitter (PBS) and quarter-wave plate. The PBS linearizes the NIR input polarization, and the wave plate then changes the polarization to circular. Upon reflection at the etalon, the circular direction/handed-ness of the polarization is reversed. Conversion back to linear polarization then occurs by passing again through the wave plate. Because this polarization is orthogonal to the incoming polarization, the PBS directs the reflected beam in a direction orthogonal to the incoming beam thereby allowing it to be monitored independently. Both the PBS and focusing lens are coated with NIR anti-reflective coatings to maintain power.

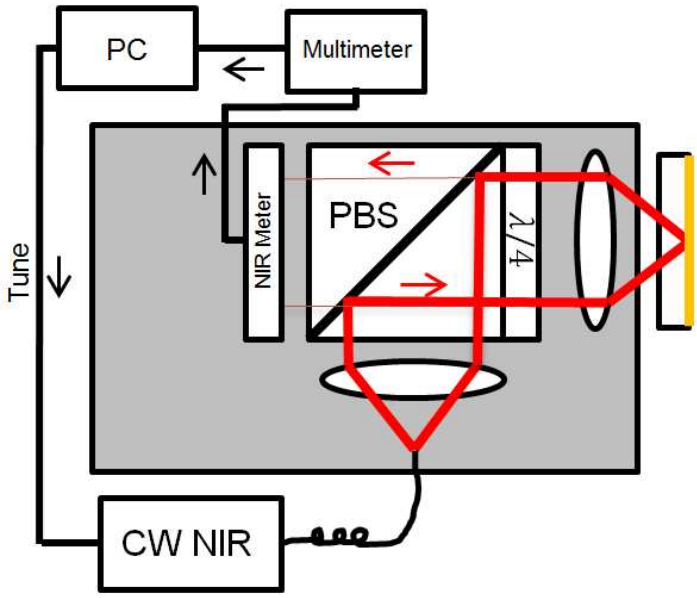

The DC value of the reflected NIR power was recorded (S122B power meter, Thorlabs Inc.) for both samples while scanning the NIR wavelength with 0.1 nm resolution. This was conducted at four randomly-selected locations per device. An example of a resonance profile for each device is plotted in Figure 2.7. Notice a sharper resonance and higher baseline power for Die/Au. At each location, the optical finesse – a key determinant of receive sensitivity – was calculated by dividing the free spectral range (FSR) by the average FWHM of the two resonances captured. The average finesse across locations was 25±2 for the Au/Au device and 67±6 for the Die/Au device.

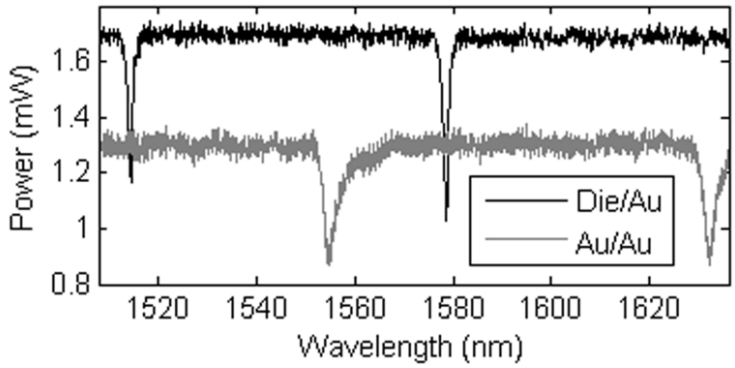

2.3.3.2 Acoustic Performance

2.3.3.2a Receive Sensitivity and Bandwidth

A determinant of acoustic sensitivity is the noise-equivalent pressure (NEP) – the lowest pressure a transducer can detect, defined as the pressure amplitude that provides an SNR of 1. It is ascertained by detecting a waveform originating from an acoustic source whose maximum pressure amplitude is known. By associating this with the maximum voltage recorded by the etalon system, a voltage-to-pressure conversion factor is obtained. The NEP is then determined by converting the root-mean-squared value of the noise in the etalon waveform at a time point that precedes the pulse. This is more accurate than using the post-pulse period wherein acoustic transients are still present.

To perform the measurement of NEP, the devices were mounted side-by-side in a small plastic water tank using epoxy. The substrates of the etalons were integrated into the tank wall such that they were directly accessible with the system optics, and the device layers are in direct contact with water. The known acoustic source used to measure NEP was a 25 MHz ultrasound probe (active area: 12.5 mm; focal length: 25.4 mm, V324 Olympus NDT Inc.) driven by a pulser/receiver (bandwidth: 50 MHz, DPR300, JSR Ultrasonics). Prior to the experiment, the maximum amplitude of the transmitted pressure wave was measured using the calibrated 40 MHz hydrophone with 20 dB preamplifier, and it was found to be 1.13 MPa. The probe was mounted on its own

translation stage to align its acoustic focal point with the focal point of the NIR beam. Its pulse as detected by the pulser/receiver unit after being reflected off of the etalon (pulse-echo) is shown in Figure 2.8a.

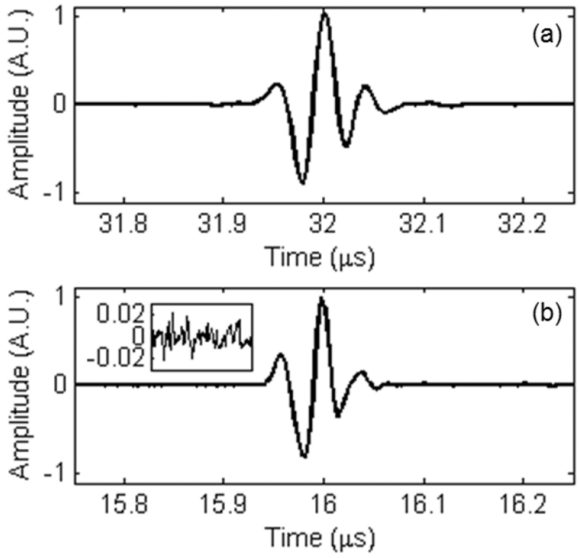

Etalon sensitivity was optimized by tuning the NIR wavelength onto the region of highest slope in the resonance profile followed by insertion of a 1.5 GHz amplified PD (818-BB-30A, Newport Corp.) to detect oscillations in the reflected power induced by HFUS (see Figure 2.9 for setup). Input power was fixed at 2 mW for both devices to ensure a proper comparison. The waveform detected by the etalon was then band pass filtered from 2.5-50 MHz and amplified by 30 dB using the receive amplifier of the DPR300, followed by 8-bit digitizing at a sample rate of 250 MHz. A waveform detected by design Au/Au is shown in Figure 2.8b and is well correlated with the shape of the pulse-echo. Based on the maximum amplitude of the unaveraged etalon waveform and the RMS value of the noise prior to the pulse, the NEP was calculated at four locations and averaged for both devices. The NEP was 3.3±0.3 kPa (0.48±0.05 $Pa/Hz^{1/2}$) for Die/Au and 6.0±0.5 kPa (0.87±0.07 $Pa/Hz^{1/2}$) for Au/Au. The increased reflectivity accompanying the use of a dielectric mirror has therefore improved the sensitivity by a factor of two.

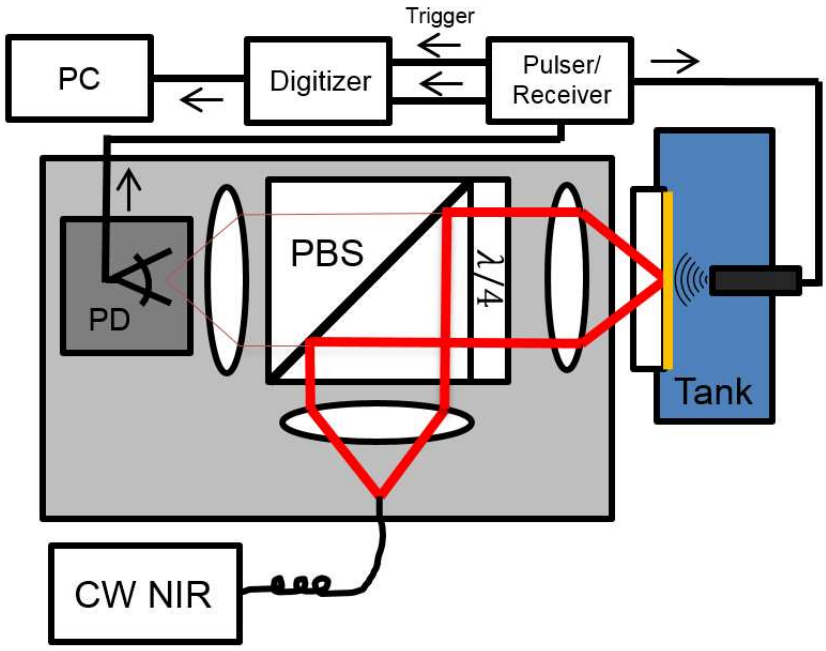

Receive bandwidth was not determined at this time due to the lack of a broad band acoustic source. Experimentally-determined receive bandwidth for etalons of varying thickness can be found in [18]. An Au/SU8/Au etalon with 10 µm thickness was reported to have a central frequency of approximately 40 MHz with a -6 dB bandwidth of 30 MHz, or 75%. Because the Au/Au and Die/Au designs are of slightly larger thickness, their central receive frequency is most likely lower and in the range of 30-40 MHz. Using Equation 1.6, the theoretical estimation for the central frequency of a 12 µm SU-8 etalon is 26 MHz. This differs from the experimental values mostly likely because the modulus increases with frequency. Modulus values measured in the MHz range were unable to be identified.

2.3.3.2b TUG Amplitude and Spectrum

High frequency ultrasound was again generated with a 355 nm optical pulse to evaluate and compare the transmit/receive center frequency and bandwidth between the Au/Au and Die/Au devices. Any increase in maximum pressure when using the Die/Au device could be attributed to (1) a higher damage threshold and hence utilization of higher UV energies and (2) an increase in total PI thickness for greater absorption. The second has already been demonstrated with bare PI films. To assess any increase associated with the inclusion of more PI in the Die/Au design relative to Au/Au, the maximum pressure for both devices was measured at a constant UV intensity – 25 mJ/cm^2 – with the hydrophone placed at 1 mm depth. As illustrated in Figure 2.10, the UV pulse was focused using the same lens that focuses the NIR beam. This is accomplished by directing the UV pulse to a laserline mirror (R355-T532/1064-B, Lattice Electro Optics) inserted between the lens and optical circulator. This mirror reflects UV and transmits NIR. Measurements were again taken at four locations on each sample with the time-of-arrival held constant. The maximum pressure was 39±0.5 kPa for Die/Au and 33±1 kPa for Au/Au. An increase is clear, but its extent is less than that observed with bare PI films. This may be due to mechanical damping imposed by the 4 μm dielectric layer.

In an experiment held at a different time than the previous, the representative waveforms generated by both designs were recorded with the hydrophone to determine any differences in emission bandwidth (measurement distance: 0.5 mm). Their power spectrums were then calculated using:

$$nfft = 2\text{^}(nextpower(size(v)),$$

$$f = f_s * (0:(nfft/2))/nfft \ ,$$

$$Y = fft(v, nfft) \ ,$$

$$Pyy = Y \cdot Y^*/nfft \ ,$$

$$P = 10\log\left(Pyy/\max\left(Pyy\right)\right) \ .$$

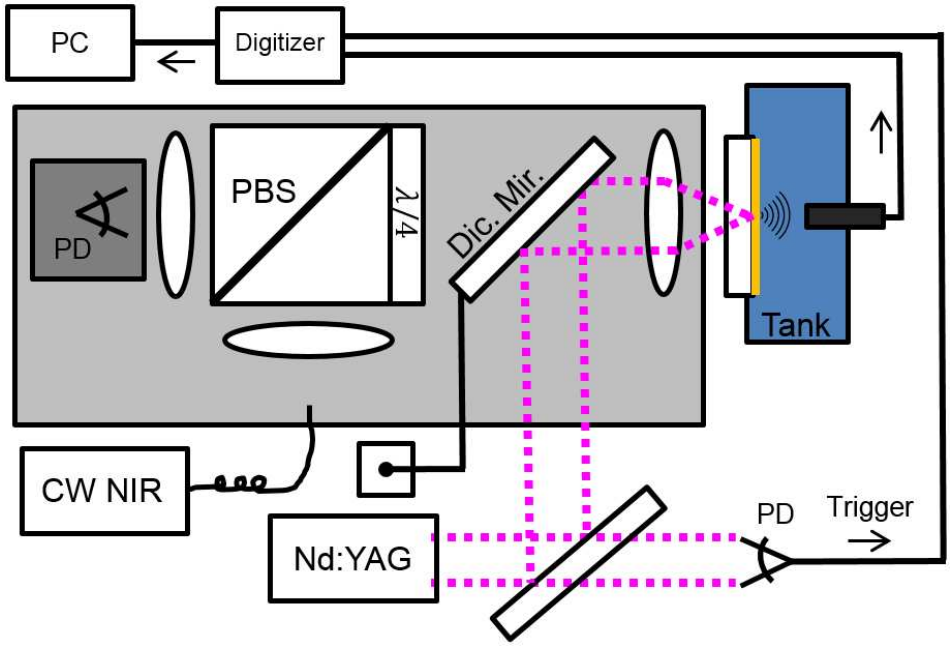

where is the voltage waveform, is the sampling frequency, and corresponds to the complex conjugate of . *Nextpower.m* finds the largest power of 2 by which its argument is divisible and adds one. The waveforms and their respective power spectrums are shown in Figure 2.11. Alignment was not optimized and UV energy was decreased, so the pressure amplitudes are lower than those previously measured. However, a larger amplitude observed with the Die/Au design relative to Au/Au is confirmed. Because of its cutoff frequency at 40 MHz, the power spectrums are dominated by the hydrophone's response. Despite the suppression of the emissions' bandwidth, the Die/Au spectrum appears to exhibit higher power than Au/Au at frequencies greater than 50 MHz.

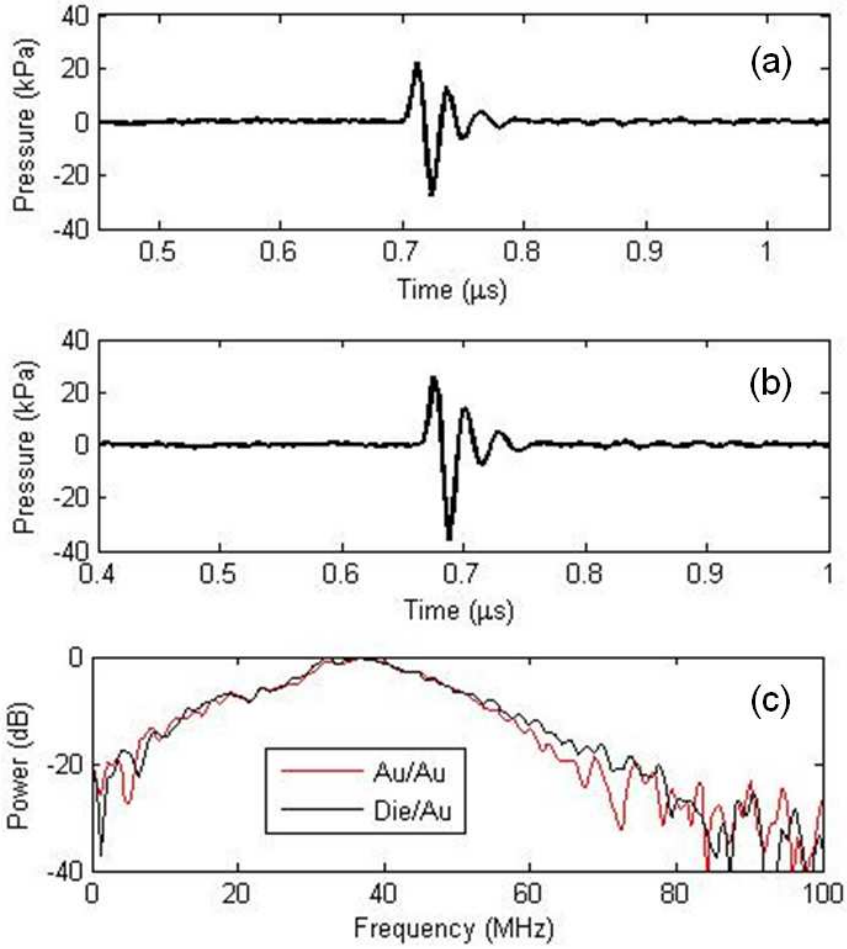

2.3.3.2c Directivity

Transmit directivity of both devices was measured by rotating the hydrophone about the UV spot with a rotational stage. A photograph of the setup is shown in Figure 2.12. The device with small tank was oriented perpendicular to the table in a larger water tank that allows angular translation of the hydrophone about the UV spot. The focusing lens used in the previous measurements was also used in this experiment to maintain the same spot size. The amplitude of the waveform was recorded throughout a range of -50º to 50º relative to normal with a step size of 1º. 2048 averages were completed at each

angle using a 1 kHz pulse repetition frequency (PRF). The directivity curves for the two devices are shown in Figure 2.13. Both exhibit a -3 dB transmission angle of approximately 30º, though sidelobes are more pronounced in the Die/Au. Asymmetry in the curves is caused by imperfect rotational alignment.

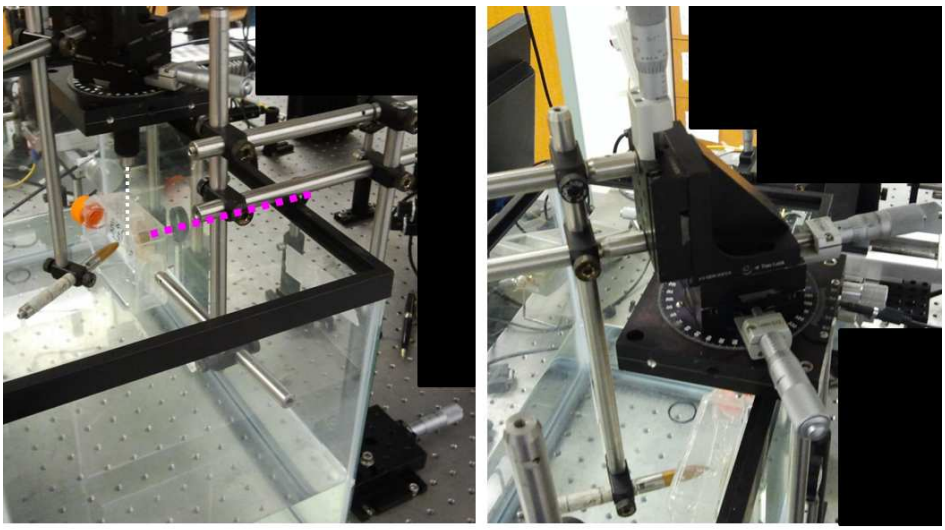

(a) (b)

The directivity function of an ideal circular transducer is:

_____

where is the wave number, is the radius of the element, and is a Bessel function of the first kind. Assuming that the UV spot size did not change when transitioning from the Au/Au to Die/Au, a change in emission bandwidth is likely responsible for any change in directivity shape. According to the model, the mainlobe width is reduced and the sidelobes are enhanced with increasing frequency. The latter is confirmed but the former is not in the experimental result. This may be due to spectrums that do not contain a single central frequency. The Fraunhoffer zone – the axial distance at which Equation 2.3 is accurate – begins at a depth of . This value is approximately 10 µm in our case, which is significantly smaller than the hydrophone measuring depth.

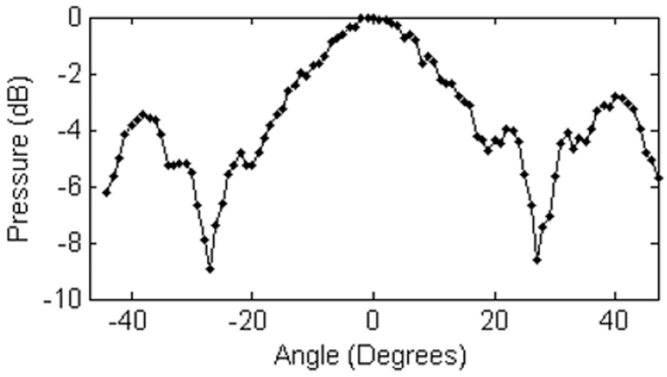

(a)

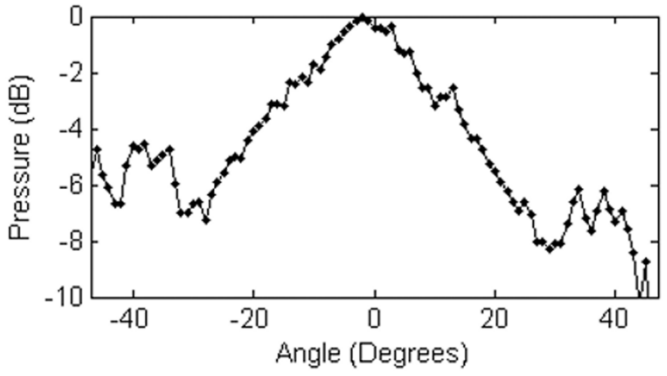

(b)

Receive directivity was not completed at this time due to lack of a rotatable, high frequency source. A directivity study by Cox and Beard showed that the effective diameter of an etalon receiver is not always equal to the diameter of NIR illumination, particularly when the spot radius is less than twice the etalon thickness [41]. In our case, this ratio is approximately . Also in [41] is a graphical means of estimating the effective spot diameter as shown in Figure 2.14a. The central receive frequency was estimated at 30-40 MHz, therefore the *ka* value is approximately 2-3 (*a* being the radius of illumination). Estimating the effective radius from this chart requires a curve corresponding to *a=d/1.6*. The region where is likely to fall is indicated by the red box. The average value on the vertical axis in this region is approximately , therefore the effective spot diameter is μm for Au/Au and Die/Au. It is possible that the 43 μm UV spot also does not accurately represent the effective transmit diameter. A more thorough directivity analysis than that presented here (as in [41]) is required to make this determination.

As an estimate for receive directivity, Equation 2.3 is plotted in Fig. 2.14b given the estimated effective receive diameter and a central frequency of 35 MHz. The -3 dB transmission angle is approximately 80°. Because th e transmit directivity appears to be more restricted than the estimated receive directivity, its mainlobe and sidelobes likely dominate the full transmit/receive directivity profile. An estimate for the complete transmit/receive response was determined by combining the data in Figure 2.13a and Figure 2.14b. This curve (Figure. 2.14c) exhibits a -6 dB angle of 45°.

2.3.3.2d Pulse-echo

In order to measure the combined transmit/receive waveform and spectrum, the NIR and UV beams were enabled simultaneously and then co-aligned in order to transmit and receive in the same location (Figure 2.15). Alignment is performed using both a course and fine stage. The former is done using the high-gain 25 MHz probe, and the latter makes use of the etalon signal generated when the UV pulse heats the etalon layers. These stages are as follows:

Course:

1. Set up etalon detection with transmitting 25 MHz probe as in Figure 2.9.
2. Change pulser/receiver to receive-only mode without changing probe position.
3. Switch DAQ trigger source from pulser/receiver to UV PD as in Figure 2.10.
4. Steer UV beam using linear actuators connected to mirror mount (Figure 2.15) until TUG signal detected by 25 MHz probe is maximized.

Fine:

1. Observe etalon detection of thermoelastic signal generated by UV pulse using no high-pass filtering.
2. Further steer UV beam until low-frequency thermoelastic signal is maximized.
3. Remove 25 MHz probe, and insert reflective target.
4. Directly connect PD output with digitizer (remove amplifier).
5. Increase averaging until SNR is sufficient.
6. Store for post-processing.

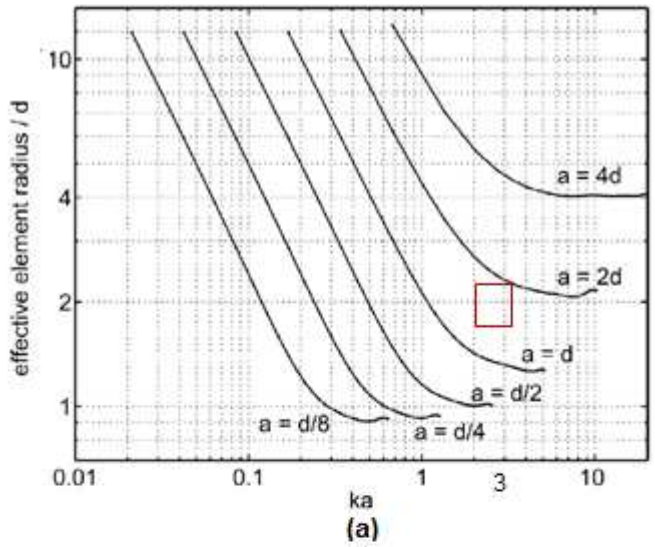
effective element radius / d
10
4
2
1
a = 4d
a = 2d
a = d
a = d/2
a = d/4
a = d/8
0.01
0.1
1
3
10
ka

(a)

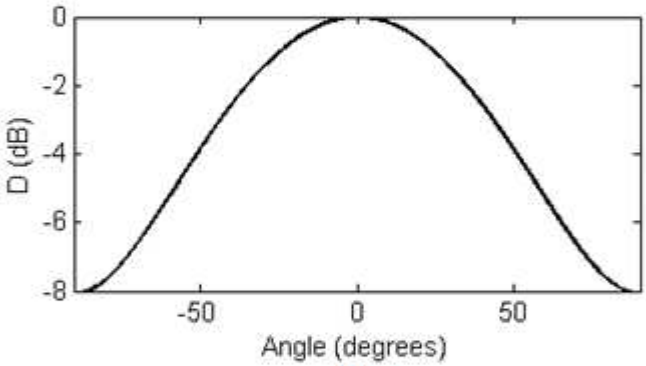
D (dB)
0
-2
-4
-6
-8
-50
0
50
Angle (degrees)

(b)

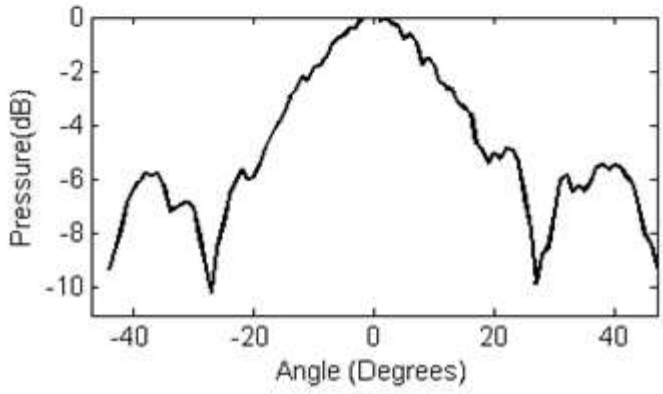
Pressure(dB)
0
-2
-4
-6
-8
-10
-40
-20
0
20
40
Angle (Degrees)

(c)

Regarding step 1 of the fine adjustment stage, the thermoelastic signal refers to a waveform exemplified by that shown in Figure 2.16. The relatively low-frequency, decaying signal (< 5 MHz) arises from the heating of the etalon by the UV pulse that creates thermal expansion of the resonator cavity. Because its time course is on the order of 100 µs, it is easily separable from the signals of interest by use of filtering. However, it is useful for the alignment stage because it is of high amplitude and thus easily observable. Concerning step 4 of the fine adjustment stage, no amplification is performed between the PD and the digitizer in order to remove the influence of the amplifier on the PI-etalon's waveform shape and frequency content. Finally, it is worth noting that the reason for using motorized actuators to steer the UV beam is that both large and very small stepping distances are required, which can be difficult to reproduce using manual micrometers. They are also essential for imaging experiments because their adjustment can be automated.

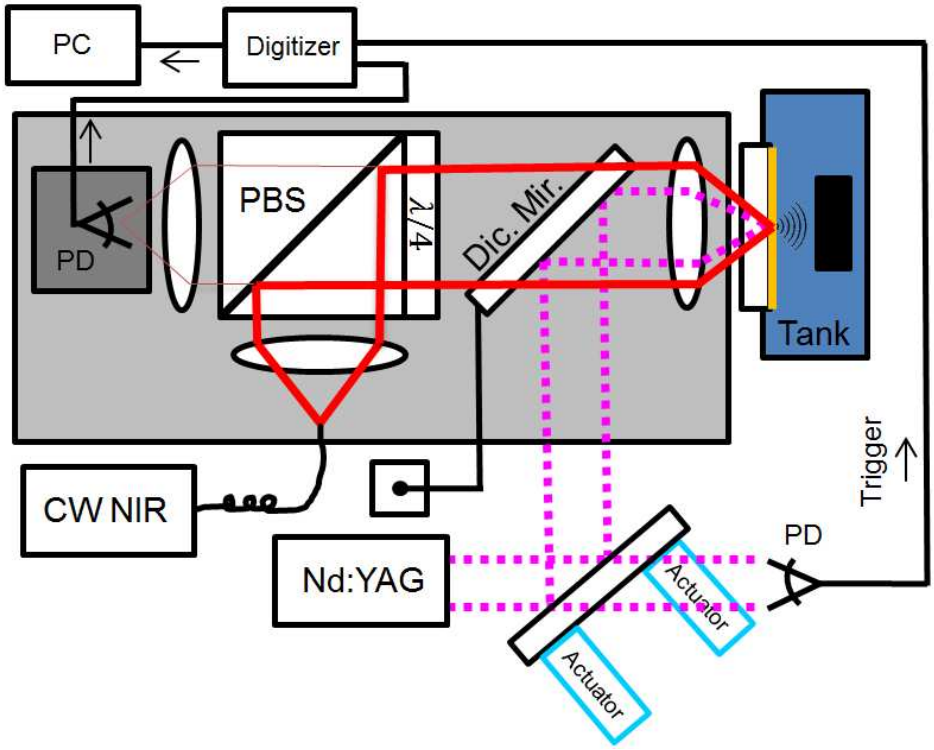

A solid metal plate placed at a depth of 1.3 mm served as a reflecting target. The pulse-echo waveform was recorded with no amplification after 1024 averages, the speed of which was dictated by the PRF of the Nd:YAG laser (500 Hz). A finite impulse response (FIR) high pass filter with a cutoff frequency of 2 MHz was then applied to exclude the thermoelastic response of the etalon. Waveforms were acquired at four randomly-selected locations on both Au/Au and Die/Au devices and then averaged. Examples are shown in Figure 2.17a and 2.17b, respectively, with their power spectrums overlaid in Figure 2.17c. The average center frequency of the Die/Au device was 49±0.6 MHz with a -6 dB bandwidth of 126±6 %. The center frequency of the Au/Au device was 37±0.8 MHz with a bandwidth of 92±3 %. Added frequency content past 50 MHz with a secondary peak occurs in the spectrum for Die/Au, which was marginally indicated in the transmission spectrums in Figure 2.11c. This could signify the presence of two mechanical resonances associated with the two polymer layers, induced by the high stiffness of the dielectric mirror.

2.3.3.2e Damage Threshold and Maximum Pressure

The damage threshold of both devices was next determined, and the maximum pressure generated at breakdown was recorded. Device breakdown was considered to have occurred after a decrease in the thermoelastic signal of the etalon (Figure 2.16) in response to increasing UV energy. Following this observation, the UV energy was measured with a high-sensitivity pyroelectric sensor (J3-09, Molectron), and the maximum pressure was measured by the hydrophone at a depth of 0.3 mm. Both of

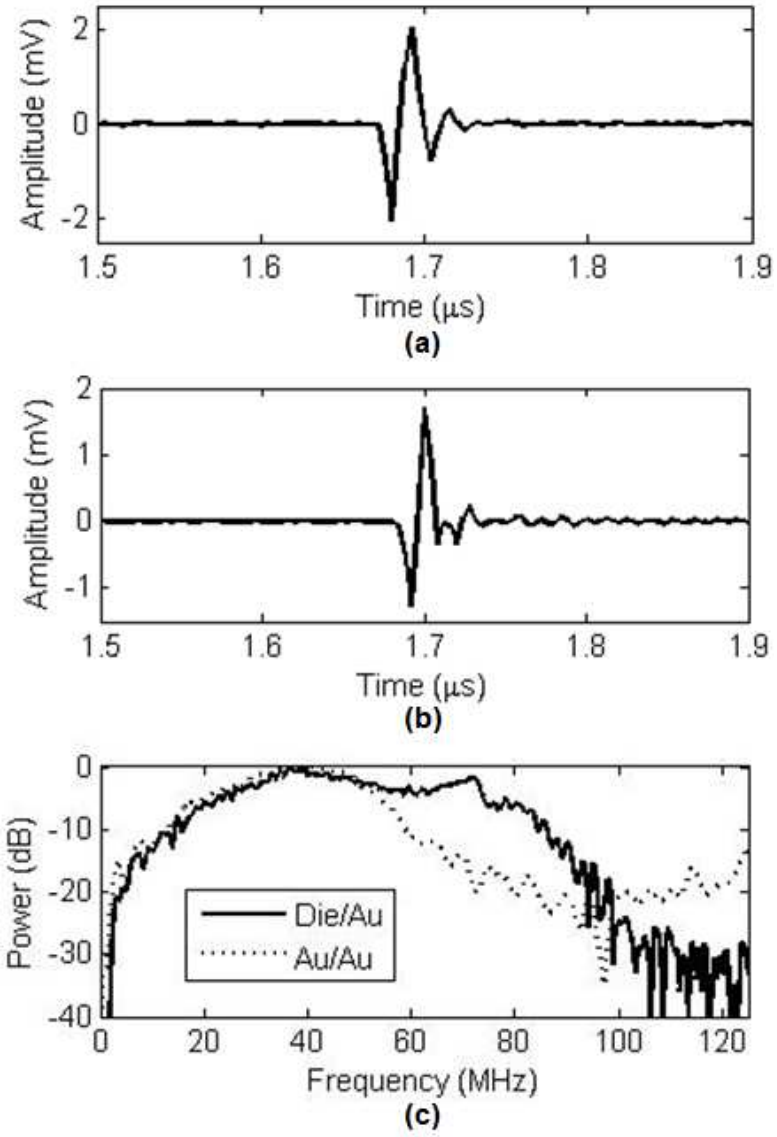

these measurements were found to vary significantly which prompted the collection of an additional block of data for both devices, i.e. from a total of eight locations. Assuming a 43 μm UV spot, the average damage threshold for Die/Au was 45±3 mJ/cm^2 and the maximum pressure was 213±52 kPa. The damage threshold for Au/Au was 46±8 mJ/cm^2 with a maximum pressure of 233±43 kPa. Judging from the standard deviations of these parameters, the comparison between devices is inconclusive. The lack of precision can be attributed to a non-uniform UV spot, i.e. an illumination profile with

localized areas of high intensity (Figure 2.2b). When the NIR and UV beams are co-aligned, these areas may or may not be perfectly coaxial with the NIR spot. If they are not, breakdown is perceived to have occurred at higher UV energies. If there is in fact a gain in damage threshold with the Die/Au device, the standard deviations indicate that it is limited to 12 mJ/cm^2.

2.4 Discussion

We have demonstrated here the fabrication and functionality of all-optical HFUS transducers consisting of a PI thin film deposited underneath an etalon receiver. TUG was elicited using an 8 ns UV pulse while the etalon operates in the NIR spectrum. The high absorption at 355 nm and high transmittance at 1550 nm of PI-2555/2525 allows stable and efficient dual-mode operation. Two designs for the etalon structure were presented – one with layers Au/SU-8/Au and another with a Dielectric/PI/Au stack. A dielectric film was chosen to serve as the bottom etalon mirror for its increased NIR reflectivity and transparency to UV light. This permits the inclusion of a thicker PI layer without substantially increasing overall device thickness – a choice informed by an observed 30 % increase in pressure produced by a 10-15 μm film. As summarized in Table 2.1, the Die/Au design exhibited in an increase in sensitivity (decreased NEP), frequency content, and output pressure. Improvements in damage threshold and maximum pressure generated are likely but unconfirmed due to measurement difficulties.

Improvements in performance notwithstanding, greater steps need to be taken to establish all-optical transducers as a viable alternative to other ultrasound technologies. For a comparison in performance, Table 2.1 includes parameters for a collapse-mode CMUT – another technology suitable for high frequency 2-D arrays due to their ease of fabrication relative to piezoelectrics [42]. Achievable center frequency and bandwidth is greater in the optical devices presented and have a similar output pressure. The NEP of the CMUT was not provided, however CMUTs generally have slightly lower sensitivity than piezoelectric transducers [43]. The receive characteristics of the Onda hydrophone (piezoelectric membrane) used in this study are also included in Table 2.1. The NEP of the hydrophone was estimated (using RMS of noise and V/Pa conversion factor) to be

	Element Diameter (μm)	Optical Finesse	NEP $Pa/\sqrt{Hz}$	T/R f_c (MHz)	T/R -6 dB Bandwidth (%)	Pressure at $E = E_0$ z = 1 mm (kPa)	Max Pressure @ z(mm) (kPa)	Damage Threshold (mJ/cm^2)
Au/Au	43	25±2	0.87±0.07	37±0.8	92±3	33±1	233±43 @ 0.3	46±8
Die/Au	43	67±6	0.48±0.05	49±0.6	126±6	39±0.5	213±52 @ 0.3	45±3
CMUT	230*	-	-	28	90	-	295 @ 0†	-
Onda	85	-	1.2	23 (R)	200 (-3dB)	-	-	-

Table 2.1 Comparison of performance parameters between Die/Au and Au/Au PI-etalons. Data represent the average across four locations on the wafer and standard deviation with the exception of Max Pressure and Damage Threshold where eight locations were used. Also shown are parameters for alternative devices with comparable active area and frequency response – a CMUT [42] and the Onda HGL-0085 hydrophone (**T/R**: Transmit/Receive; $\mathbf{E_0}$: 25 mJ/cm2; **R**: receive-only; **z**: measurement depth; *Effective diameter calculated from rectangular dimensions; †Half of peak-to-peak measured at device surface) [39] (© 2014 IEEE).

1.2 $Pa/Hz^{1/2}$ - slightly higher than that for the PI-etalon. The performance of the PI-etalon is therefore similar to other high frequency technologies with small active area, however SNR needs more improvement in order to motivate a shift towards laser-based systems. Many averages are required at present, which is not a practical option for real-time imaging.

An increase in maximum output pressure could be accomplished by increasing four parameters associated with the UV beam: spot size, illumination uniformity, wavelength, and pulse-duration. At the expense of directivity, a larger UV spot in the range of 100-200 μm will facilitate greater net absorption by lowering intensity. By eliminating localized areas of high intensity in the beam profile, a uniform illumination will increase thermoelastic conversion efficiency [44]. Increasing the wavelength and pulse duration would likely increase the damage threshold, though the latter would reduce transmit bandwidth. The choice of wavelength is limited by the absorption spectrum of PI-2525/2555. Using absorbance measurements for the first group of bare PI films, an absorbance of 1.4 (the value reported for the 2.5 μm PI layer in [37]) was observed for the 10 μm PI layer at 415 nm – a potential upper limit on useable wavelengths. Regarding pulse duration, Piglmayer et al. demonstrated that the ablation threshold for a PI film at 302 nm is nearly constant for pulse widths below 200 ns [45], but this

relationship remains to be seen for higher wavelengths. Yung et al. reported an ablation threshold of 100 mJ/cm^2 for a PI film at 355 nm using 21 ns pulses [46]. Assuming that PI dictates the limit on damage threshold for the overall device, an increase in pulse width appears justified given our estimate of 45 mJ/cm^2 using an 8 ns pulse. However, damage threshold may be dependent on the particular compound of polyimide used.

Gains in sensitivity will also lend towards a more tenable SNR. Simple alterations that can decrease the NEP include selecting a PD with lower noise-equivalent power and an NIR laser with higher output power. Other methods entail further modifying the thin film structure with alternative fabrication procedures. Relatively simple adjustments for an improved Q-factor include increasing the etalon thickness and replacing the second mirror with another dielectric mirror, although disadvantages accompany these adjustments. Increasing the etalon thickness would decrease bandwidth, and using an outer dielectric mirror similar in thickness to the first would increase reflections at the device-medium interface. More drastic changes that could improve sensitivity involve patterning the films along the lateral dimension. Zhang and Beard showed that the Q-factor of a fiber optic etalon was considerably increased by creating a convex outer mirror, producing an NEP of 85 Pa over a bandwidth of 20 MHz (20 mP/Hz$^{1/2}$) [47]. Tadayon et al. have created a waveguide structure in a polymer etalon that achieved an NEP of 178 Pa over a bandwidth of 28 MHz (30 mPa/Hz$^{1/2}$) [48]. These techniques will be discussed in more detail in Chapter 6.

Chapter 3

Imaging with Wafer-based PI-etalons

3.1 Overview

For the first time we demonstrate the viability of an all-optical ultrasound transducer with supporting optics to form an imaging system yielding the dynamic range required for tissue imaging. We present the mechanisms, merits, and results of two synthetic-array configurations created by scanning the receive (NIR) and transmit (UV) beams across the PI-etalon surface. The first is a fixed-transmitter/scanning-receiver technique wherein the NIR etalon beam with 35 µm spot is scanned across a 2 x 2 mm aperture upon which a stationary 2.8 mm UV spot transmits ultrasound in a plane-wave like mode. The imaging of wire targets placed at a depth of 1.8 mm and 5.2 mm yielded an estimate of 71/145 µm for the lateral resolution and 35/38 µm for the axial resolution in offline reconstruction. The second system consists of a fixed-receiver/scanning-transmitter configuration which translates a 43 µm UV spot across of a 2 x 2 mm aperture for each of four receive locations. Reconstruction of wire targets indicates a lateral resolution of 70/114 µm at depths of 2.4 and 5.8 mm, respectively, with an average axial resolution of 35 µm. Finally, we explore the challenges of imaging in the latter configuration, which provides the best opportunity for real-time performance pending further development.

3.2 Introduction

We have previously demonstrated the performance of an integrated all-optical transmitter/receiver consisting of a UV-absorbing PI thin film that is also transparent in the NIR range – wavelengths used for the operation of etalons in this study. By placing the PI film underneath an etalon resonator, the UV and NIR beams may overlap yet independently operate their respective transduction mechanism. As a result, transmitter and receiver can be in the same location thereby allowing complete 2-D arrays of arbitrary configuration. To date, linear endoscopic/intravascular ultrasound arrays rarely exceed operating frequencies above 10 MHz. The adoption of all-optical ultrasound

technology therefore has the potential to reveal disease characteristics presently inaccessible by any endoscopic imaging modality.

The imaging axial resolution provided by an ultrasound transducer array operating with pulse duration T is

$$\Delta z \sim \frac{v_s T}{2} ,$$

where v_s is the speed of sound of the medium. Based on the pulse-echo waveforms presented in Figure 2.17, the average pulse duration between both PI-etalon designs was approximately 50-60 ns. We can therefore expect an axial resolution in the range of 35-45 µm in water. Lateral resolution is dependent on the aperture of the transducer/array, imaging depth, and central operating frequency. Typical IVUS catheters have a diameter below 2 mm in order to be compatible with the size of peripheral and coronary arteries, so we will limit our lateral region of interest to a 2 x 2 mm rectangular aperture. The -3 dB lateral resolution in the Fraunhofer zone for a flat rectangular aperture is

$$FWHM = 2R \sin^{-1} \frac{0.6 v_s}{W f_c} ,$$

where *R* is radial distance, *W* is the aperture width, and f_c is the central operating frequency [49]. The average central frequency between both PI-etalons was approximately 43 MHz. At imaging depths of [2 4 6 8 10] mm we can then expect -3 dB lateral resolutions of approximately [42 84 126 167 209] µm, respectively.

In order to serve as a complete substitute for piezoelectric technology, all-optical arrays should be capable of receiving at any number of locations simultaneously and likewise for transmission. This would allow full phased array operation for acoustic beam steering and focusing in both transmitting and receiving stages. Multiple NIR and multiple UV beams are then required, which would add significant complexity and cost to the supporting optical system. A single NIR beam could be split into several beams provided a constant resonance wavelength at all locations, but a beam splitter and PD would be required for each channel. A single UV beam could be split in the same way, but optical multiplexing would be required to turn on and off each subsequent UV beam.

In the early 1990's, techniques using synthetic arrays for ultrasound imaging arose [50]. This typically involves spatially scanning either a single receiver or transmitter while the other is stationary in order to simulate a full array. Because many fabrication challenges and performance issues are presented when pursuing dense, high frequency arrays, synthetic arrays offer a convenient alternative. Using this method, focusing in the receiving stage can still be performed after all signals have been acquired via delay-and-sum – a method referred to as the Synthetic Aperture Focusing Technique (SAFT). However, focusing in transmission is not possible because only a single transmitter can be active at one time. As a result, both penetration depth and image dynamic range is lower than that of complete arrays. Another disadvantage is that achieving real time imaging is more difficult because one must await complete scanning of the aperture before image reconstruction can begin. Finally, the large separation of A-line acquisitions in time makes imaging with synthetic arrays more susceptible to motion artifacts.

Despite the disadvantages intrinsic to synthetic arrays, their convenience in the case of all-optical ultrasound transduction is substantial. Laser beams can be easily scanned along the transducer surface using automated translation or steering of optical components. SAFT imaging is therefore the most practical option at this time. In this chapter, we explore two types of beam scanning to form synthetic 2-D arrays for 3-D high resolution imaging. The first involves generating high amplitude acoustic transmission (> 4 MPa) by using a relatively broad UV spot (approx. 2-3 mm in diameter) that is fixed in position, and an NIR beam with 35 µm spot is raster scanned within a 2 x 2 mm area superimposed. The second SAFT method involves raster scanning a 43 µm UV beam across a 2 x 2 mm aperture for each of four different receive locations. The results presented are such that the Au/Au PI-etalon design was used exclusively for the fixed-transmitter/scanning-receiver configuration and the Die/Au design for the fixed-receiver/scanning-transmitter configuration. This is because both the Die/Au design and its associated scanning technique were hypothesized to be improvements to the imaging system and thus completed later in time.

3.3 Methods and Results

3.3.1 Imaging with Fixed-transmitter/Scanning-receiver

3.3.1.1 Scan Methods and Data Acquisition

In order to scan the NIR beam across a 2-D aperture in an automated fashion, the entire NIR optical assembly needs to be placed on an x-y-z translation stage that is motorized in the x-y plane. An illustration of the experimental setup is shown in Figure 3.1a. Linear actuators (T-LA28A, Zaber Tech.) translate the breadboard on which the NIR optics rest. The focusing lens has a 60 mm focal length, which provides enough space between the NIR optics and the etalon to accommodate an unfocused UV beam with angled incidence. The goal is to raster scan the NIR beam across an aperture that is superimposed onto the UV spot (Figure 3.1b). As mentioned, the PI-etalon used during this study had PI/Au/SU8/Au thin film layers with thicknesses of 2.5/0.05/10/0.05 μm, respectively. For imaging targets, two copper wires having a diameter of 80 μm were separated and orthogonal to each other in the imaging field. A photograph of the setup is shown in Figure 3.2.

It should be noted that the UV source used during this imaging study is different than that on which Chapter 2 results are based. Therefore the pulse-echo duration and bandwidth are once again worth presenting as they influence imaging resolution. In this case, the 355 nm optical pulse had a 6 ns pulsewidth, 2.2 mJ energy, and originated from the third harmonic of a ND:YAG laser (Surelight I, Continuum Inc.). With an incident angle of roughly 30 degrees, the area of illumination was elliptical with a major diameter of 3.3 mm and a minor diameter of 2.3 mm yielding an intensity of 36 mJ/cm^2. The amplitude of the generated pressure wave was 4.3 MPa measured at a depth of 1.7 mm. Using a glass slide as a reflective target, the Au/Au PI-etalon's pulse-echo (high-pass filtered at 2 MHz) and spectrum are shown in Figure 3.3. Pulse-echo duration is approximately 70 ns and the -6 dB spectrum extends from 2 to 48 MHz.

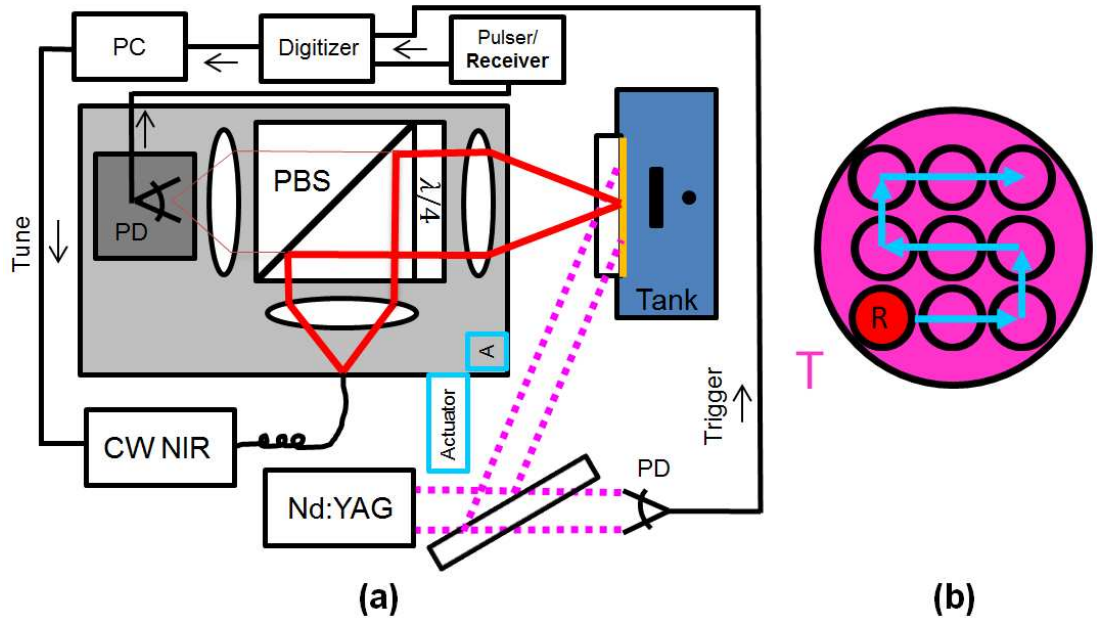

Figure 3.1. (a) Optical and DAQ system for fixed-transmitter/scanning-receiver imaging; **(b)** scan pattern for the NIR spot superimposed onto a broad UV spot.

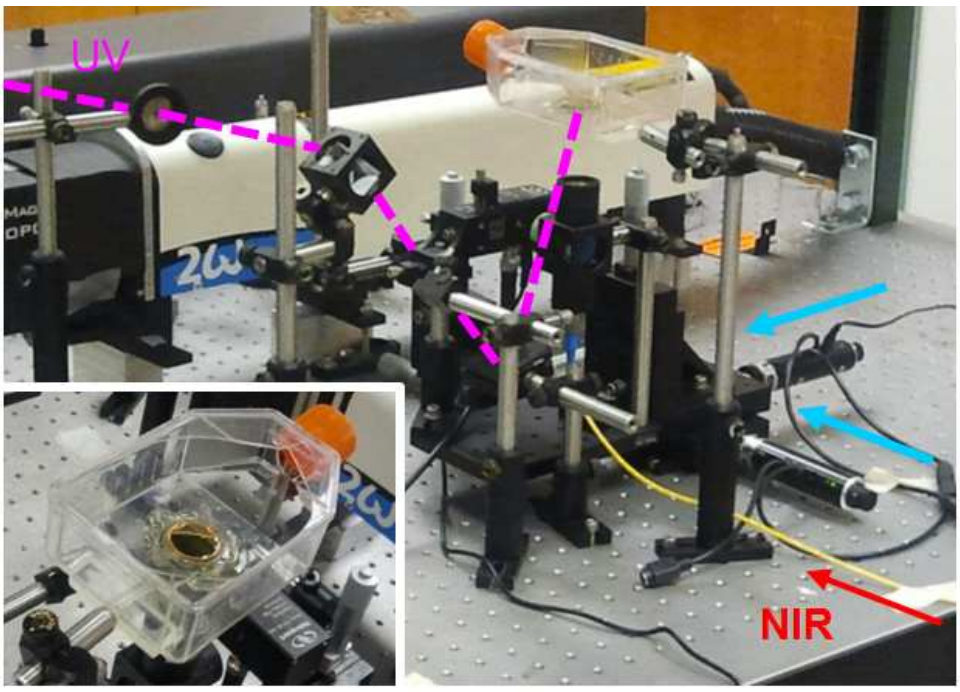

Figure 3.2. Photograph of experimental setup for fixed-transmitter/scanning-receiver imaging. Linear actuators (blue arrows) translate a stage on which the NIR optics rest. The unfocused UV beam is stationary and incident upon the PI-etalon with an angle of 30°. Also shown inset is the Au/Au PI-etalon mounted in a small plastic water tank [37] (© 2012 IEEE).

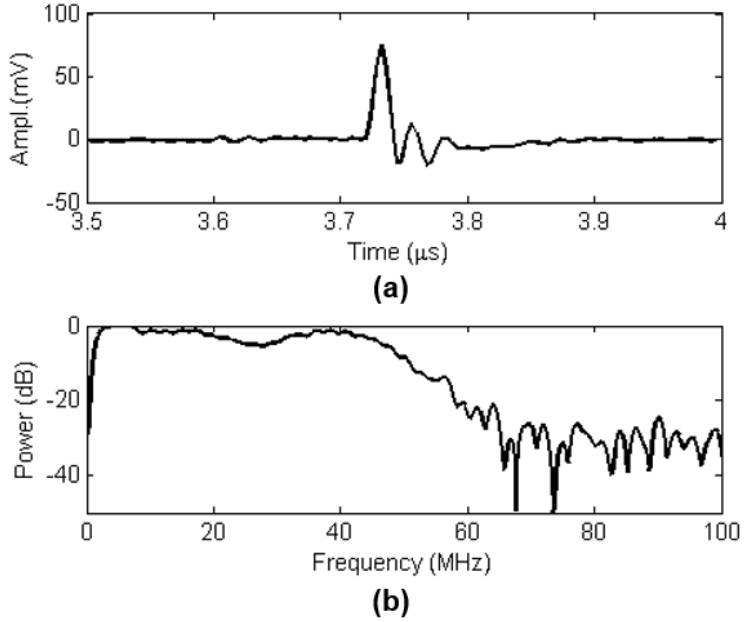

Figure 3.3. Pulse-echo **(a)** waveform and **(b)** power spectrum for Au/Au PI-etalon with Continuum Surelight I UV source.

Before imaging can be conducted, a map of the resonance wavelengths and their associated location on the wafer needs to be constructed in order to optimize receive sensitivity throughout the scan. Resonance wavelength can vary appreciably if the thickness of the etalon is non-uniform. It can also shift after immersing the device in water due to uptake of fluid in the etalon cavity. If changes in the resonance wavelength go unobserved, the operating wavelength of the optical system may deviate from the region of highest slope on the resonance curve. As a consequence, receive sensitivity can drastically change over the course of the imaging scan and be severely diminished if the shift is large. Figure 3.4 portrays the drift of the resonance wavelength across a 1 mm scan of the Au/Au transducer at 100 μm intervals. The resonance wavelength was determined across the intended 2 x 2 mm aperture using 100 μm step size and stored for the subsequent imaging experiment.

Figure 3.4. Drift of a single resonance over 1 mm at 100 micron step size for the Au/Au device.

During the imaging experiment, the NIR probe beam was scanned across the wafer through a 2 x 2 mm grid using a step size of 30 µm. Before scanning commenced, the table of resonance wavelengths as a function of beam position was loaded into the acquisition program. At each grid point in the imaging scan, the LabVIEW DAQ program searched for the closest corresponding location from which the resonance wavelength was determined and tuned the wavelength to the associated value minus 1 nm. The PD output was amplified by 50 dB using the receive function of the pulser/receiver introduced in Chapter 2. 32 waveforms were acquired at each detector location and averaged, followed by storage for post-processing. Because the PRF of the Nd:YAG laser was limited to 10 Hz, total scan time was approximately 4 hours.

3.3.1.2 Post-processing and Image Reconstruction

In addition to the forward-propagating ultrasound created in the PI layer of the device, a portion propagates backwards through the substrate whereupon it is reflected back towards the device. Additional acoustic emissions then occur corresponding to each reflection, and these emissions create additional pulse-echoes off of targets in the imaging field. These are particularly problematic when large pressures are generated as when using a broad UV spot for TUG. The first step of post-processing was to null these additional echoes by searching A-lines for peaks separated in time by the estimated propagation time through the substrate. The final step of signal processing was to digitally band-pass filter from 25 to 55 MHz. Delay-and-sum image reconstruction using SAFT was then performed as follows:

We define the waveform recorded by a receive element $[m,n]$ as $v = v(m,n,t)$, where continuous time is assumed for convenience. We also define the path taken by the emitted acoustic wave to pixel $[\alpha,\beta,\zeta]$ in the imaging field as $\overrightarrow{r_T}$ and represent the return path of a reflected wave from said pixel to a detector as $\overrightarrow{r_R}$ (Figure 3.5). In the case of a broad, unfocused UV spot, assuming plane wave propagation for transmission was found to provide the best reconstruction results, rather, $\overrightarrow{r_T} = z$ where z is referenced to the detector plane. The shape of the reflected wavefront is assumed to be isotropic/hemi-spherical, therefore $\overrightarrow{r_R}$ is a vector from the pixel to the detector. The presence of a target at $[\alpha,\beta,\zeta]$ is then indicated by the amplitude $A = A[\alpha,\beta,\zeta]$, calculated using

$$A[\alpha,\beta,\zeta] = \sum_n \sum_m v\left(m,n,t = \frac{z[\zeta] + |\vec{r}_R|}{v_s} - t_0\right) ,$$

where

$$|\overrightarrow{r_R}| = \sqrt{(x[\alpha] - x[m])^2 + (y[\beta] - y[n])^2 + z[\zeta]^2} ,$$

and t_0 is the time of peak UV energy relative to the trigger. This is followed by envelope detection using

$$h[\alpha,\beta,:] = imag[\mathcal{H}(A[\alpha,\beta,:])] ,$$

$$A_{env}[\alpha,\beta,:] = \sqrt{h[\alpha,\beta,:]^2 + A[\alpha,\beta,:]^2} ,$$

where $\mathcal{H}$ is the Hilbert transform. Finally, the data is normalized and subsequently logarithmized.

The full 3-D reconstruction of the wires can be appreciated via a -10 dB isosurface as shown in Figure 3.6a. Their relative orthogonality is clear. Figure 3.6b shows 2-D cross sections of the wires from the 3-D reconstruction with 25 dB dynamic range. We may observe two types of artifacts, both of which result in the replication of the imaging targets. The first type is duplication of the nearest wire occurring approximately 1 mm after the primary reconstruction. This is due to the imperfect removal of reflection transmissions, as additional signals are buried in noise and hence unidentifiable. A second artifact is replication of the targets immediately following the original, best exhibited by the wire at larger depth. These are likely due to the secondary and third peaks in the pulse-echo waveform shown in Figure 3.3a.

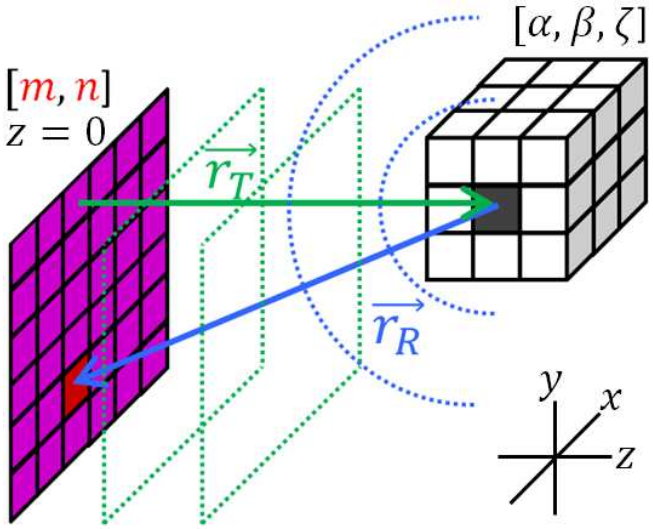
[α, β, ζ]
[m, n]
z = 0
r_T
r_R
y
x
z

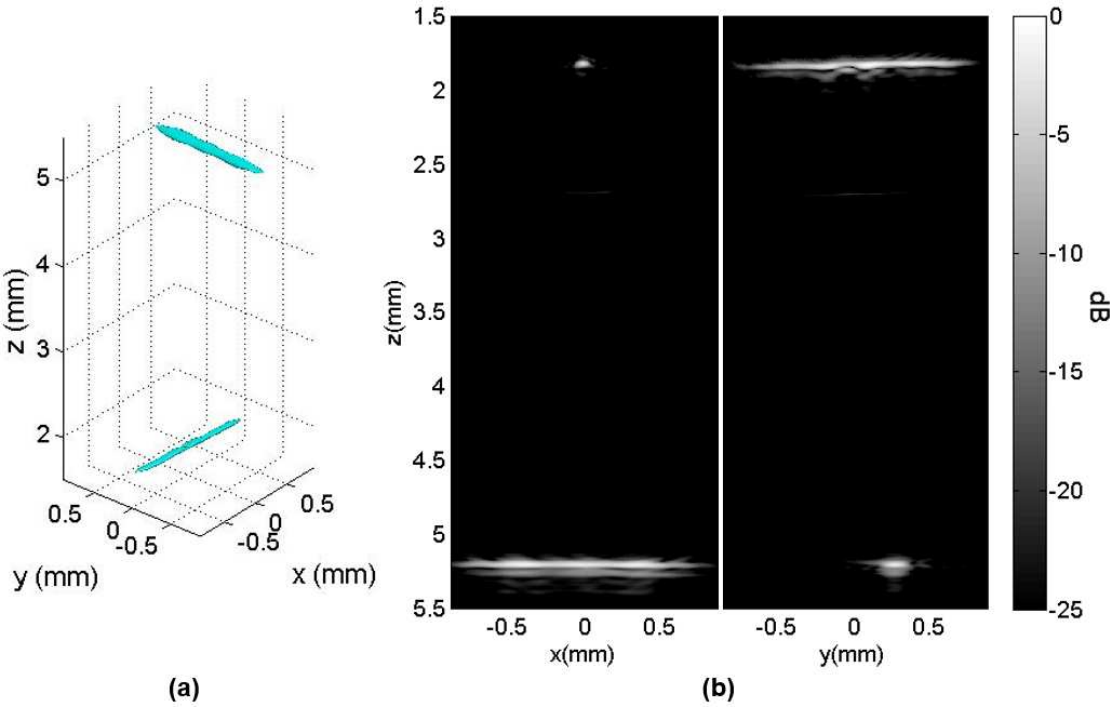
z (mm)
y (mm)
x (mm)
z(mm)
x(mm)
y(mm)
dB
(a)
(b)

We define imaging resolution by the -6 dB threshold in the reconstruction, which can be estimated by examining 1-D cross sections of the 2-D slices as shown in Figure 3.7. The full dynamic range is also better appreciated because 8-bit linear gray scale is limited to 25 dB. Background noise occurs at approximately 35 dB – a far superior result than previous attempts to image with an all-optical transducer as presented in [36]. For the wire at 1.8 mm, the estimate for the -6 dB resolution is 71 µm in the lateral dimension and 35 µm in the axial dimension. For the wire at 5.2 mm depth, the estimate is 145 µm in the lateral dimension and 38 µm in the axial dimension.

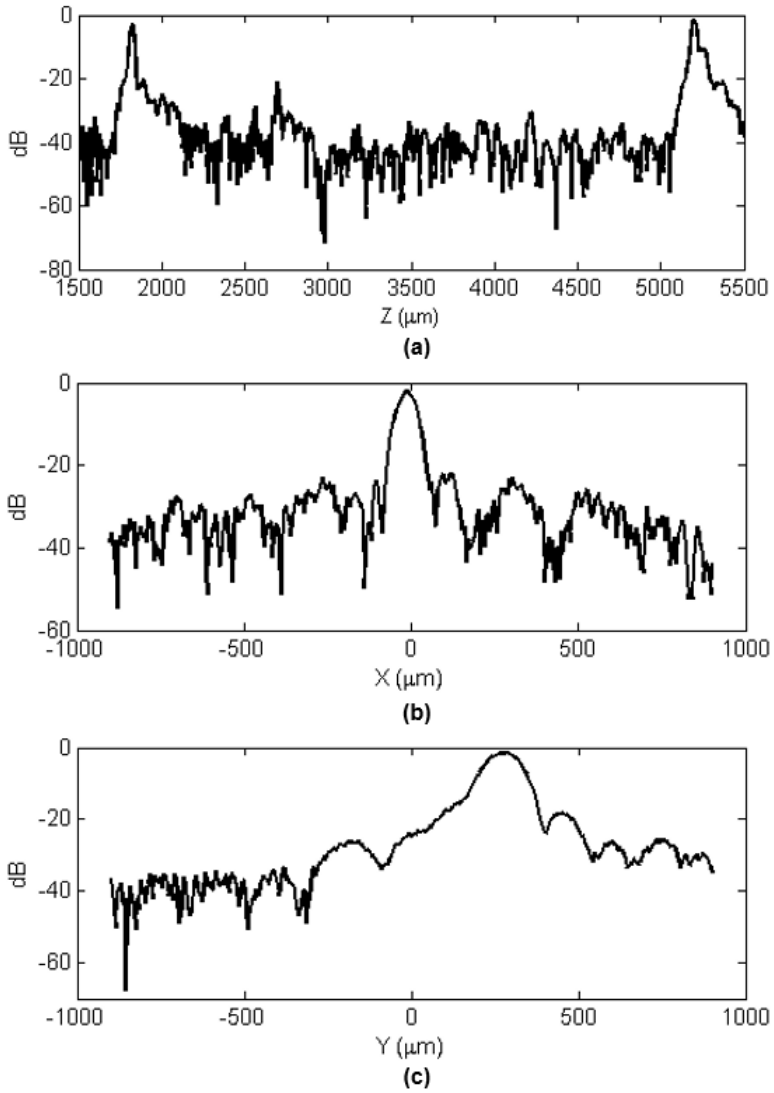

Figure 3.7. 1-D slices of 3-D reconstruction for resolution estimation; **(a)** axial slice of x-z plane in Figure 3.6b showing cross sections of both wires; **(b)** lateral slice of x-z plane in Figure 3.6b at nearest wire; **(c)** lateral slice of y-z plane in Fig. 6b at farthest wire.

3.3.1.3 Ex Vivo Imaging of Carotid Artery in Swine

To understand how the array might perform in an intravascular setting, an excised coronary artery of a healthy pig was acquired. The vessel was cut along the direction of its long axis and flattened (Figure 3.8a). The sample was then imaged with the inner wall facing the device. Because the aforementioned reflection emissions from the substrate can substantially affect image reconstruction of continuous media, imaging of the artery was performed using an Au/Au etalon fabricated on a 10 mm glass substrate. In this case, the time between the primary emission and the first reflection emission is 4-5 µs. This allows imaging within a depth of 3-4 mm without artifacts. Image reconstruction is shown in Figure 3.8b, which demonstrates the array's response to point scatterers of a turbid media. While penetration depth appears limited to approximately 500 µm, the result indicates an ability to obtain the SNR required to image organic materials found in blood vessels. Differentiation of vessel wall components would be expected in disease models containing layers of fatty and fibrous material from atherosclerotic plaque.

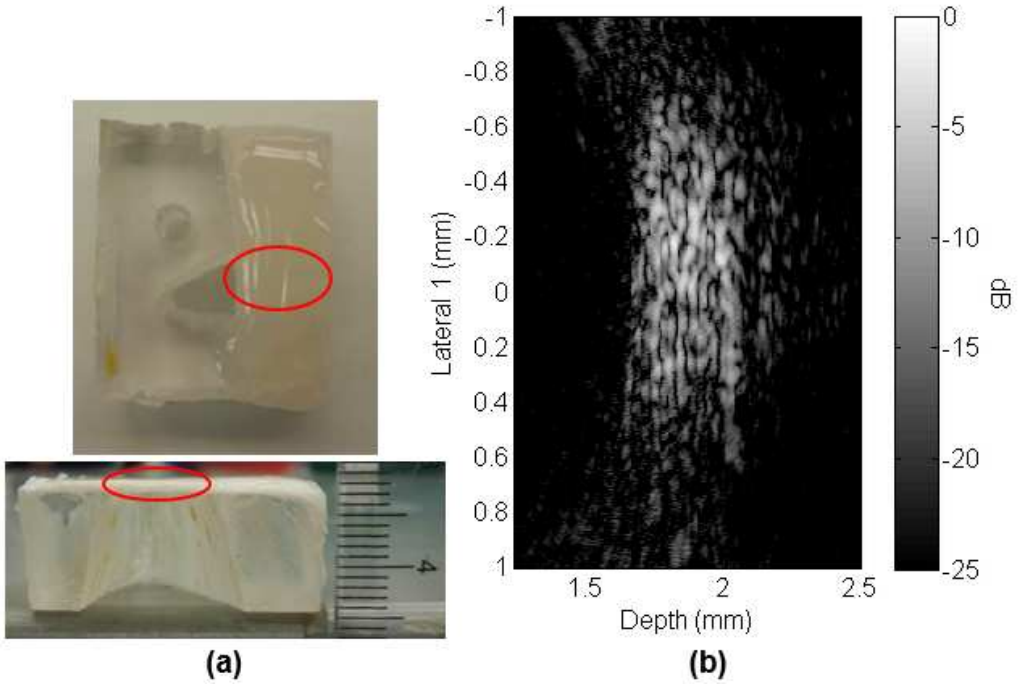

3.3.2 Imaging with Fixed-receiver/Scanning-transmitter

3.3.2.1 Scan Methods and Data Acquisition

The second beam-scanning technique for SAFT imaging entailed focusing the UV beam to create a smaller transmit element and spatially scanning it to form a dense synthetic array. This yields an ability to create both receive and transmit elements at any location. Figure 3.9 illustrates the optical system for this method, and it is photographed in Figure 3.10. UV and NIR beams are once again integrated as in Chapter 2 for pulse-echo measurements, however the actuators for automated translation of the NIR assembly are now in place, and the UV beam will be scanned at regular intervals. As a 355 nm laser source, we return to the combined 1064/532 nm output of a frequency-doubled Nd:YAG laser (LUCE, Bright Solutions) guided through a frequency-tripling crystal (LBO Type 1, Conex Systems Tech.). In addition, the 2.5-50 MHz amplifier of the pulser/receiver is again used for maximum signal amplitude. Finally, the Die/Au PI-etalon design was used exclusively under this scanning method, having layers PI/Die/PI/Au/ with 2.5/4/11/0.05 μm thickness.

An important advantage to using this scan method is that the number of receive elements can be drastically reduced while the UV beam can be scanned through a dense grid. Recall that scanning the NIR/receive beam throughout a dense grid requires predetermination of the optimal wavelength at each receive location and imposes added time to the imaging scan for wavelength adjustments. In using only a few receive locations, the required wavelength adjustments are minimal, leading to a less complex imaging procedure and a more stable sensitivity throughout the course of the scan. In addition, a rapidly scanning galvo-mirror system for the UV laser could be employed that would lower image acquisition time because there is no need to dwell at the element location. Lastly, reducing the size of the transmitter creates future opportunities to explore beam forming with a phased laser array.

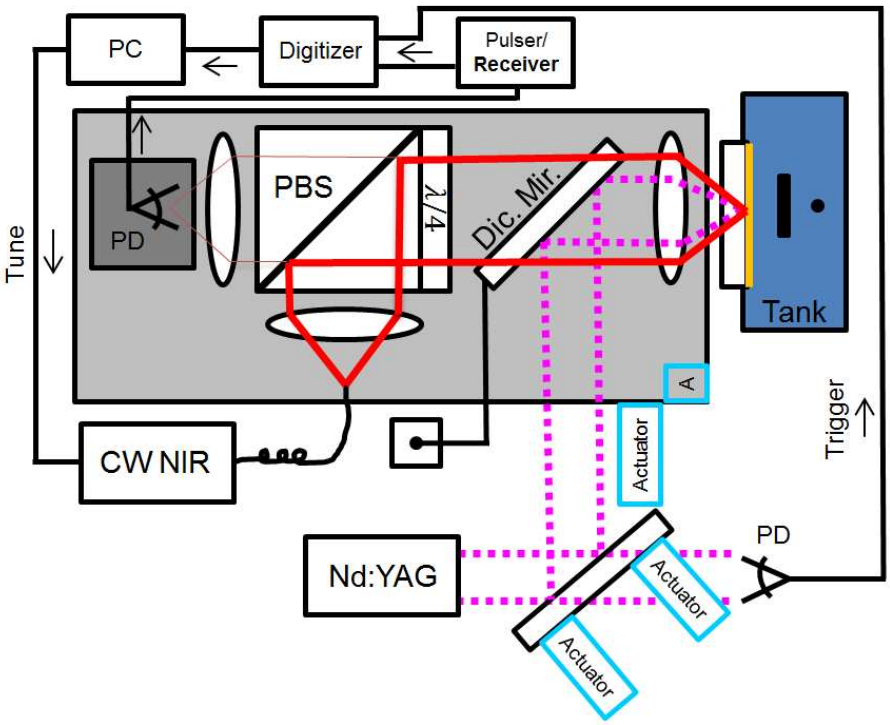
PC
Digitizer
Pulser/
Receiver
PBS
λ/4
Dic. Mir.
PD
Tune
Tank
A
Actuator
Trigger
CW NIR
Nd:YAG
PD
Actuator
Actuator

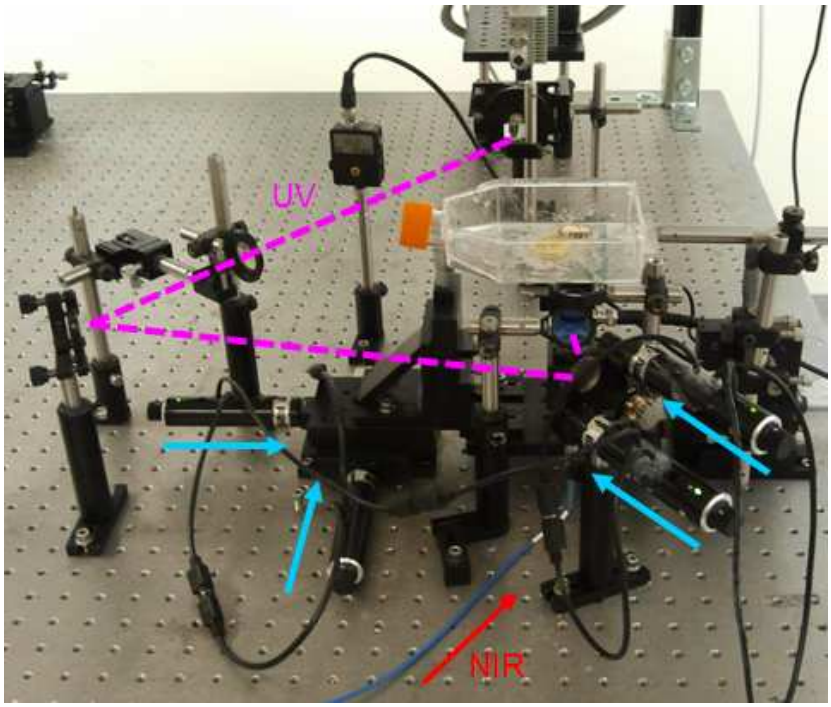
UV
NIR

There are a few disadvantages of using a dense grid of small UV spots/transmitters. The primary one is the lowered acoustic emission associated with a smaller UV spot. We have compensated for the associated loss in SNR by performing rapid averaging with high-speed signal acquisition and a laser with higher PRFs in comparison to the fixed-transmitter/scanning-receiver setup. Another issue is that translation of the focusing lens with the NIR optics (used to change the receive location) also translates the UV beam with it. Figure 3.11 shows the intended scan pattern for this study wherein we limit the number of receive locations to four, and we scan through a dense transmit grid for each receive location. If we want to use the same UV/transmit grid points for each NIR/receive location, we have to re-center that grid every time the NIR optics are translated, as illustrated in Figure 3.12.

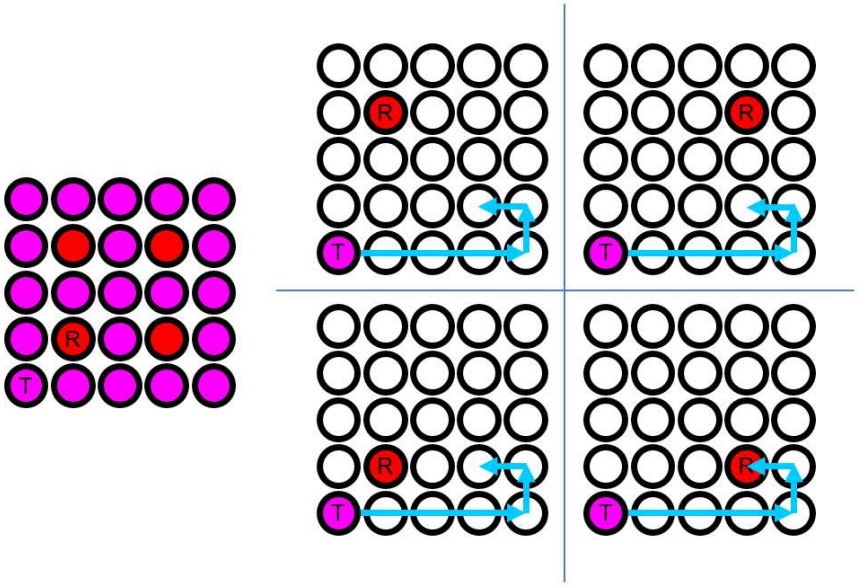

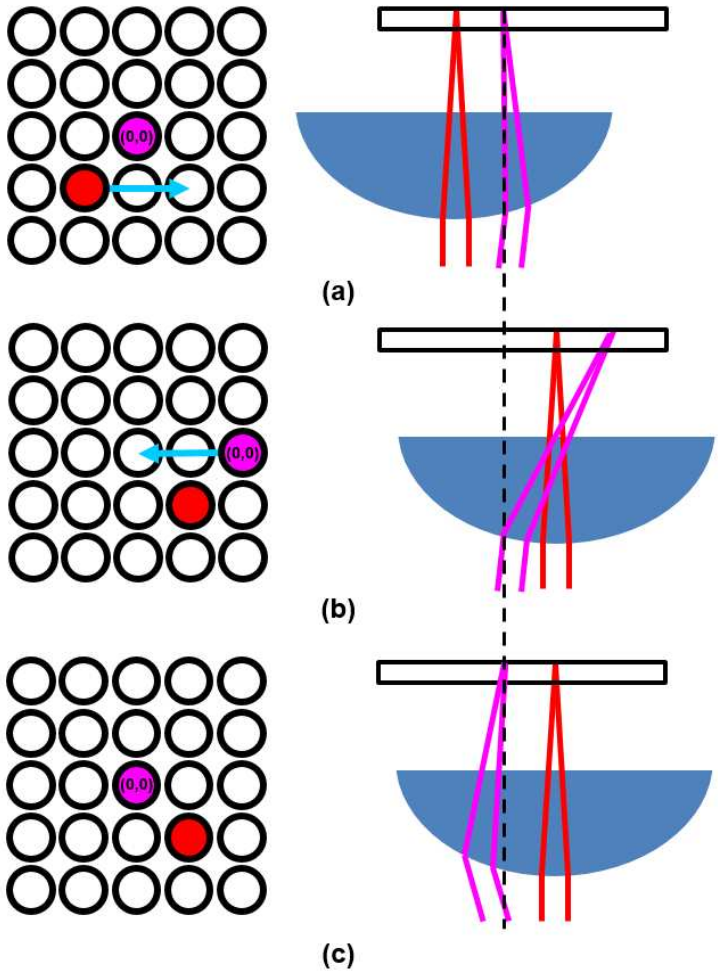

3-D imaging of two wire targets 127 µm in diameter was performed with the Die/Au device using a 2 x 2 mm synthetic aperture of 957 transmitting elements centered on a 1 x 1 mm synthetic array of four receive elements. The two 127 µm wires were oriented perpendicular to one another and roughly aligned with an axis of the UV beam scan. While the NIR beam is held at a single receive location, the UV beam is scanned across a 33 x 33 element grid. Prior to the scan, new coordinates representing the center of the intended transmitter grid (one that is centered about the array of four receive elements) were predetermined for each receive position. These coordinates were then

automatically updated when switching to a new receive position during the scan. The optimal NIR wavelength at each of four receive positions was also predetermined and programmed into the scan. At each transmit location, 1024 waveforms were amplified by 50 dB, filtered from 2.5-50 MHz, digitized at 250 MHz, and averaged prior to storage for post-processing. A UV PRF of 500 Hz was used resulting in a total scan time of approximately two hours.

Accurately knowing the locations of the UV spot during a scan – a prerequisite for high quality image reconstruction – is challenging because angular deflection of the UV beam with a mirror mount produces a rhomboidal grid with axes of different step size. Furthermore, deflection of the beam through a simple plano-convex lens creates a non-flat focal plane, which introduces scan curvature and a varying spot size. To best estimate the shape of the 33 x 33 element transmit array, the location of each element in a downsampled version (99 elements) was estimated using acoustic trilateration. The hydrophone was used to sample the field generated by each UV element at four locations laterally dispersed in the target space. The result confirms the presence of two non-orthogonal scan axes of different step size (Figure 3.13a). Because the axes of hydrophone translation coincided with those of the NIR scan, the result also demonstrates the angular offset between the UV array and the NIR array (also shown).

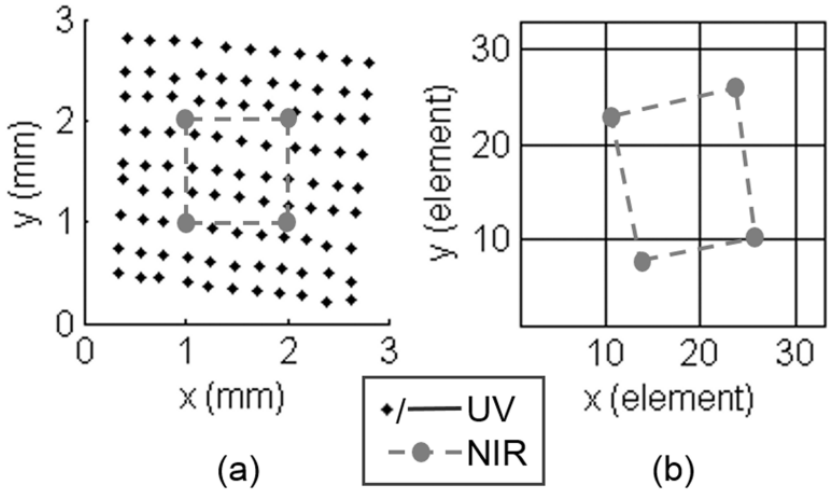

3.3.2.2 Post-processing and Image Reconstruction

During offline reconstruction, the signals were first digitally bandpass filtered in the range of 25-65 MHz. Search for and removal of pulse-echoes from secondary emissions due to substrate reflections were not required in this case because the reflections disperse laterally along the wafer when the UV spot size is small. By the time the reflections reach the surface of the device, their amplitude is negligible. For the acoustic propagation model in this imaging method, we assume isotropic propagation for both transmit and receive wavefronts (Figure 3.14). In this case, the target presence in a voxel of the imaging field is

_____

where

_____

and

_____

where coordinates correspond to a single transmitter location.

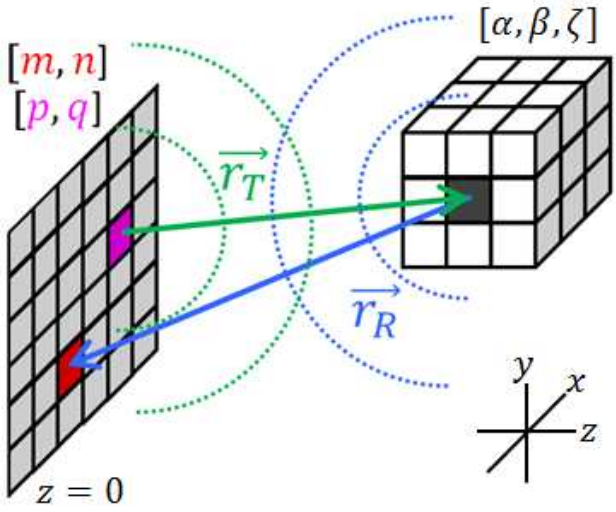

Ideally, transmit element locations and would be determined by trilateration results, however the method's accuracy is currently insufficient. A basic linear array that was assumed to represent the UV grid during reconstruction is shown in Figure 3.13b. The relative position of the four receivers ( ) can be known by identifying A-lines with the strongest thermoelastic signal. The error in using the assumed grid manifests in a receive grid that is not square and equally distributed about the center. A -10 dB isosurface of the 3-D reconstruction with 7 μm voxel size is shown in Figure 3.15a. Figure 3.15b shows two planes of the 3-D reconstruction in which the front and back side of the wires can be observed. Assuming a UV step size of 72 and 64 μm for the two UV axes, respectively, yielded the best result. From these images, estimates of -6 dB resolution were obtained: 70 μm lateral and 32 μm axial at a depth of 2.4 mm and 114 μm lateral and 38 μm axial at a depth of 5.8 mm. Background noise occurred at approximately -30 dB.

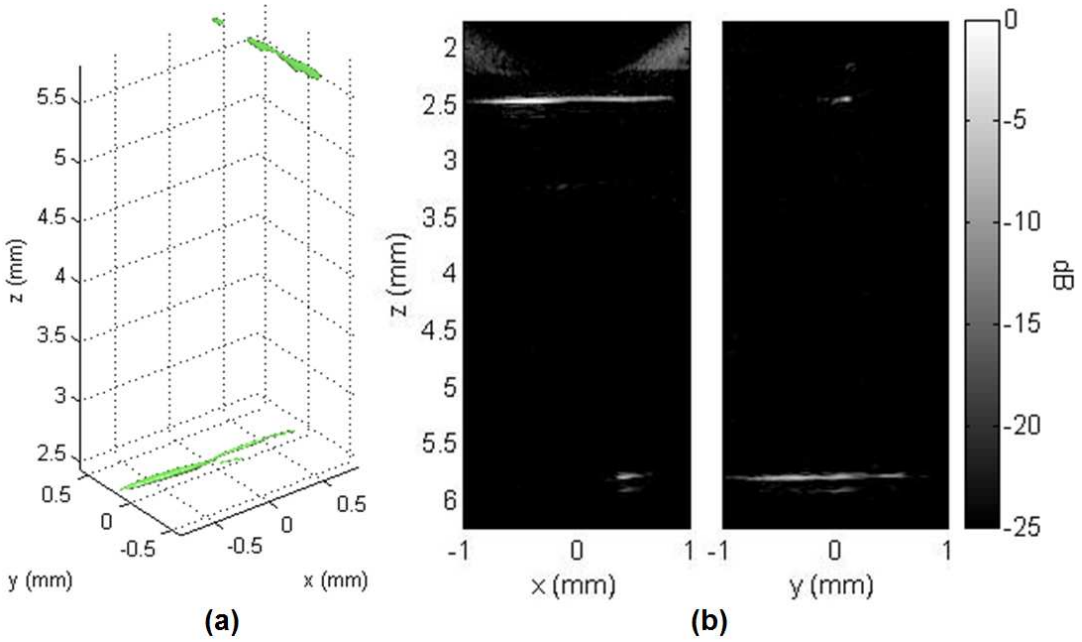

A smearing artifact typical of backprojection algorithms is present, as seen before the nearest wire. The source of these effects can be better understood by comparing the independent reconstructions of data taken at single receive positions. Figure 3.16a shows the reconstruction of the nearest wire using data collected only by a single receiver positioned at x = -500 μm. Figure 3.16b shows that for the receiver positioned at x = 500 μm. Each receiver appears to capture a pulse-echo only within a vicinity of ±500 μm (lateral) from its position at this depth, and outside of this vicinity reveals the waveform summing of the reconstruction algorithm where the target is not present. Figure 3.16 also reveals that the orientation of the reconstructed wire differs between receivers, which may be a consequence of using the model in Figure 3.13b. When both data sets are summed to create Figure 3.15b (along with data from the remaining two receivers), redundant information between receivers, i.e. echoes received from the same portion of the wire, fail to sum properly. This reduces dynamic range that in turn raises background levels, including the smearing artifact, and warps the reconstruction of the target.

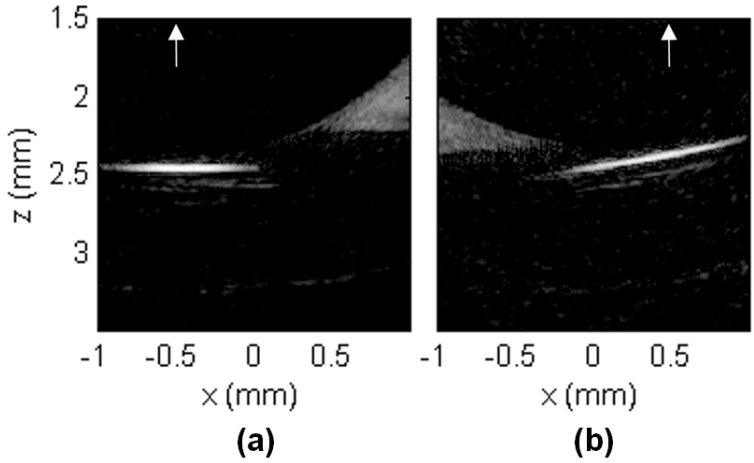

The complete thermoelastic response of the PI-etalon to the absorption of the UV pulse is best characterized in Figure 3.17a. This figure contains pixelated A-lines recorded by a single receiver for one dimension of the UV scan path. Overlap of the UV and NIR spots is indicated by the earliest and longest-lasting waveform detected (at approx. -500 µm). The signal pattern radiating laterally from this point might correspond to flexural plate waves excited in the dielectric layer. While the presence of these signals aid in image reconstruction by designating the location of the receivers, they become problematic when transmitter and receiver are separated by large distances. In this case, the signals dominate the pulse-echo response with substantial delay (≈ 1 µs) thereby overshadowing any echoes reflected from targets within a depth of approximately 1 mm. Figure 3.17b shows the average power spectrum of the A-lines presented in Figure 3.17a. The central frequency of these signals is 20 MHz with a -6 dB bandwidth of 120 % – a frequency range not easily suppressed by filtering without attenuating the signals of interest. Also depicted in Figure 3.17a is a reflection of the backwards-travelling acoustic pulse by the rear surface of the 3 mm glass substrate, represented by the vertical lines near t = 1.1 µs. Vertical bars near t = 0 correspond to trigger interference.

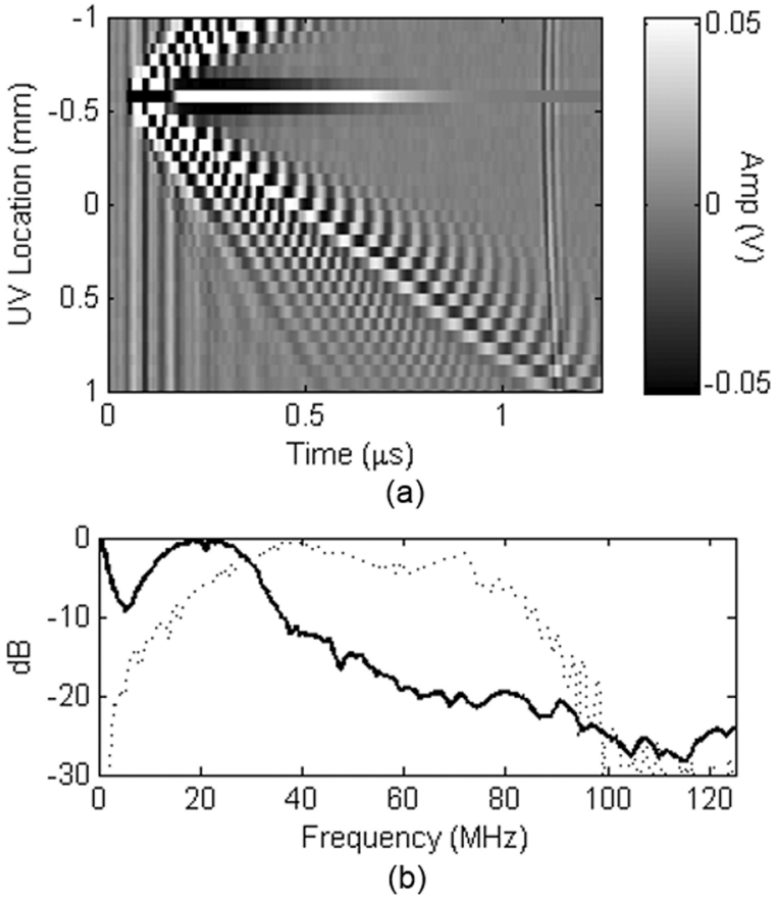

3.4 Discussion

We have demonstrated here the basic imaging capabilities of a PI-etalon transducer with two beam-scanning methods for a synthetic aperture. Using a 2 x 2 mm synthetic array of 35 μm receive elements and a broad UV spot, we obtained estimates of 35/38 μm and 71/145 μm at a depth of 1.8/5.2 mm for the axial and lateral resolution, respectively. Using a dense, 2 x 2 mm synthetic array of transmitters centered on a 1 x 1 mm synthetic array of four receive elements, results indicate a lateral resolution of 70 μm and

114 μm at depths of 2.4 and 5.8 mm, respectively, with an average axial resolution of 35 μm. Results from both imaging configurations correlate well to the expected resolutions presented in the introduction, and they mark an advance in the ability of an all-optical device to provide the dynamic range needed for high resolution ultrasound imaging.

Both imaging configurations presented here have advantages and disadvantages. With a broad UV spot and dense receive (NIR) array, acoustic output is easily greater than 1 MPa, which maximizes SNR. In addition, the propagation model for image reconstruction is more accurate with the fixed-transmitter/scanning-receiver because the exact locations of each receive element are predictable, which improves image quality. However, receive sensitivity is unstable due to a severe variation in resonance wavelength across the wafer. It is therefore likely that the user would have to calibrate often by finding the resonance wavelength for each of many receive locations so as to avoid significant drops in sensitivity. Finally, frequent translation of the entire NIR optical assembly may introduce alignment errors. Specifically, the device plane may drift out of the NIR focal plane, and coupling of the reflected NIR beam to the PD may shift away from optimal alignment.

Scanning the UV beam for a dense array of transmitters is advantageous in that there is no need for frequent wavelength adjustments. Furthermore, maintaining alignment is less critical because the NIR assembly is only translated to a small number of positions for receiving. Consequently, a high-speed galvo scanner can be integrated into the setup to do the bulk of the beam scanning. Using a galvo for the NIR beam is much more challenging because of the need to capture the reflection. The primary disadvantage in using a fixed-receiver/scanning-transmitter configuration is the lowered acoustic output associated with a small UV spot size. This diminishes SNR thereby requiring a high level of averaging. In addition, precise determination of the transmitter locations across the scan aperture for an accurate propagation model is difficult in the scanning-transmitter arrangement. The grid of elements in the 2-D scan is not rectilinear, and the pitch varies throughout. These factors ultimately degrade image quality during reconstruction because of (1) errors in estimating the propagation time to and from a pixel in the field of view and (2) ineffective summing of datasets between individual receivers whose UV coordinate systems are not the same.

At this time, we believe that the potential speed of the scanning-transmitter/fixed-receiver arrangement warrants our focus, as real-time imaging is the final goal. Also its disadvantages may be mitigated by various techniques. As mentioned in Chapter 2, SNR can be enhanced by increasing UV illumination uniformity, spot size, and pulse duration. Lateral confinement of the etalon resonator will also increase SNR. Though modifications of this nature will create additional alignment challenges, maintaining only a few receivers that are fixed in location would limit them.

A more predictable UV scan grid could be achieved by modifying the system optics. Figure 3.18 illustrates the detriments of scanning with a conventional lens compared to different types of scanning lenses. Using a simple achromatic lens results in a non-flat focal plane (Figure 3.18a). Spot size and the scanning step size are therefore inconsistent. Flat-field scanning lenses (Figure 3.18b) resolve this issue, but scan length isn't linear with input angle (step $= f \tan\theta$). F-theta lenses (Figure 3.18c) add elements such that the relationship between incident angle and step size is linear, while telecentric f-theta lenses (Figure 3.18d) accomplish the same feat while maintaining a beam that is always orthogonal with the focal plane. In our case, the desired scan field is less than 5 x 5 mm. If we choose to maintain a lens focal length in the range of 30-60 mm, the maximum scan angle is less than 10°. At this angle, $f\theta \approx f \tan\theta$ and the telecentric lens would be of less benefit. Moreover, a single-element scan lens is desirable because it would (1) allow for less distance between the NIR PBS and focusing lens (optimal for maintaining NIR alignment) and (2) reflect less energy at wavelengths for which it is not designed (less components = less reflections). Regarding the latter feature, scanning lenses supporting such a broad wavelength range (355-1550 nm) do not exist. Because we currently have less NIR energy to spare, the best choice might be a flat-field scanning lens for 1550 nm and to accept energy losses at 355 nm. However, it is unknown to what degree a flat focal plane will be maintained at 355 nm. If an NIR source with higher power is obtained, a lens designed for 355 nm will likely be best.

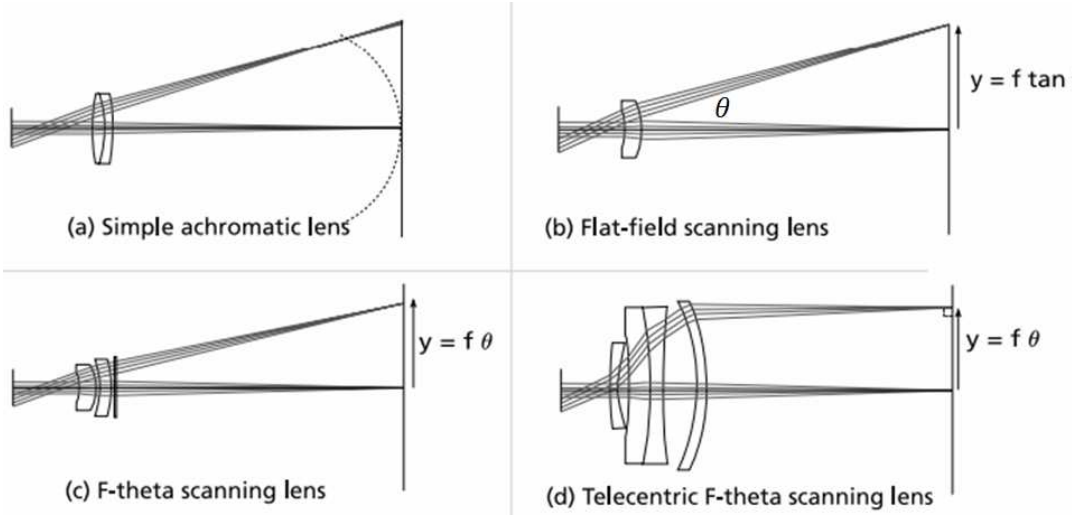

Transitioning to non-metallic targets such as tissue will introduce higher demands on SNR, therefore the aforementioned modifications might be necessary. If SNR is still insufficient, we might revert to the fixed-transmitter/scanning-receiver configuration with broad UV spot for higher acoustic output. We anticipate that creating a fiber optic-equivalent of our device for *in vivo* use will be challenging and place further constraints on SNR. Coupling the laser beams to a fiber bundle will limit the optical energy available as well as the shape and density of the arrays.

An obstacle that may generally prevent the adoption of all-optical ultrasound imaging is the scan time associated with synthetic apertures. When using the PXI acquisition card in the fixed-receiver/scanning-transmitter study, the maximum trigger rate when sampling 10 μs of data at 250 MHz is approximately 2.5 kHz. Assuming that large gains in SNR can be achieved and the scan is limited purely by data acquisition parameters, performing 32 averages (versus 1024) with a 2.5 kHz PRF (versus 500 Hz) would reduce scan time from two hours to 50 seconds. Without gains in SNR, a field-programmable gate array could be employed to perform a high level of averaging thus reducing data transmission over the PXI bus. This would allow for a PRF beyond 2.5 kHz. It is also possible to lower the density of the UV grid and incorporate multiple NIR lasers to reduce scan time. Decreasing the density by a factor of two (255 elements versus 957) and using four NIR laser systems would further lower scan time to 4

seconds. At this time scale, the mechanical scan rate of the actuators can also be a limiting factor. Modern galvo scanners can scan at a rate below 1 ms per step. In this case, scanning through a 957-element array once would take 1 second. Time for image reconstruction should also be addressed. Producing a single 2-D slice with our 64-bit, 3.4 GHz quad-core PC took 33 seconds. Halving the UV-grid density reduces reconstruction time to 10 seconds, however background levels in the image increase from -30 to -25 dB. Utilizing GPU processing and an increased pixel size would lower it to below 1 second. Additional ways to increase frame rate might be to introduce sparse arrays or add frequency-domain SAFT reconstruction [52].

Chapter 4

Fiber Optic Etalon for Photoacoustic Imaging

4.1 Overview

In this work we present the fabrication and testing of a fiber optic ultrasound sensor based on etalon technology. In between two Au mirrors, SU-8 polymer was spray coated onto the face of a single mode (SM) fiber to form the etalon medium with 13 μm thickness and a finesse of 22. Using a broadband signal to evaluate its performance, the sensitivity was 11.6 kPa over a 47.5 MHz bandwidth, or 1.7 $Pa/Hz^{1/2}$ with a -3 dB bandwidth of 27 MHz centered at 28 MHz. We propose the development of a rectilinear ultrasound array based on this device. The design entails the bundling of several fiber etalons which, when combined with photoacoustic excitation, would yield a flexible and compact, forward-viewing photoacoustic endoscope. To simulate the performance of a bundled device, we have mechanically scanned a single fiber etalon to image simple photoacoustic targets. The results demonstrate the viability of using a fiber optic-based photoacoustic endoscope to image optically absorptive structures such as blood in vasculature. Potential applications for our device include the monitoring of angiogenesis and hypoxia, which are early markers of tumor formation.

4.2 Introduction

Photoacoustic imaging (PAI) is a versatile modality that has been used in a variety of medical applications involving both anatomical and functional visualization of biological processes. The positive attributes of this modality include the high-specificity of optical imaging and the high resolution and low scattering of ultrasound imaging. By choosing a particular irradiation wavelength, specific structures can be selected for imaging with high contrast due to their characteristic absorption at that wavelength. Blood for example is highly absorptive of green light, and the imaging of microvasculature has been demonstrated by several research groups using PAI [53-55]. These structures, owing to their micro-scale dimensions, emit high-frequency ultrasound waves (> 20MHz). In

addition to a choice of morphology, PAI can be tailored to image the distribution of oxygen in tissue thereby revealing spatial information on metabolic processes [56].

4.2.1 Angiogenesis

Angiogenesis is vital for the formation, growth, and survival of tumor masses in cancer [57]. Several pharmacological mechanisms have been employed in attempting to prevent or reduce the formation of vasculature required for tumor growth as part of a therapeutic regimen. The predominant method has been to target the signaling pathways of vascular endothelial growth factor (VEGF) [58], and several drugs such as Bevacizumab have been approved by the Food and Drug Administration (FDA) as safe and effective treatments for anti-angiogenic therapy [59]. However, monitoring the microscopic effects of these treatments *in vivo* has proven to be challenging with conventional vascular imaging techniques such as dynamic contrast-enhanced (DCE-) MRI or X-ray CT [60]. Evaluating angiogenic criteria including microvascular density and vascular heterogeneity escape the resolution of these techniques and often require histological examination. PAI is a valuable compromise between the invasive surgery required for histological analysis and the limited resolution of DCE-MRI/CT. An endoscopic method could potentially facilitate repeated access to cancerous areas for the three-dimensional imaging of microvasculature. PAI could therefore prove useful in characterizing angiogenic activity and thus the effectiveness of angiogenesis inhibitors in curtailing tumor growth.

4.2.2 Hypoxia

Cancerous tissue has been shown to be significantly more hypoxic than normal tissue due to poor vascularization. While hypoxia in normal tissue typically results in programmed cell death, cancer cells often respond by overexpressing hypoxia-inducible factor 1 proteins (HIF-1) which has been correlated with increased tumor growth, metastasis, and recurrence [61], [62]. Hypoxia furthermore increases resistivity to radiation therapy due to the role oxygen plays in enabling the free-radical damage of DNA [63]. Because chemotherapy specifically targets rapidly proliferating cells, the slowed rate of cell growth resulting from hypoxia also limits response to treatment.

Hypoxia therefore has arisen to be a factor in cancer prognosis as well as a predictor of treatment viability, and it can be estimated by measuring pO_2. Techniques such as fMRI, F19-labeled MRI, and positron emission tomography (PET) have been used to image hypoxia, however they only provide qualitative measurements of pO_2 and are moreover a costly option for repeated studies [64]. The detection of pO_2 via Photoacoustic Lifetime Imaging (PALI) is a method pioneered by our group [65], [66]. This method entails a double-pulse excitation of oxygen-sensitive dyes to produce an acoustic signal from which absolute pO_2 can be inferred. With the addition of a dye-administering channel, PALI could be integrated into our design for a photoacoustic endoscope. It could therefore be used *in vivo* for high-resolution imaging of pO_2 in combination with vascular imaging. The ability to endoscopically image both the degree of hypoxia and states of angiogenesis in cancer patients with a single device could prove to be a powerful diagnostic tool in the staging, treatment, and monitoring of malignant growths.

4.2.3 Photoacoustic Endoscopy

Photoacoustic Endoscopy (PAE) is a new imaging modality that can provide high-resolution vascular imaging *in vivo*. Yang et al. have created the first photoacoustic endoscope, consisting of a radially scanning probe combined with linear translation in order to perform 3-D vascular imaging [67], [68]. However, the rigidity of the device's 48 mm-long probe head may significantly limit the number of viable endoscopic applications due to a requisite flexibility for fine guidance. Radial devices are also restricted in that they cannot image areas directly in front of the probe as with traditional endoscopes. In this work, we demonstrate an alternative design for PAE based on fiber optics for the purposes of creating a flexible, forward-viewing imager. This device design could be used to navigate through both lumen and body cavities with minimal invasiveness. We will moreover use 532 nm optical pulsing for photoacoustic excitation and thus perform vascular imaging, as blood is highly absorptive at this wavelength.

For the development of a forward-viewing photoacoustic endoscope, we propose the inclusion of etalon transducers for high-frequency detection. Unlike other existing technologies, these sensors maintain high sensitivity at high frequencies despite a reduced transducer size. Furthermore, the simplicity of etalon receivers makes them

highly miniaturizable, and a few groups have successfully fabricated etalons onto the tip of optical fibers to be used for low-field acoustic detection [69]-[72]. Our design entails the fabrication and bundling of several fiber etalons to form a high-frequency ultrasound sensor array for high-resolution imaging. The conjoining of a fiber etalon bundle with one or several fibers that transmit optical pulses would serve as a flexible and compact photoacoustic endoscope. Previous etalons created by our group have been shown to have bandwidths above 50 MHz [16], which corresponds to an axial imaging resolution of 30 µm. At this scale, our endoscopic device would prove useful in vascular and functional imaging *in vivo*.

4.3 Methods and Results

4.3.1 Fabrication

Nanofabrication techniques are commonly used to construct optical resonators of small thickness, and these techniques were used to deposit the etalon's layers onto the tip of an optical fiber. A standard SM fiber was stripped to its 120 µm cladding and cleaved to provide a flat surface on which to fabricate the etalon. Electron-beam evaporation was then used for deposition of the first etalon mirror. A 3 nm titanium adhesion layer was first evaporated onto the tip of the optical fiber followed by a 30 nm layer of gold for high reflectivity. SU-8 photoresist was chosen for the optical medium due to the polymer's high compressibility and thus sensitivity to acoustic pressure. Microchem's MicroSpray was used to manually spray coat SU-8 after deposition of the first mirror. An approximate thickness of 10 µm has shown to provide an optimal tradeoff between bandwidth and sensitivity in previous etalons [18], and a single spray of MicroSpray was found to have deposited a 10-15 µm layer of SU-8 at the fiber tip. Due to the surface tension of the cylindrical fiber, the shape of the layer formed is convex. After deposition, the layer is cured and exposed to UV light to initiate cross linkage. Finally, a second mirror was evaporated in order to complete the construction of the resonator (Figure 4.1 inset).

4.3.2 Characterization

4.3.2.1 Optical Resonance

To measure the optical resonance of the etalon, a wavelength-tunable CW NIR laser (Agilent HP 8168F) was connected to a fiber optic circulator (FOC) (Thor Labs 6015-3-FC) at port 1 (Figure 4.1). Port 2 was connected to the fiber optic etalon with an FC-FC connector, and the reflected signal is routed through Port 3 and detected by a 125 MHz PD (New Focus 1811-FC) that has both AC (> 25 kHz) and DC (< 25 kHz) outputs. The DC output was monitored by a multimeter. The resonance profile can be observed in Figure 4.2. The optical finesse was approximately 22. Given the FSR of approximately 100 nm as seen in the resonance curve, the thickness of the cavity can be estimated using

_____ _____

where and are the wavelengths at resonance and is the index of refraction. The reflected power is lowered due to the reduced coupling and attenuation by the fiber optic circulator; an input power of 2 mW at 1550 nm yielded 1.05 mW returned for the fiber, whereas 1.25 mW was detected using the free space/wafer setup.

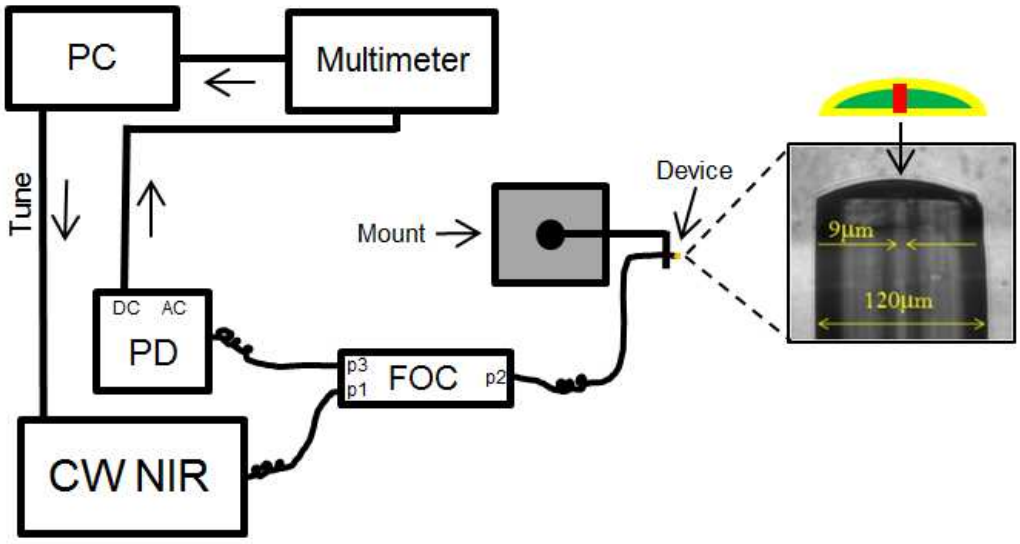

4.3.2.2 Acoustic Performance

In order to evaluate its acoustic performance, the fiber etalon was submerged in a water tank and placed near a 100 nm chromium thin-film irradiated with a 3 ns, 532 nm laser pulse generated by a Nd:YAG laser (Bright Solutions LUCE). The setup is shown in Figure 4.3. A photoacoustic source was chosen because it produces a broad band signal suitable for evaluating the frequency response of the etalon. In addition, alignment of the etalon with such a source is significantly easier with a fiber device compared to the wafer design. To achieve maximum sensitivity, the wavelength of the IR beam was adjusted to that corresponding to the point of minimum slope on the falling edge of the resonance curve. The AC output of the PD was then sampled at 250 MHz with an 8-bit digitizer (PXI-5114, National Instruments Corp.) and averaged 1024 times with no amplification.

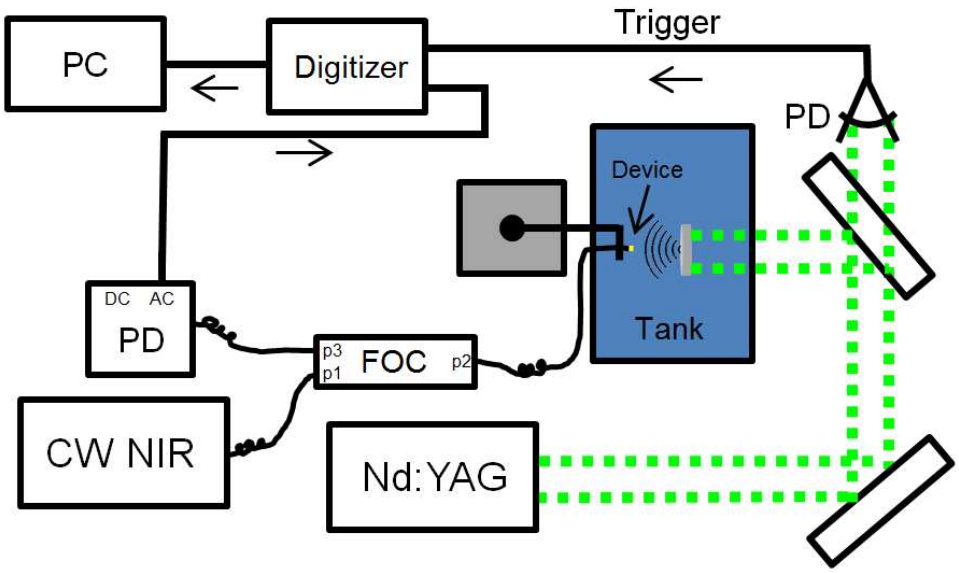

Figure 4.4b shows the temporal waveform detected by the fiber etalon. Because the metallic film is very thin, the acoustic field generated conforms to the energy profile of the optical pulse, as seen in Figure 4.4a. The first bipolar oscillation present in Figure 4.4b corresponds to what is expected in this case, but several oscillations occur thereafter. These are likely due to additional resonant modes (mechanical) occurring in the convex polymer slab, which are represented by the periodic dips in the waveform's power spectrum (Figure 4.4c). Overlaid on this spectrum is that for the same waveform but truncated after the first oscillation – a more ideal response that can be expected from a flat thin film. The center frequency of this spectrum is 27.5 MHz with a -3 dB bandwidth of 27 MHz or 98 %. The NEP was determined by measuring the maximum pressure generated by the irradiated film using the calibrated hydrophone (Onda HGL-0085). The NEP was 11.6 kPa over a 47.5 MHz bandwidth or 1.7 $Pa/Hz^{1/2}$ – slightly higher than the 1.3 $Pa/Hz^{1/2}$ obtained using the wafer etalon (~9 kPa). This is likely due to the reduction in reflected power caused by increased attenuation in the FOC.

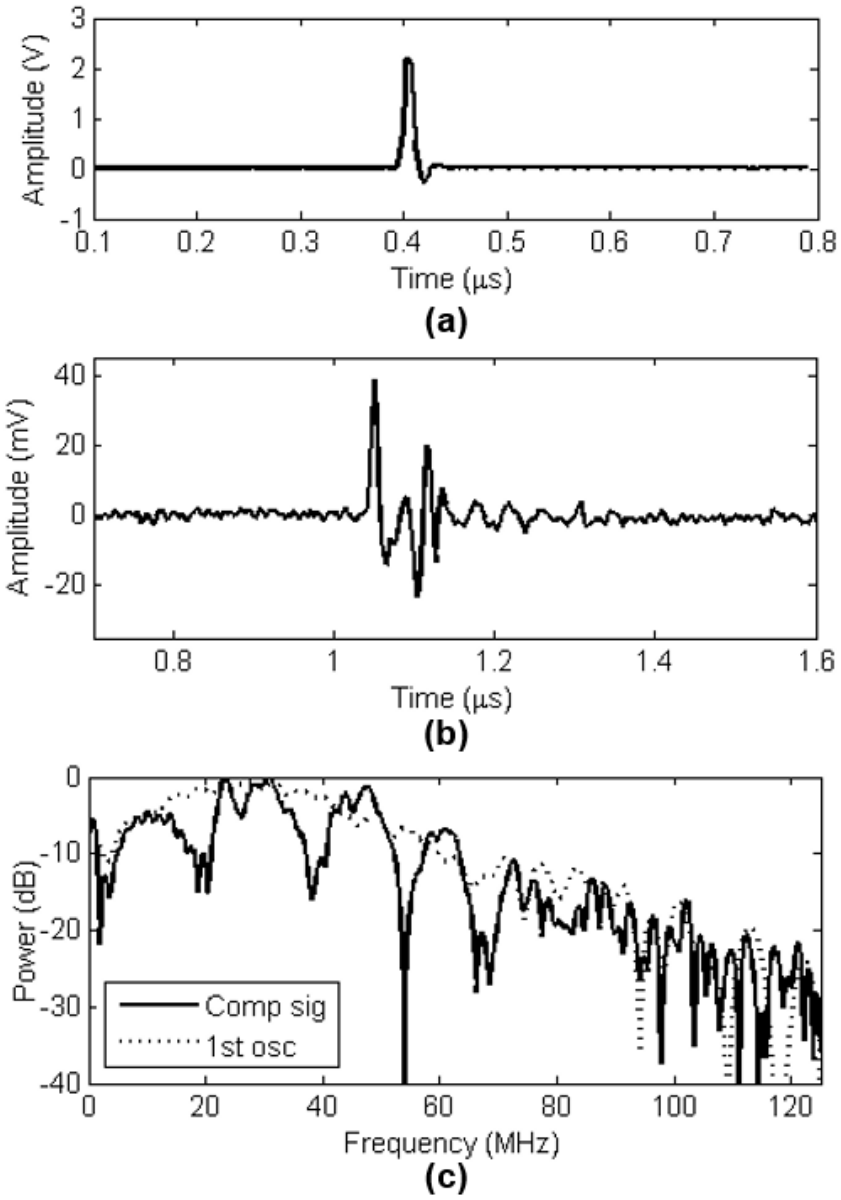

Figure 4.4. (a) Energy profile of the optical pulse that generated the **(b)** TUG waveform detected by fiber etalon. The waveform's spectrum is shown in **(c).** Overlaid on the spectrum is that for the waveform in (b) truncated after the first bipolar oscillation.

To verify that the extra oscillations in the chromium waveform were due to additional mechanical modes in the curved etalon cavity and not a part of the actual acoustic field, a 25 MHz transducer (active area: 12.5 mm; focal length: 25.4 mm; V324, Olympus NDT Inc.) driven by a pulser/receiver (bandwidth: 50 MHz; DPR300, JSR Ultrasonics) was

used as an acoustic source. The reflection of the transmitted acoustic signal off of the etalon face is shown in Figure 4.5a, and that detected by the etalon can be observed in Figure 4.5b. The etalon signal was amplified by the pulser/receiver using the same settings for the echo. Oscillations additional to those in Figure 4.5a are clearly present, indicating modulation of the true acoustic waveform received.

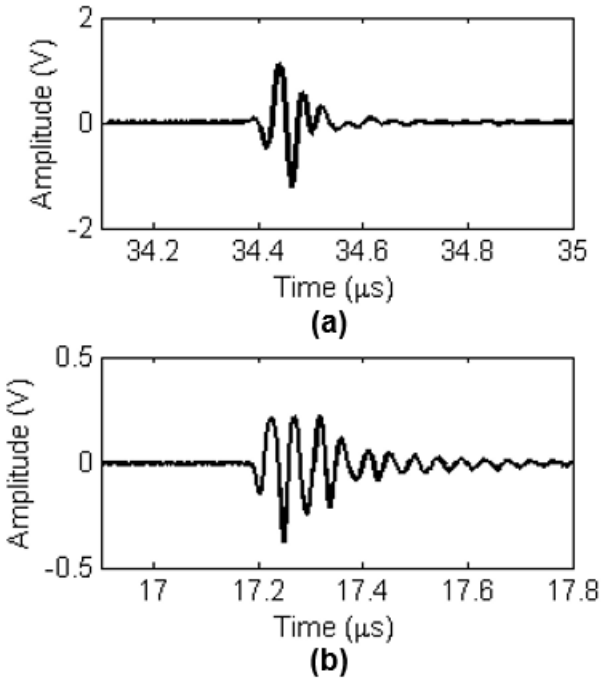

Figure 4.5. (a) Pulse-echo of 25 MHz probe reflected off of fiber etalon and **(b)** the waveform detected by the fiber etalon.

4.3.3 PAI with a Synthetic Aperture

In an effort to estimate the performance of a fiber etalon bundle in the imaging of photoacoustic targets, the fiber etalon was translated in a 2-D plane parallel with the target plane by connecting linear actuators to the Cartesian translation stage on which the device is mounted (Figure 4.6). Illumination of targets for photoacoustic excitation was fixed during the scan, and the pulser/receiver was used to amplify the AC output of the PD. The first target imaged was a black polystyrene sphere of diameter 50 μm embedded in agarose gel. The sphere was illuminated using a 532 nm optical pulse at a

1 kHz PRF to allow for fast averaging. During the scan, a 1 mm x 1 mm plane was traversed above the bead at 30 µm intervals. This corresponded to a hypothetical array of 1225 elements. Image reconstruction was then performed using Equation 3.1 with . Signals were first filtered using a 2.5-50MHz asymmetric FIR filter. The diameter of the reconstructed bead according to the three dimensions x (lateral), y (lateral), and z (axial) was approximately 75, 125, and 200 µm, respectively (Figure 4.7). Illumination was incident from the positive y direction.

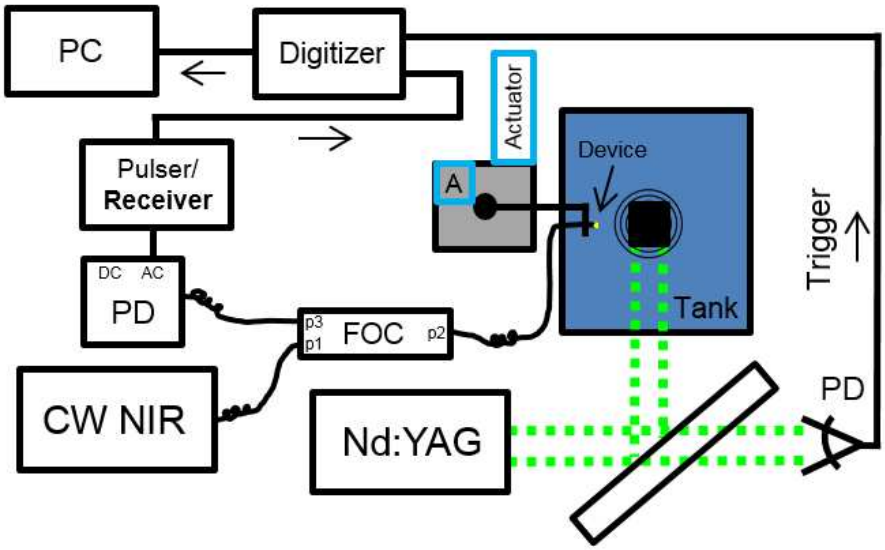

Figure 4.6. Optical and DAQ system for synthetic aperture imaging of a photoacoustic target using fiber etalon.

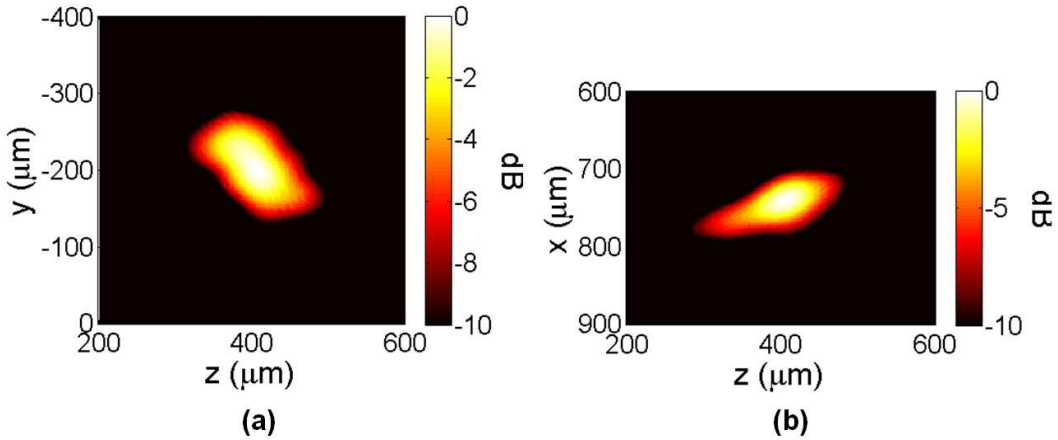

A more complex target was chosen to determine the sensor's ability to resolve an asymmetric geometry. A human black hair of 60 µm diameter was embedded into a gel. The etalon was scanned above the target over a 1.5 x 1.5 mm plane at 50 µm increments (equivalent to 961 hypothetic sensors). All other scanning and processing parameters were the same as in the bead scan. The reconstruction results are found in Figure 4.8. This illustrates the hypothetical array's ability to image more complex 3-D objects such as a heterogeneously-oriented group of blood vessels.

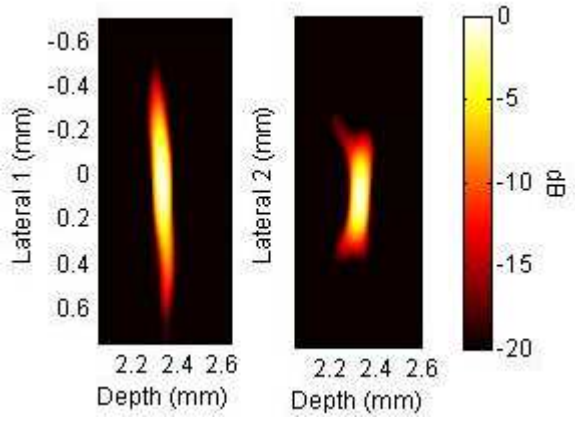

Figure 4.8. Orthogonal 2-D reconstructions of a 60 µm hair.

4.4 Discussion

We have constructed an etalon with an Au/SU-8/Au thin-film structure on a SM fiber with 9 µm core. The SU-8 layer was deposited via spray-coating which resulted in an undesirable dome-like profile over the fiber. The resonance profile indicated a 13 µm thickness and finesse of 22. The sensitivity of the device was measured to be 11.6 kPa over a 47.5 MHz bandwidth, or 1.7 $Pa/Hz^{1/2}$ with a -3 dB bandwidth of 27 MHz centered at 28 MHz. We have also demonstrated the ability of a fiber etalon bundle to perform 3-D PAI by spatially scanning the device in a 2-D plane.

If more sensors are to be introduced to form a bundle, the etalon fabrication process must undergo some revision so as be more reproducible; when spray coating of the polymer layer is performed manually, device thickness is difficult to precisely control. This could lead to a variation in resonance wavelength, bandwidth, and sensitivity across fibers. A Parylene Deposition System (PDS) would facilitate a reproducible, sufficiently

thin, and uniform polymer coating across the face of the fiber bundle.

Design and assembly of an optical system to process multi-fiber signals will be carried out after fabrication of the bundled device. Two designs are being considered, both of which have a different method of coupling the laser to the fiber bundle. The first design entails the use of a fiber optic optical switch (OS) as shown in Figure 4.9. Magneto-optical switches with microsecond switch times are commercially available (e.g. Agiltron's Crystalatch), however they are limited to a low number of fibers (1x8). Multiple 1x8 multiplexers could be cascaded to create a switch of a larger order, though a bundle of over 100 fibers would require over twelve 1x8 switches. Switches up to 1x128 are also available but the switching time is increased to the order of milliseconds due to a micro-electro-mechanical systems (MEMS)-based mechanism (e.g. DiCon 1xN OS). At present these devices are quite costly and therefore may not be a suitable choice. A less expensive method would be to focus the beam in free space onto the core of each fiber in a sequential manner using linear actuators. Translation from one position to the next will also likely be on the order of milliseconds. While this arrangement might be more compact than when using an OS (a 100 fibers would require a 100 fiber optic connections), the scanning procedure will require more precision for beam alignment. More of this method will be detailed in Chapter 5. Ultimately, the acquisition of signals from every fiber in a timely manner is required in order to achieve an acceptable frame rate.

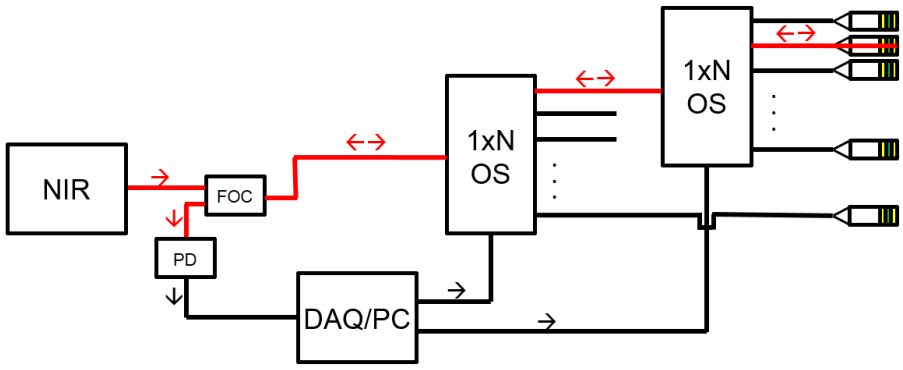

Figure 4.9. Fiber optic system for fiber etalon array. Multiple 1xN optical switches (OS) can be cascaded to form a bundle of elements.

The diameter, optical properties, and total number of individual fibers chosen to be bundled will be directly related to the device's size, resolution, and frame rate. If beam scanning is chosen over optical multiplexing, the larger core size of multi-mode (MM) fibers would better facilitate the coupling of the beam. An additional requirement is that the fibers chosen should have a low Numerical Aperture (NA) for strong optical resonance at the receiving end. 100 µm MM fibers of 0.12 NA are currently available. A 100-element rectangular bundle of these fibers, for example, would yield a 0.5 mm x 0.5 mm device. Because arterioles are typically around 30 µm in diameter, presently achieved resolutions will need to be improved upon in order to perform imaging of microvasculature, particularly when fewer fibers are chosen than simulated here. In order to acquire a reasonable frame rate, the PRF of the laser will need to be increased, and the number of signal averages will need to be lowered. Reconstruction time for a 1 mm x 3 mm field-of-view was approximately 2.5 seconds. For a 100 element array using a PRF of 5 kHz and 64 averages, the total time for acquisition and reconstruction of a single frame would then be 3.8 seconds.

Regarding clinical applications, our design for PAE could be implemented as a form of high resolution image guidance during procedures involving percutaneous biopsy. Because the dimensions of our device will be dependent on the fiber bundle diameter, its size could be scaled down so as to be mountable at the tip of a biopsy needle in order to provide awareness of the vascular environment directly ahead. Endoscopic Ultrasound Fine Needle Aspiration (EUS-FNA) is already an established imaging modality for forward-viewing endoscopic biopsy guidance. However, commercially available models consist of low-frequency curvilinear ultrasound arrays (<10MHz) (Pentax EB-1970UK, Olympus GF-UC140P-AL5) which limits resolution to over 100 µm. The 30 µm resolution as provided by our device design would allow for higher quality imaging during procedures. It could also serve as a means to characterize tissue which could reduce the need to perform biopsy.

Chapter 5

Towards a Fiber Optic PI-etalon Imager

5.1 Overview

We have previously shown the viability of a PI-etalon thin film structure to serve as a high-frequency transmit/receive ultrasound transducer. In order for all-optical ultrasound transduction to have a future in clinical ultrasound imaging, transitioning from free space operation to fiber optics is essential. Here we present preliminary work and the design concept for a fiber optic imager based on the PI-etalon transducer. The creation of a single-element device is first explored using a 50 µm broadband optical fiber. Deposition of a 1-5 µm layer of PI onto the fiber was achieved via spray-coating with an airbrush, and a 0.5 µJ 355 nm pulse was coupled to the fiber resulting in a 150 kPa signal. While coupling NIR light to the fiber is easily accomplished in free space, capturing the reflected signal is very challenging and necessitates considerable attention to the supporting optics. Here we propose modifications to the optics presented in Chapter 4 to meet such needs. Finally, we speculate on the requirements for expanding the single-element design into an array suitable for imaging with a synthetic aperture.

5.2 Introduction

In vivo medical applications such as endoscopic and intravascular ultrasound typically require high frequency operation in order to obtain a resolution that provides clinically meaningful information. These applications also require compactness and flexibility for easy insertion and maneuverability. Meeting these requirements has proven to be a significant challenge using conventional ultrasound technology because the electrical cabling and interconnections involved at this scale make ultrasound arrays particularly susceptible to RF noise, capacitive loading by the leads, and distortion from crosstalk. As a result, additional front-end electronics are usually required which adds undesired bulk to the imaging head thereby limiting the ability to meet size requirements.

The ultimate goal in the pursuit of all-optical ultrasound transduction is the production of a fiber optic device for *in vivo* applications. Electrical cabling and interconnections would be nonexistent at the scan head using these elements, thereby circumventing electrical noise and distortion. Furthermore, the prospect of using optical fibers as the sole means of communication with the imaging head raises the likelihood of meeting the size and flexibility requirements of endoscopic and intravascular devices. While there have been instances of fiber optic ultrasound receivers (including that presented in Chapter 4) [69]-[72] and fiber optic ultrasound transmitters [73]-[76], to date there has been no production of an integrated transmit/receive transducer in fiber optic form. PI-etalons are an ideal candidate for such a device because the optical properties of the thin film layers allow receiver and transmitter to exist in the same location. Here we present progress made towards fabrication of a single-element fiber optic PI-etalon and present a design concept for expansion into a fiber bundle for synthetic aperture imaging.

5.3 Methods and Results

5.3.1 Fiber Selection and Characterization

The first challenge encountered when fabricating a fiber optic PI-etalon is the availability of an appropriate fiber. The chosen fiber must be:

1. An efficient transmitter in both the UV and NIR spectrums;
2. Resistant to thermal damage induced by high energy UV pulses;
3. Heat resistant to temperatures at which polyimide layers are cured (250-300 ℃);
4. Available in a bundled package; and
5. Available with core sizes less than 100 µm.

The ideal choice would be a fused, coherent array of small-core fibers (~ 10 µm) to form an image bundle (Figure 5.1). Laser scanning across the rear bundle face would then be exactly reproduced at the front end where the device is deposited. Moreover, precise lateral alignment of the UV or NIR beams with an individual fiber's location for efficient coupling is unnecessary with fused cores. At present, commercially available image bundles do not meet requirements 1-3. We are therefore resigned to choosing a

specialty fiber with which bundles can be custom-made. Coherent bundles of this type containing a large number of fibers are extremely costly and are thus not an option, however one can theoretically map the position of fibers in incoherent bundles from end to end. In this case, the coordinates recorded must be taken into consideration during beam scanning. Special care to align the optical beams with fiber cores is also challenging because cores are separated by the cladding of the fibers chosen (i.e. not fused).

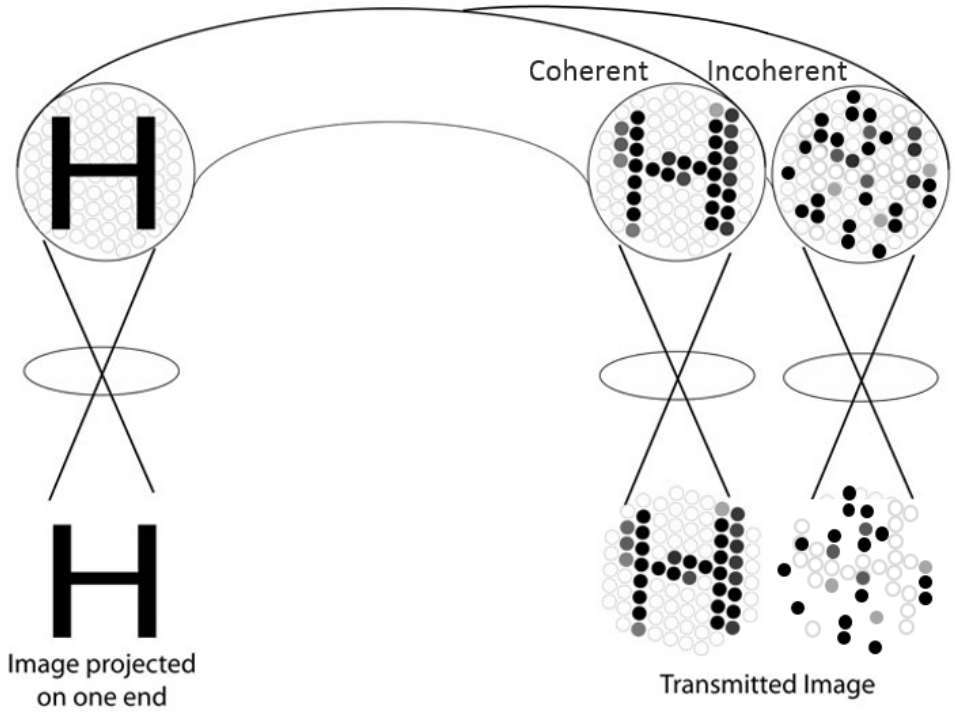

Figure 5.1. Image transmission through an image bundle (coherent) and a non-coherent bundle [77].

We have verified the functionality of a suitable broadband, MM fiber with 50 µm core diameter (Optran WF, Ceramoptec). It's transmission at both 355 nm and 1550 nm is above 99% (Figure 5.2), and it is available with small cladding (60 µm diameter) for dense bundling. A 5-ns 355 nm optical pulse with energy over 1 uJ (DTL-375QT, Laser-export) was successfully coupled to the fiber for greater than 30 minutes without signs of thermal damage. Heat resistance is achieved using a polyimide jacket in the case of bare fiber or stainless steel SMA 905 connectors when bundled. In Figure 5.3a is a photograph of a 7-element non-coherent bundle provided by Ceramoptec using the WF

fibers. The epoxy used to adhere the 7-element bundle to the connector that contains it can raise the level of the bundle such that it is no longer flush with the connector surface (also known as “pistoning”). The quality of thin films to be deposited on the fibers’ end face will depend on this topology (Figure 5.3b), therefore it needs to be taken into account when choosing an appropriate deposition method.

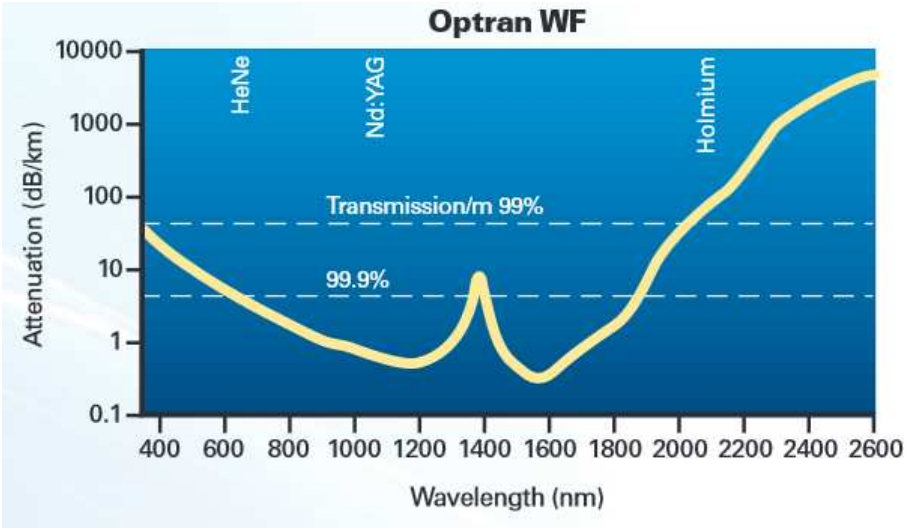

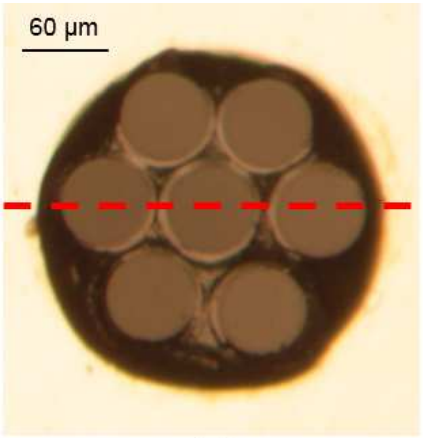

(a)

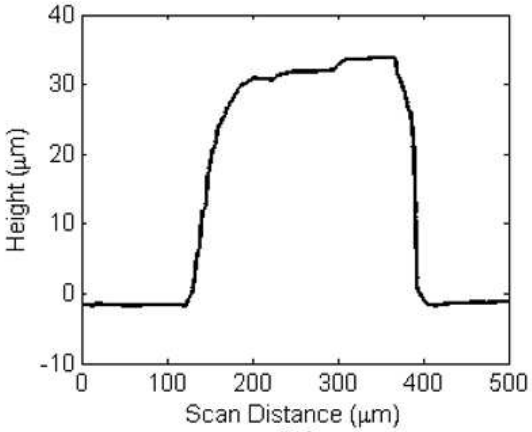

(b)

5.3.2 Fabrication

5.3.2.1 Introduction

Again consider the general thin film structure to be fabricated on the end face of optical fibers (Figure 5.4). In Chapter 4 we demonstrated the effect that not having a conformal coating can have on the receiving properties of the etalon transducer. The curved/domed layer provided by spray-coating SU-8 distorted the waveform to be detected through undesirable acoustic modes. Thus, it is critical that conformal layers are produced whenever possible. Parylene has been shown to be a well-suited material for the etalon polymer because vapor deposition systems dedicated to it are commercially available. Parylene can also serve as the protective polymer. Deposition techniques already utilized for fabrication of the etalon mirrors are adequately conformal. The primary challenge then is the deposition of PI onto an irregular surface such as a fiber.

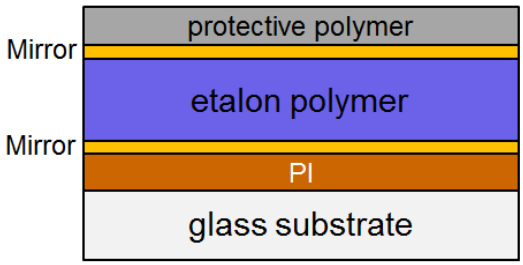

5.3.2.2 PI Deposition onto Optical Fibers

There is currently no commercial service available that can perform vapor deposition of PI, though layers on the order of 100 nm have been vapor deposited in a research setting using chemical vapor deposition [79]-[81]. As with SU-8 Microspray, there exists products for spray coating polyimides (e.g. POSS ImiClear, Hybrid Plastics), however these are restricted to clear PIs which do not have the prerequisite UV-absorptive properties. Tran proposed the spray deposition of polyimides using an airbrush technique [82], [83]. Spray coating of polymers via airbrush has been explored within the last five years as an option for low-cost production of organic solar cells [84], [85] and

has been shown to produce film qualities comparable to those of spin coating [86], [87]. Here we have modified this technique for deposition of 1+ μm films of PI-2555. While the non-conformity of spray coating will be present – particularly given the non-flat topology of a bundle as found in Figure 5.3b – limiting the PI thickness to a few microns will allow for a flatter device than the fiber etalon shown in Figure 4.1.

PI-2555 was diluted with T-9039 Thinner (HD Microsystems) and spray coated onto a bare Optran WF fiber with a gravity-feed single-action airbrush (200-9F, Badger Airbrush Co.). Gravity-feed was chosen for the finest atomization of spray particles, and single-action was chosen so as to have a flow rate that is independent of the spray trigger (Figure 5.5). Nitrogen gas from a standard gas cylinder was used as the air source. A 40% solution of PI-2555 provided the best film quality. Dilutions below 30% resulted in clumping of the polymer after the solvent is evaporated during a cure, and a 50% dilution did not sufficiently flow through the airbrush. Flow is also impeded if the airbrush is not flushed with solvent (T-9039) after every spray deposition, resulting in inconsistent layer thicknesses for particular spray conditions.

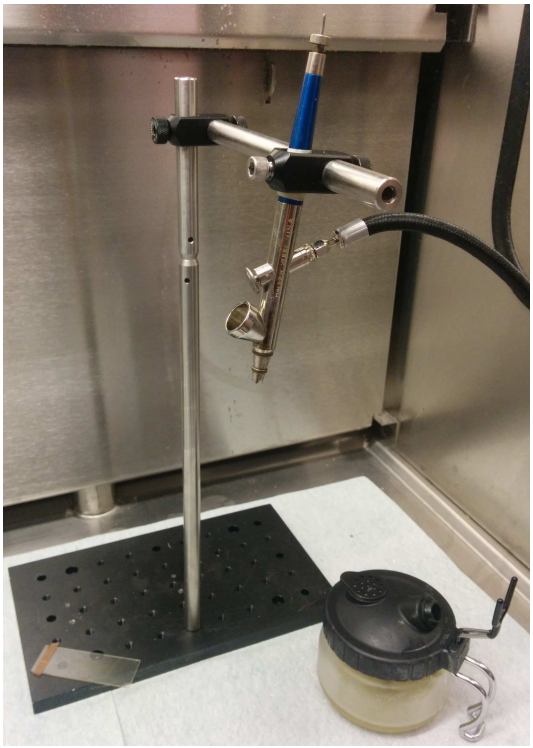

The critical parameter that controls the film quality when using an airbrush is droplet size. A higher droplet size has been shown to yield lower surface roughness but reduces film conformity, thus a tradeoff exists. The three dominant factors which influence droplet size are (1) gas/air pressure, (2) distance between the sample and the airbrush nozzle, and (3) flow rate [88], [89]. A larger droplet size is achieved using a high flow rate, low pressure, and low spray distance. However, a low gas pressure in the range of 15-20 psi with a 15-20 cm spray distance is recommended in order to prevent the airbrush from blowing off droplets that have already landed on the sample surface. A low flow rate is ideal for our application, as conformity to the fiber geometry is desired at this time. Because flow rate is controlled via a turning screw on the back of the airbrush, quantitative estimation for the parameter is not possible. However, flow rates are reproducible by tracking the number of turns on the adjustment screw.

With the cleaved fiber face under the airbrush, the fiber was motioned in a figure-8 pattern under continuous spray for 20 seconds. The pressure was approximately 23 psi with a nozzle-to-sample distance of 20 cm. The fiber was then cured at 125 ℃ for 1 minute to evaporate the solvent followed by a 90-minute cure at 250 ℃ in a vacuum oven. Figure 5.6a shows photographs of the fiber before and after deposition. A slightly curved surface is evident as with SU-8 Microspray in Figure 4.1. The most practical manner with which to estimate the film thickness at this time is to reference it to the diameter of the fiber coating – 70 µm. The film thickness is most likely in the range of 1-5 µm. Because the individual elements of a bundle as in Figure 5.3 do not appear to be completely flush with each other (i.e. the circular edge of each fiber's face is still present), we can expect similar deposition rates and film conformity when transitioning to the bundled design. This remains unconfirmed at this time because profiling the bundle face for different spray parameters requires sacrificing numerous samples (i.e. cutting off all but the connector to fit inside a profilometer), which are quite costly. Ultimately, vapor deposition of polyimide is preferred and possibly necessary, but constructing a deposition system to do so is beyond the scope of this project.

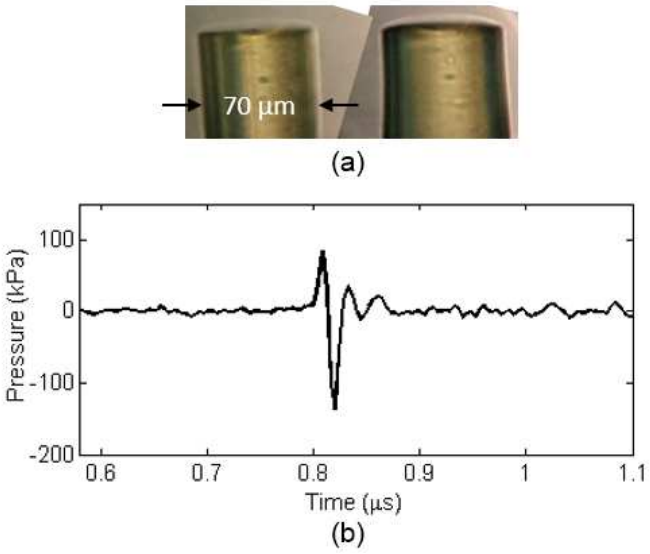

5.3.2.3 Fabrication of Etalon Layers

For the sake of convenience, gold mirrors have been chosen at this time to construct the etalon layers of the fiber optic device. In addition, a 10-15 µm layer of PI has been selected for the etalon medium because the material is currently available in spray-on form; however, the reflectivity of the Au mirrors prevents the layer's usefulness as an additional UV-absorbing medium. In the future, vapor-deposited Parylene will serve as the etalon layer due to its conformal properties. Finally, a dielectric mirror will replace the first gold mirror for higher finesse and enhanced acoustic sensitivity.

5.3.3 Supporting Optics

5.3.3.1 Optical Circulation

When evaluating the receive properties of a fiber-based PI-etalon, the first task is to construct the supporting optics for measuring the reflected NIR intensity. When using a fiber etalon receiver as reported in Chapter 4, the inclusion of the FOC was not only convenient but necessary. This is because an ordinary free-space circulator is polarization-dependent, and the SM fibers on which the etalon was deposited are not

polarization-maintaining. Significant energy loss can then occur, which is heavily influenced by the physical orientation of the fiber. FOCs are designed to be polarization-independent, which is required to support a fiber optic PI-etalon.

Direct connection of an FOC with a fiber PI-etalon is precluded by the need to couple more than one laser source to the same fiber and the need to spatially scan these lasers for imaging. The NIR and UV beams must therefore be coupled to the device fiber using free space optics. Figure 5.7 illustrates the ideal system for a PI-etalon fiber optic imager. NIR from the output port of a MM FOC is collimated and focused onto the bundle using 1-to-1 optical imaging. The two lenses are also mounted on a translation stage which allows scanning of the NIR beam. A stationary dichroic mirror is again placed between the two lenses thereby allowing integration of the UV source which is spatially scanned using a high-speed galvanometer.

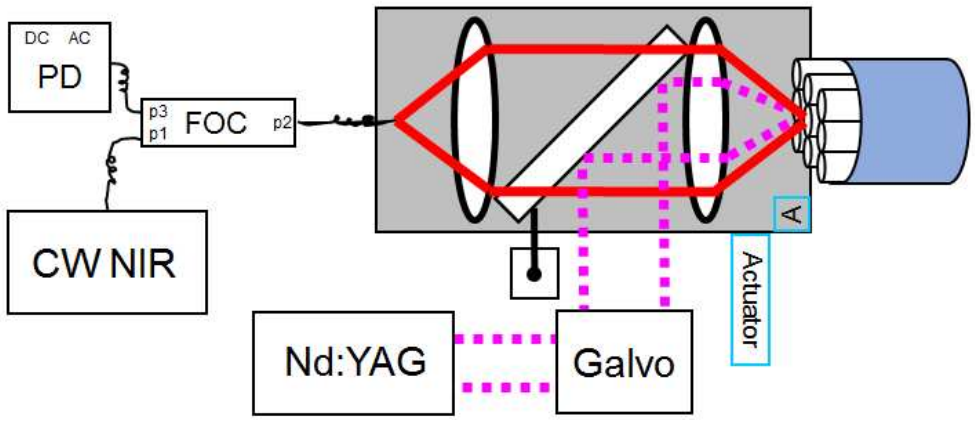

Figure 5.7. Ideal optical system for a fiber optic-based PI-etalon imager. The gray slab represents a translation stage.

The optical system for a PI-etalon imager as shown in Figure 5.7 is theoretically feasible but may be difficult to achieve in practice. This is primarily due to the challenge of coupling the reflected NIR source back into the FOC, which has an aperture determined by the core size of the fiber (< 100 µm). Even if alignment is perfected when focusing onto a certain fiber in a fiber bundle, translating the NIR beam to a different fiber will likely compromise this alignment. Repeated tuning might then be necessary, which would degrade the potential for real-time imaging. Using free-space optics for circulation is thus necessary.

As a free-space, polarization-independent alternative to a FOC, a simple non-polarizing 50-50 beam splitter (BS) for NIR circulation has been chosen (Figure 5.8). In using the BS, the reflected NIR energy arriving at the PD would be reduced to 25% of the input energy resulting in a 75% decrease in SNR. For comparison, the energy through a 50 µm MM FOC (C-band; Bitline System Pty. Ltd.) reflected off of a 50 µm MM fiber with 50 nm Au mirror was measured to be 55% of incident. The extra 30% loss in energy suffered when using a simple BS could easily be compensated for by selecting an NIR source with higher output power. An alternative to using a simple BS would be to construct the free-space equivalent of a FOC as done by Shiina et al. [91], but the number of components involved (two PBSs, two Faraday rotators, two half-wave plates) would add unnecessary complexity and pose additional alignment challenges.

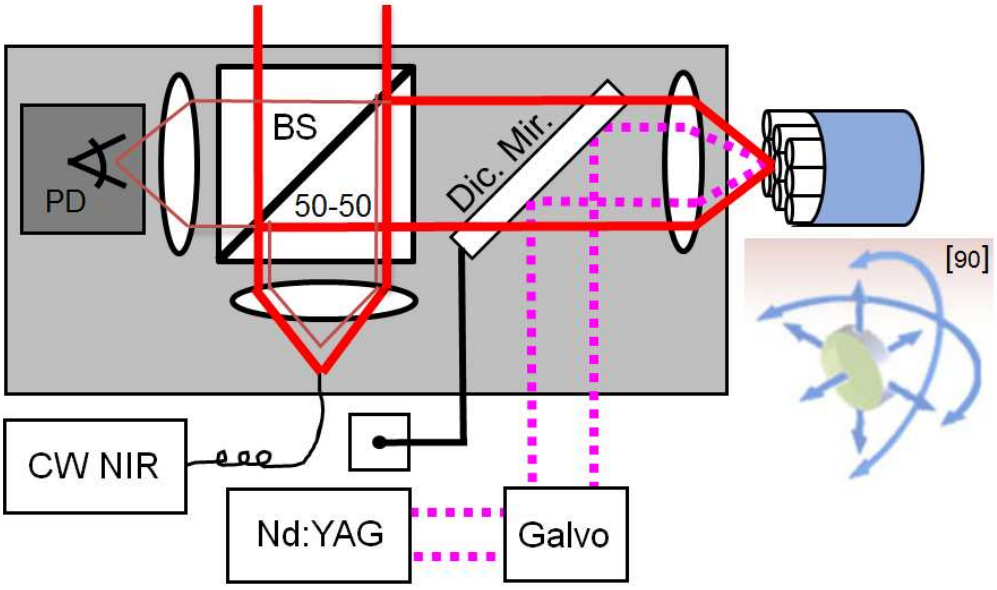

5.3.3.2. Selection of Focusing Lens

Care must be taken also in choosing the appropriate lens that is to focus both the UV and NIR beams onto the fiber so as to maximize coupling. The lens chosen should provide a spot size equal to or less than the core size of the fiber. Spot size is directly proportional to the focal length of the lens and is estimated to be

$$d = 1.27\lambda\frac{f}{D} ,$$

where d is the spot diameter, f is the lens focal length, and D is the beam waist at the lens. Another requirement of the lens is that its NA should be less than that of the fiber for efficient coupling. In air, NA is estimated to be

$$NA \approx \frac{D}{2f} .$$

A tradeoff therefore exists when choosing the focal length of the lens. In our experimental setup, the fiber chosen has a 50 µm core and NA = 0.22. Currently the beam waist for NIR is 3.6 mm (specified by fiber collimator) and approximately 0.5 mm for UV. The focal length of the lens should then be 10-55 mm to maintain a spot size below 50 µm and an NA below 0.22 for both NIR and UV beams.

5.3.4 Device Characterization

5.3.4.1 Acoustic Transmission

A 5-ns, 1.2 µJ 355 nm optical pulse (DTL-375QT, Laser-export) was coupled to the PI-coated Optran WF fiber with approximately 50 % efficiency. The average waveform generated over 1024 acquisitions as detected by a high frequency hydrophone (aperture: 85 µm, HGL-0085/AH-2010, Onda Corp.) is shown in Figure 5.6b. Its amplitude is approximately 150 kPa at a depth of 1.2 mm and was stable for greater than 10 minutes of continuous UV exposure.

5.3.4.2 Acoustic Reception

Current efforts are directed towards obtaining a resonance curve of a single PI/Au/PI/Au fiber optic device and determining receive characteristics. The optical system illustrated

in Figure 5.8 sans galvo has been constructed for this purpose. Unfortunately, we cannot meet the NIR energy requirements at this time given the large losses incurred by the 50-50 BS and imperfect fiber coupling. The current NIR source (HP 8168F, Agilent Technologies) has a maximum output of 5 mW, therefore a new laser with approximately 20 mW output energy is preferred although at substantial cost. Cost may be reduced by selecting an NIR diode laser with fixed wavelength or narrow range if the resonance wavelength is predictable through strict control of the fabrication method.

5.4 Discussion

In this chapter we have laid the foundation for building an endoscopic imager utilizing a PI-etalon for all-optical ultrasound transduction. A suitable fiber on which a PI-etalon is to be deposited has been identified and tested, and a spray coating technique has been created to coat optical fibers with a PI thin film. Vapor deposition of the etalon medium is required for a conformal coating in order to prevent distortion of received acoustic waves. In addition, an optical system has been designed to support the coupling of NIR and UV beams to a bundle of optical fibers, however a large portion of NIR energy must be sacrificed. This necessitates investment into a more powerful tunable NIR laser for future studies.

Chapter 6

Summary and Future Directions

6.1 Summary

A novel form of all-optical ultrasound technology has been presented in this thesis for high frequency operation and high resolution imaging. All-optical operation evades the electrical noise, distortion, and crosstalk of piezoelectric probes, and dense 2-D arrays of high frequency elements are easily produced by the focusing and scanning of laser beams. The choice of a PI film as a photoabsorptive layer to be integrated into an etalon receiver allows (1) the thermal stability required for sustained operation and (2) transmission and reception of ultrasound at any location on the device surface. Imaging with high dynamic range is therefore possible using dense synthetic arrays of arbitrary configuration. We envision the development of a compact imager based on the PI-etalon that would provide roughly a 1.5 x 1.5 x 8 mm field of view for endoscopic applications such as IVUS and biopsy-guidance.

Chapter 2 presented the optical and acoustic characterization of the PI-etalon. PI-2555/2525 films exhibit a penetration depth of 0.8 µm at 355 nm and greater than 95% transmission at 1550 nm. By depositing PI films underneath the etalon device layers, thermal stability of the transducer is achieved, as the film absorbs the majority of UV energy before incidence onto the etalon structure. In addition, two PI-etalon designs were compared – one having simple gold mirrors with SU-8 as the etalon medium (Au/Au) and the other having a dielectric inner mirror combined with PI as the etalon medium (Die/Au) for gains in acoustic sensitivity and emission amplitude, respectively. Both designs exhibited superior bandwidth as well as a sensitivity and emission strength comparable to piezoelectric and CMUT transducers of similar active area. We will proceed with the Die/Au design, which approximately exhibited an NEP of 0.5 $Pa/Hz^{1/2}$ and a central operating frequency of 50 MHz with a bandwidth of 125%.

In Chapter 3 we evaluated the imaging capabilities of the PI-etalon using synthetic arrays formed via beam scanning. Two methods were presented: (1) a fixed-transmitter/scanning-receiver arrangement using broad UV illumination for plane wave imaging and (2) a fixed-receiver/scanning-transmitter configuration with transmit and receive elements similar in active area. A broad UV spot easily produces pressure over 1 MPa, but scanning the receive element entails determination and monitoring of the resonance wavelength at each location. While scanning a smaller transmitting element produces much lower pressures, the method facilitates faster scanning and a more stable receive sensitivity. Additionally, rapid averaging and sensitivity improvements by various means will compensate for the reduction in SNR. Using both configurations in a 2 x 2 mm aperture, we were able to achieve an axial resolution of 35-40 µm and a lateral resolution between 50-150 µm within a depth of 6 mm.

Transitioning from a free-space to a fiber optic design is critical for delivering all-optical ultrasound technology to clinical scenarios. Chapter 4 reported the development and characterization of a fiber optic etalon receiver with layers Au/SU-8/Au deposited on a 120 µm SM fiber. The receiver demonstrated an NEP of 1.7 $Pa/Hz^{1/2}$ with a bandwidth of 100% centered at 27 MHz. Spray coating of SU-8 was utilized to form a 10-15 µm etalon layer over the core, but the surface tension of the fiber facilitated a dome-like/convex cavity covering the entire fiber face. This produced undesirable acoustic modes that distorts detection of the incident acoustic waveform. Finally, PAI of simple targets was performed using 2-D translation of the fiber to simulate a bundle of fiber etalons.

Building upon progress made in Chapter 4, work towards full transmit/receive optical ultrasound in fiber optic form was detailed in Chapter 5. A spray method using an airbrush for PI-2555 was developed, and a 1-5 µm layer was deposited on a carefully selected wide field fiber. Coupling of UV to the fiber produced pressure waveforms with an amplitude comparable to that achieved in Chapter 2 with a wafer-based device. Furthermore, we have described a suitable optical system for the receive component of the imager, but obtaining an NIR laser source with higher energies is likely required to proceed with further developments. Vapor-deposition of thin, conformal PI layers is ultimately desired for creation of a fiber bundle of PI-etalons but is presently unavailable.

6.2 Future Directions

6.2.1 Near-term Goals

At this juncture we seek to verify the functionality of a single, fiber optic PI-etalon element. For convenience, the layered structure will be PI/Au/PI/Au with spray-deposited PI layers. Precise alignment of the fiber using the 5-axis kinematic mount as indicated in Figure 5.8 is crucial in order to maximize the reflected power. Once alignment is optimized, we anticipate a reduced sensitivity compared to wafer-based devices until an NIR source with higher output power is obtained. Moreover, the pulse-echo frequency spectrum may be distorted by using a non-flat etalon layer. Despite these deficiencies, we will subsequently transition to bundles of fibers using the same device layers and evaluate the efficacy of laser scanning from element-to-element. Once proof of concept is established, a foundation for all-optical ultrasound imaging *in vivo* will have been created. Improvements in device fabrication, the supporting optics, and instrumentation will then be integrated in order to advance the technology towards clinical viability.

6.2.2 Lateral Beam Confinement

In Table 2.1, we compared performance parameters between the PI-etalon and other technologies with elements of similar active area. The bandwidth and center frequency of the PI-etalon has been shown to be superior to CMUTs and piezoelectrics, and both receive sensitivity and levels of pressure generated were within the same order of magnitude. Despite this achievement, all-optical ultrasound technology will likely not be adopted due to the cost and size of the accompanying system unless an order-of-magnitude increase or more in SNR is acquired. Also discussed in Chapter 2 were various methods for improving both transmission and reception, however the changes required to drastically improve SNR are likely to come from lateral beam confinement in the etalon resonator cavity. As illustrated in Figure 6.1a, optical reflections in a flat cavity will disperse laterally. This broadens the resonance profile in two ways. Firstly, successive non-normal reflections will be associated with a different optical path length – a phenomenon referred to as phase dispersion. Reflection at the primary resonance wavelength will then be increasingly non-zero, resulting in a shallower and hence

broader resonance profile. Secondly, lateral beam propagation results in energy loss to the interferometer, which can be considered an effective reduction in mirror reflectivity. Because optical finesse is inversely proportional to mirror reflectivity, finesse is lowered.

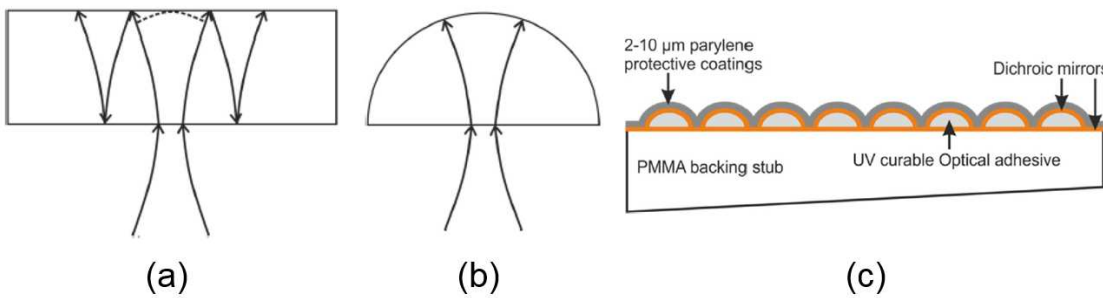

Figure 6.1. Illustration of laser light propagation into a **(a)** flat and **(b)** concave etalon cavity. The lateral spread of energy in the flat cavity creates phase dispersion and an effective reduction in reflectivity. A concave outer mirror of specified curvature can retain such reflections thereby preserving optical finesse. Arrays of concave etalon cavities **(c)** have been fabricated using inkjet printing of UV-curable adhesive [92] (© 2014 SPIE).

Zhang and Beard first modified the shape of the etalon cavity into a convex surface [47]. The first mirror is flat, and the second takes the shape of the convex cavity (Figure 6.1b). By carefully designing the curvature of the cavity, the curved mirror can more efficiently reflect light emerging at non-normal incidence back into the core and help maintain a consistent optical path length. This reduces energy loss and phase dispersion resulting in higher finesse. Li et al. have succeeded in creating arrays of these structures using inkjet printing of UV-curable adhesive (Figure 6.1c). In comparison to a flat etalon cavity with thickness equal to the radius of the convex cavity (56 µm), finesse improved from 60 to 218. The NEP was measured to be 85 Pa over a bandwidth of 20 MHz, or 20 $mPa/Hz^{1/2}$ – an order of magnitude smaller than that achieved using the PI-etalon though over a much lower bandwidth [92]. These benefits were not apparent in our fiber optic etalon with domed shape because the film curvature was not custom tailored to the NA of the fiber.

A second method for lateral confinement of the etalon probe beam is to create a step-index configuration as inside an optical fiber. This has been achieved by Tadayon et al. with a fabrication procedure shown in Figure 6.2 [48]. Cylindrical pillars of SU-8 2010 polymer (refractive index: 1.67) are created using photolithography, and a cladding made of a thiol-ene/methacrylate photopolymer (TM Polymer) with 1.53 refractive index

is deposited around the pillars. This was accomplished by placing a glass slide on top of the pillar and placing droplets around the pillar with a syringe (i.e. via capillary action). The total internal reflection created in a typical 1.62/1.52 optical fiber is then mimicked resulting in lateral energy confinement and thus preservation of high optical finesse. When using a core/pillar that is 20 µm in diameter with a thickness of 25 µm, the finesse was found to be 200 whereas the finesse measured when focusing outside of the core material was approximately 40. The NEP was measured to be 178 Pa over a bandwidth of 28 MHz, or 30 mPa/Hz$^{1/2}$ – again, an order of magnitude below that of a plain polymer etalon. This step-index configuration will likely be chosen over a convex cavity because the acoustic response of a flat film is more ideal than that of a hemispherical surface.

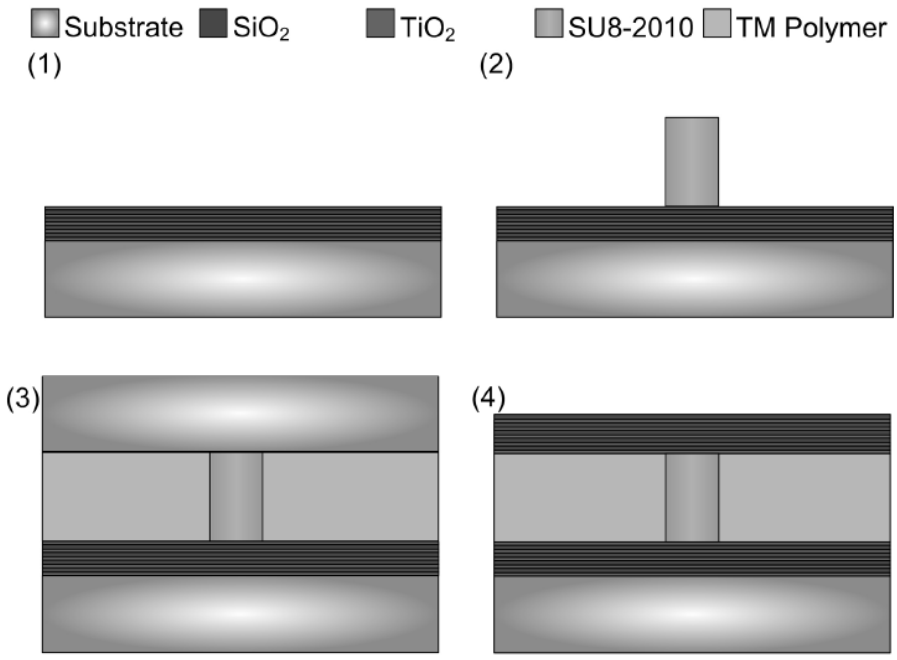

Figure 6.2. Fabrication process for a polymer waveguide etalon. In **(1)** a dielectric mirror consisting of alternating layers of SiO_2 and TiO_2 is deposited onto a glass substrate. **(2)** Cylindrical pillars of SU-8 are then produced to serve as the core material. **(3)** A polymer cladding is created by placing a glass slide on top of the pillar and filling in the gap. **(4)** The glass slide is removed, and the second mirror is then deposited [48] (© 2014 IEEE).

Another factor that could severely influence optical finesse is the necessary use of MM optical fibers as a basis for a fiber optic PI-etalon imager. In order to couple both UV and NIR energy into the same fiber, a special wide-field MM fiber with 50 µm core and 0.22 NA was selected. We have demonstrated the operation of a fiber-etalon using a SM fiber with 9 µm core and 0.12 NA. Because using a fiber of higher NA increases the range of

propagation angles out of the fiber, there will be an increase in phase dispersion and energy loss when choosing a MM fiber. A lowered optical finesse is therefore expected. Using lateral beam confinement as with a convex or waveguide etalon may not only be useful but necessary in limiting phase dispersion in this case. However, successful ultrasound detection using MM fiber etalons have already been demonstrated without such modifications [70], [93]. For an in-depth analysis of how illumination by MM fiber influences etalon performance, see [94].

6.2.3 Alternatives to Synthetic Apertures

The limitations of synthetic apertures is also a concern in pursuing all-optical ultrasound imaging. In Chapter 3 we discussed modifications to the fixed-receiver/scanning-transmitter configuration that would reduce the acquisition of a single frame to below 1 second. The inclusion of a galvo-scanner and four NIR sources were cited as the options conducive to this reduction. Figure 6.3 illustrates an optical system that could incorporate both features. Multiple NIR beams are fed to the 50-50 BS and focused using the same lens, and their respective reflections are focused onto their dedicated PD. In order to separate positional control over the NIR beam positions, tilting of each NIR source's fiber collimator will be necessary. A disadvantage of transitioning to this system is the added cost associated with additional lasers and PDs. Alignment of all NIR beams onto their respective fibers and PDs might also prove to be highly challenging. Finally, whether or not the frame rate can be increased to real-time levels (> 25 PFS) after incorporating the proposed features in Figure 6.3 is presently unknown, and motion of the target during UV laser-scanning may result in intractable image artifacts. Options that do not involve beam-scanning must therefore be investigated.

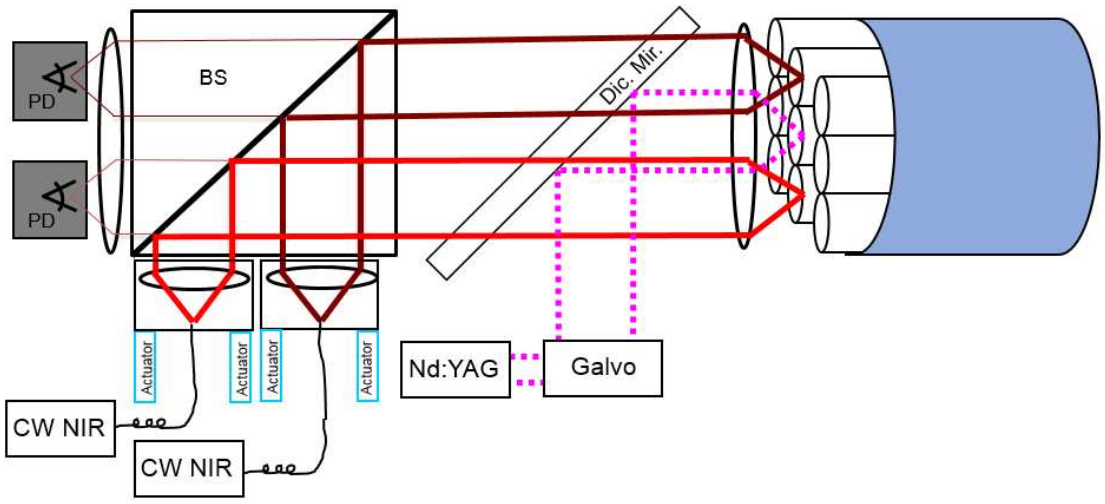

Figure 6.3. Proposed optical system for fixed-receiver/scanning-transmitter imaging. Four NIR beams are directed through the same optics, and their position after focusing onto the bundle is determined by their angle of incidence, which is controlled using tilting mounts.

Parallel etalon detection has been demonstrated using a broad illumination beam combined with a CCD camera as shown in Figure 6.4 [95]. The CCD sensor detects the intensity of the reflected beam at multiple locations simultaneously. Because the frame rate of modern CCD/CMOS image sensors is typically below 500 Hz, the CCD cannot alone detect MHz waveforms. Instead, the etalon probe beam is pulsed such that the CCD is effectively on only at the time at which one decides to sample. In order to sample at consecutive time points, the laser is pulsed with a series of time delays thereby allowing construction of the full waveform. However, to construct a full pressure waveform, one is limited by the CCD frame rate. For example, acquiring a 10 µs waveform at an effective sample rate of 100 MHz requires 1000 samples and hence 1000 frames. The total time required to construct the full waveform is then 2 seconds assuming 500 FPS. Because this corresponds to a lower frame rate than the proposed fixed-receiver/scanning-transmitter arrangement, this method is only advantageous when the alternative is the fixed-transmitter/scanning-receiver scan method in which much time is necessary to determine the optimal wavelength at each receive location. This method may be optimal if the high SNR gains when using a broad UV (transmitter) spot is critical.

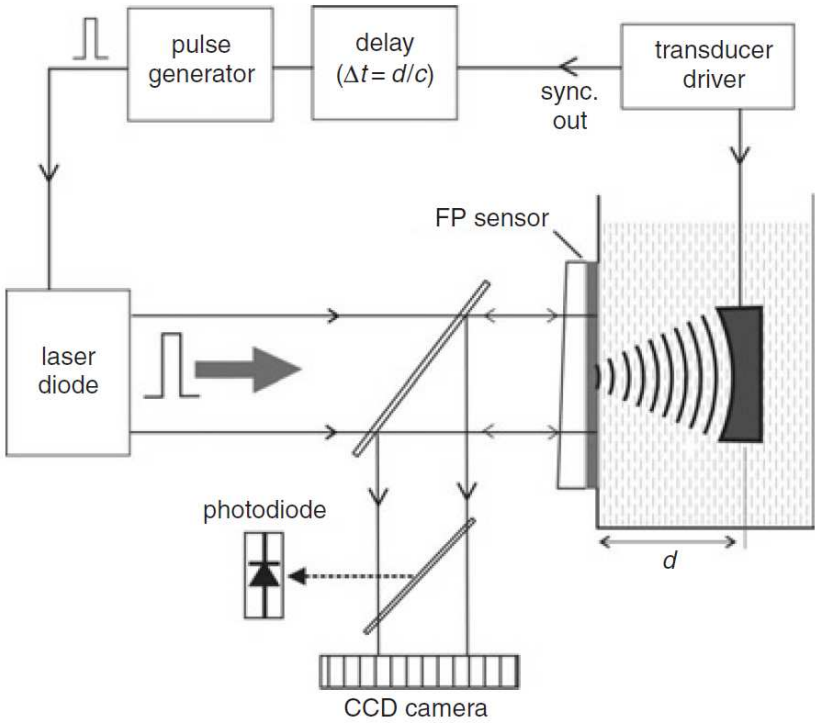

Figure 6.4. Multi-channel, parallel-acquisition detection of ultrasound with an etalon. Instead of a CW source, a pulsed source is triggered at the anticipated time-of-arrival of ultrasound so that the CCD is effectively on only at that time [95] (© 2006 IEEE).

An interesting method for producing a laser-generated ultrasound field of arbitrary shape with no need for beam scanning is to pass a broad beam through a holographic pattern (phase hologram) before incidence onto the photoabsorptive film [96]. Specifically, focused narrowband ultrasound can be created by passing light through a binary Fresnel zone plate (Figure 6.5a). The depth of focus depends on the ultrasound frequency and the size of the rings in the Fresnel pattern, and the lateral position of focus is controlled by the position of the pattern's central axis relative to the beam. Brown et al. have confirmed that broadband ultrasound can be focused as well if one uses a series of laser pulses with a temporal spacing proportional to the spacing of the arcs in the Fresnel pattern [97]. Finally, fast steering of the focal point can even be done by using a liquid-crystal spatial light modulator to alternate between different Fresnel patterns at video frame rates (> 50 FPS). It should be noted that the arrangement of the optical fibers to which the light is to be coupled would likely disrupt the pattern to a moderate degree before arriving at the PI film.

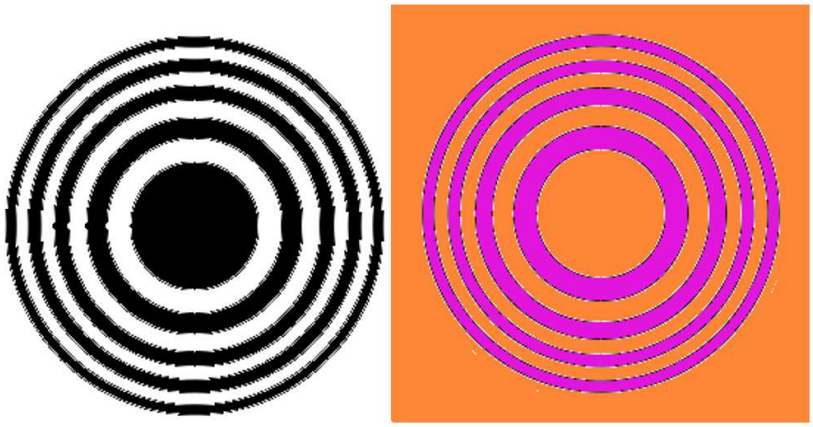

(a) (b)

Figure 6.5. Focusing of optically-generated ultrasound using **(a)** Fresnel zone plate as a holographic pattern through which a broad UV pulse is guided before hitting the PI film, resulting in the illumination pattern **(b)**.

A less involved alternative to free-space laser scanning is to work purely with fiber optics from the lasers to the device as suggested for a receive-only bundle in Figure 4.9. Figure 6.6 illustrates a completely fiber optic system wherein the UV and NIR sources are routed to a network of fiber PI-etalons via 2 x N bi-directional optical switches controlled by the user. As mentioned in Chapter 4, the switching time for conventional MEMS switchers is on the order of 10 ms, yet devices using an electric field as the sole switching mechanism (i.e. non-mechanical) can switch on the order of 10 ns. However, identifying a fast switch that operates over such a broad wavelength band (350-1600 nm) may be problematic and costly. A means to bundle the individual PI-etalon elements after they have been deposited would also be required.

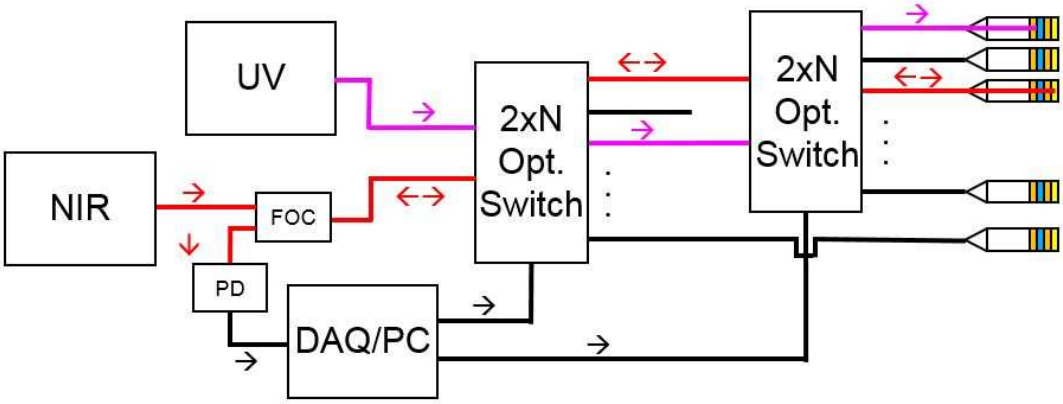

6.2.4 Dual-mode Pulse-echo/PAI

A logical progression from the work presented here is the integration of photoacoustic functionality into the PI-etalon for dual-mode imaging. By utilizing dielectric films for both etalon mirrors, the entire structure could be transparent at wavelengths used for photoacoustic excitation of tissue. It is conceivable then that dual-mode operation allowing both pulse-echo and PAI is possible, being of particular use in the context of IVUS; Sethuraman et al. revealed that photoacoustic intravascular probes have the potential to differentiate between vulnerable plaques [98]. In this case, the fixed-transmitter/scanning-receiver arrangement will be required to provide a sufficient number of receivers for high quality PAI, and the supporting optics must be modified to include an additional beam as shown in Figure 6.7. Switching to a lower wavelength for etalon operation may also be necessary to minimize the thickness of the dielectric mirrors. This would reduce acoustic reflections at the device-medium interface as well as preserve bandwidth in both transmission and reception of HFUS.

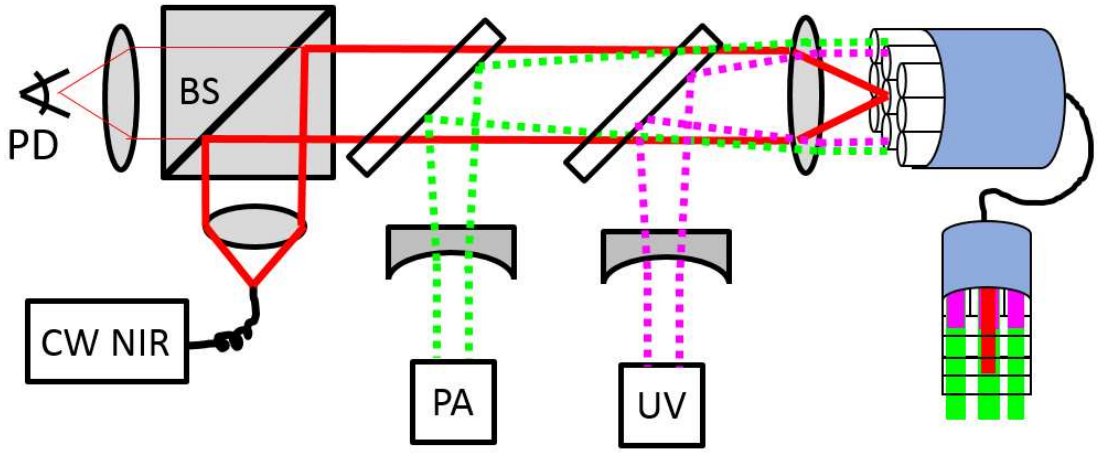

Figure 6.7. Potential optical system for dual-mode pulse-echo/PAI using a PI-etalon array (PA: photoacoustic source).

Bibliography

[1] D. F. van Wijk, A. C. Strang, R. Duivenvoorden, D. F. Enklaar, R. J. van der Geest, J. J. Kastelein, E. de Groot, S. G. Stroes, and A. J. Nederveen, “Increasing spatial resolution of 3T MRI scanning improves reproducibility of carotid arterial wall dimensions measurements,” *Magn. Reson. Mater. Phy.*, vol. 27, pp 219-226, 2014.

[2] Y. Zhao, E. Brun, P. Coan, Z. Huang, A. Sztrokay, P. C. Diemoz, S. Liebhardt, A. Mittone, S. Gasilov, J. Miao, and A. Bravin, “High-resolution, low-dose phase contrast X-ray tomography for 3D diagnosis of human breast cancers,” *Proc. Nat. Acad. Sci*, vol. 109, no. 45, pp. 18290-18294, 2012.

[3] J. T. Bushberg, J. A. Seibert, E. M. Leidholdt, and J. M. Boone, *The Essential Physics of Medical Imaging*, Philadelphia, PA: Lippincott Williams & Wilkins, 2012, pp. 15.

[4] F. S. Foster, C.J. Pavlin, K. A. Harasiewicz, D. A. Christopher, and D. H. Turnbull, “Advances in ultrasound biomicroscopy,” *Ultrasound Med. & Biol.*, vol. 26, no. 1, pp. 1-27, 2000.

[5] D. A. Knapik, B. Starkoski, C.J. Pavlin, and F.S. Foster, “A 100-200 MHz ultrasound biomicroscope,” *IEEE Trans. Ultrason. Ferrorelectr. Freq. Control*, vol. 47, no. 5, pp. 1540-1549, 2000.

[6] X. Li, W. Wu, Y. Chung, W. Y. Shih, W. Shih, Q. Zhou, K. K. Shung, “80-MHz intravascular ultrasound transducer using PMN-PT free-standing film, *IEEE Trans. Ultrason. Ferroelectr. Freq. Control*, vol. 58, no. 11, Nov. 2011.

[7] X. Li, W. Wei, Q. Zhou, K. K. Shung, and Z. Chen, “Intravascular photoacoustic imaging at 35 and 80 MHz,” *J. Biomed. Optics*, vol. 17, no. 10, pp. 106005-1, 2012.

[8] C. K. Lee and P. J. Benkeser, “Investigation of a forward-looking IVUS imaging transducer,” in *Proc. IEEE Ultrasonics Symp*., 1991, pp. 691-694.

[9] L. Gatzoulis, R. J. Watson, L. B. Jordan, S. D. Pye, T. Anderson, N. Uren, D. M. Salter, K. A. Fox, and W. N. McDicken, “Three-dimensional forward-viewing intravascular ultrasound imaging of human arteries in vitro,” *Ultrasound Med. Biol.*, vol. 27, no. 7, pp. 969-982, 2001.

[10] B. J. Kimura, V. Bhargava, W. Palinski, R. J. Russo, and A. N. DeMaria, “Distortion of intravascular ultrasound images because of nonuniform angular velocity of mechanical-type transducers,” *Amer. Heart J.*, vol. 132, no. 2, pp. 328-336, Aug. 1996.

[11] M. O’Donnell, M. J. Eberle, D. N. Stephens, J. L. Litzza, K. S. Vicente, and B. M. Shapo, “Synthetic Phased Arrays for Intraluminal Imaging of Coronary Arteries,” *IEEE Trans. Ultrason. Ferroelectr. Freq. Control*, vol. 44, no. 3, pp. 714-721, May 1997.

[12] G. Gurun, C. Tekes, J. Zahorian, T. Xu, S. Satir, M. Karaman, J. Hasler, and F. L. Degertekin, “Single-chip CMUT-on-CMOS front-end system for real-time volumetric IVUS and ICE imaging,” *IEEE Trans. Ultrason. Ferroelectr. Freq. Control*, vol. 61, no. 2, Feb. 2014.

[13] A. Nikoozadeh, I.O. Wygant, D. Lin, O. Oralkan, A. S. Ergun, D. N. Stephens, K. E. Thomenius, A. M. Dentigner, D. Wildes, G. Akopyan, K. Shivkumar, A. Mahajan, D. J. Sahn, and B. T. Khuri-Yakub, “Forward-looking intracardiac ultrasound imaging using a 1-D CMUT array

integrated with custom front-end electronics," *IEEE Trans. Ultrason. Ferroelectr. Freq. Control*, vol. 55, no. 12, Dec. 2008.

[14] J. Hamilton, T. Buma, M. Spisar, and M. O'Donnell, "High frequency optoacoustic arrays using etalon detection," *IEEE Trans. Ultrason. Ferroelectr. Freq. Control*, vol. 47, pp. 160–169, Jan. 2000.

[15] K. P. Köstli and P. C. Beard, "Two-dimensional photoacoustic imaging by use of Fourier-transform image reconstruction and a detector with an anisotropic response," *Appl. Opt*., vol. 42, no. 10, pp. 1899–1908, 2003.

[16] S. Ashkenazi, Y. Hou, T. Buma, and M. O'Donnell, "Optoacoustic imaging using thin polymer etalon," *Appl. Phys. Lett*., vol. 86, no. 13, art. no. 134102, 2005.

[17] C. Sheaff and S. Ashkenazi, "A fiber optic optoacoustic ultrasound sensor for photoacoustic endoscopy," in *Proc. IEEE Ultrasonics Symp*., 2010, pp. 2135-2138.

[18] L.V. Wang, *Photoacoustic Imaging and Spectroscopy*, Boca Raton, FL: CRC, 2009, pp. 223-238.

[19] P. C. Beard, F. Perennes, and T. N. Mills, "Transduction mechanisms of the Fabry-Perot polymer film sensing concept for wideband ultrasound detection," *IEEE Trans. Ultrason., Ferroelect., Freq. Contr*., vol. 46, pp. 1575-1582, Nov. 1999.

[20] R. M. White, "Generation of elastic waves by transient surface heating," *J. Appl. Phys.*, vol. 34, no. 12, pp. 3559-3567, 1963.

[21] R. J. von Gutfeld and R. L. Melcher, "20 MHz acoustic waves from pulsed thermoelastic expansions of constrained surfaces," *Appl. Phys. Lett.*, vol. 30, art. no. 257, 1977.

[22] A. M. Aindow, R. J. Dewhurst, D. A. Hutchins, and S. B. Palmer, "Laser-generated ultrasonic pulses at free metal surfaces," *J. Acoust. Soc. Am.*, vol. 69, no. 2, pp. 449-455, 1981.

[23] S. Fassbender, B. Hoffmann, and W. Arnold, "Efficient generation of acoustic pressure waves by short laser pulses," *Mat. Sci. Eng. A*, vol. 122, no. 1, pp. 37-41, 1989.

[24] X. Wang and X. Xu, "Thermoelastic wave induced by pulsed laser heating," *Appl. Phys. A*, vol. 73, pp. 107-114, 2001.

[25] B. R. Tittmann, R. S. Linebarger, and R. C. Addison Jr., "Laser-based ultrasonics on Gr/epoxy composite," *J. Nondestr. Eval.*, vol. 9, no. 4, pp. 229-238, 1990.

[26] E. Biagi, F. Margheri, and D. Menichelli, "Efficient laser-ultrasound generation by using heavily absorbing films as targets, " *IEEE Trans. Ultrason., Ferroelect., Freq. Contr.*, vol. 48, pp. 1669-1680, Nov. 2001.

[27] T. Buma, M. Spisar, and M. O'Donnell, "High-frequency ultrasound array element using thermoelastic expansion in an elastomeric film," *Appl. Phys. Lett.*, vol. 79, art. no. 548, 2001.

[28] T. Buma, M. Spisar, and M. O'Donnel, "A high-frequency, 2-D array element using thermoelastic expasion in PDMS," *IEEE Trans. Ultrason., Ferroelect., Freq. Contr.*, vol. 50, pp. 1161-1176, Sep. 2003.

[29] Y. Hou, J. Kim, S. Ashkenazi, M. O'Donnell, and J. Guo, "Optical generation of high frequency ultrasound using two-dimensional gold nanostructure," *Appl. Phys. Lett.*, vol. 89, art. no. 093901, 2006.

[30] H. W. Baac, J. G. Ok, H. J. Park, T. Ling, S. Chen, A. J. Hart, and L. J. Guo, "Carbon nanotube composite optoacoustic transmitters for strong and high frequency ultrasound generation," *Appl. Phys. Lett.*, vol. 97, art. no. 234104, 2010.

[31] Y. Hou, J. S. Kim, S. Ashkenazi, S. W. Huang, L. J. Guo, and M. O'Donnell, "Broadband all-optical ultrasound transducers," *Appl. Phys. Lett.*, vol. 91, art. no. 073507, 2007.

[32] Y. Hou, J. S. Kim, S. W. Huang, S. Ashkenazi, L. J. Guo, and M. O'Donnell. "Characterization of a broadband all-optical ultrasound transducer-from optical and acoustical properties to imaging," *IEEE Trans. Ultrason., Ferroelect., Freq. Contr.*, vol. 55, pp. 1867-1877, Aug. 2008.

[33] Y. Hou, S. Ashkenazi, S. W. Huang, and M. O'Donnell. "An integrated optoacoustic transducer combining etalon and black PDMS structures," *IEEE Trans. Ultrason., Ferroelect., Freq. Contr*., vol. 55, pp. 2719-2725, Dec. 2008.

[34] C. Sheaff and S. Ashkenazi, "A polyimide-etalon thin film structure for all-optical high-frequency ultrasound transduction," *IEEE Trans. Ultrason., Ferroelect., Freq. Contr*., vol. 59, no. 10, pp. 2254-2261, Oct. 2012.

[35] L. V. Wang, *Photoacoustic Imaging and Spectroscopy*, Boca Raton, FL: CRC, 2009, pp. 3-17.

[36] L. V. Wang and H. Wu, *Biomedical Optics: Principles and Imaging*, Hoboken, NJ: Wiley, 2007, pp. 283-319.

[37] Q. Shan, A. Kuhn, P.A. Payne, and R.J. Dewhurst, "Characterization of laser-ultrasound signals from an optical layer within a transparent fluid," *Ultrasonics*, vol. 34, no. 6, pp. 629-639, 1996.

[38] R. H. French, J. M. Rodriguez-Parada, M. K. Yang, R. A. Derryberry, M. F. Lemon, M. J. Brown, C. R. Haeger, S. L. Samuels, E. C. Romano, and R. E. Richardson, "Optical properties of materials for concentrator photovoltaic systems," *Photovolt. Spec. Conf.*, pp. 394-399, 2009.

[39] C. Sheaff and S. Ashkenazi, "Characterization of an improved polyimide-etalon all-optical transducer for high resolution imaging," *IEEE Trans. Ultrason., Ferroelect., Freq. Contr*., vol. 61, no. 7, pp. 1223-1232, Jul. 2014.

[40] J. Chalupský, J. Krzywinski, L. Juha, V. Hájková, J. Cihelka, T. Burian, L. Vysín, J. Gaudin, A. Gleeson, M. Jurek, A. R. Khorsand, D. Klinger, H. Wabnitz, R. Sobierajski, M. Störmer, K. Tiedtke, and S. Toleikis, "Spot size characterization of focused non-Gaussian x-ray laser beams," *Opt. Exp.*, vol. 18, no. 26, Dec. 2010.

[41] B. T. Cox and P. C. Beard, "The frequency-dependent directivity of a planar Fabry-Perot polymer film ultrasound sensor," *IEEE Trans. Ultrason., Ferroelect., Freq. Contr.*, vol. 54, no. 2, Feb. 2007.

[42] Ö. Oralkan, B. Bayram, G. G. Yaralioglu, A. S. Ergun, M. Kupnik, D. T. Yeh, I. O. Wygant, and B. T. Khuri-Yakub, “Experimental characterization of collapse-mode CMUT operation,” *IEEE Trans. Ultrason. Ferroelectr. Freq. Contr.*, vol. 53, no. 8, pp. 1513–1523, Aug. 2006.

[43] I. O. Wygant, “A comparison of CMUTs and piezoelectric transducer elements for 2D medical imaging based on conventional simulation models,” in *Proc. IEEE Ultrasonics Symp*., 2011, pp. 100–103.

[44] M. Kalms, S. Hellmers, P. Huke, and R. B. Bergmann, “Beam shaping using liquid crystal-on-silicon spatial light modulators for laser ultrasound generation,” *Optical Eng.*, vol. 53, no. 4, pp. 044110-1/-6, Apr. 2014.

[45] K. Piglmayer, E. Arenholz, C. Ortwein, N. Arnold, and D. Bäuerle, “Single-pulse ultraviolet laser-induced surface modification and ablation of polyimide,” *Appl. Phys. Lett*., vol. 73, no. 6, pp. 847-849, Aug. 1998.

[46] W. Yung, J. S. Lui, H. C. Man, and T. M. Yue, “355 nm Nd:YAG laser ablation of polyimide and its thermal effect,” *J. Mat. Proc. Tech*., vol. 101, no. 1-3, pp. 306-311, Apr. 2000.

[47] E. Z. Zhang and P. C. Beard, “A miniature all-optical photoacoustic imaging probe,” in *Proc. SPIE*, 2011, vol. 7899, no. 78991F.

[48] M. A. Tadayon, M. E. Baylor, and S. Ashkenazi, “Polymer Waveguide Fabry-Perot Resonator for High-Frequency Ultrasound Detection,” *IEEE Trans. Ultrason. Ferroelectr. Freq. Contr.*, Vol. 61 (2014), No.12.

[49] R. Cobbold, Foundations of Biomedical Ultrasound, New York, NY: Oxford, 2007, pp. 187.

[50] J. Jensen, S.I. Nikolov, K.L. Gammelmark, M.H. Pederson, “Synthetic aperture ultrasound imaging,” *Ultrasonics*, Vol. 44, pp. e5-e15, 2006.

[51] B. Furlong and S. Motakef, “Scanning lenses and systems,” CVI + Melles Griot.

[52] K. Nagai, “A new synthetic-aperture focusing method for ultrasonic B-scan imaging by the fourier transform,” *IEEE Trans. Ultrason. Ferroelectr. Freq. Contr.*, vol. 32, no. 4, pp. 531–536, Jul. 1985.

[53] C. Hoelen, F. De Mul, R. Pongers, and A. Dekker, "Three-dimensional photoacoustic imaging of blood vessels in tissue," *Opt. Lett.*, vol. 23, pp. 648-650, 1998.

[54] X. Wang, Y. Pang, G. Ku, X. Xie, G. Stoica and L. V. Wang, "Noninvasive laser-induced photoacoustic tomography for structural and functional in vivo imaging of the brain," *Nat. Biotechnol*., vol. 21, pp. 803-806, 2003.

[55] E. Z. Zhang, J. Laufer, and P. Beard, "Three dimensional photoacoustic imaging of vascular anatomy in small animals using an optical detection system," in *Proc. of SPIE Vol*, 2007, pp. 64370S-1.

[56] H. F. Zhang, K. Maslov, G. Stoica, and L. V. Wang, "Functional photoacoustic microscopy for high-resolution and noninvasive in vivo imaging," *Nat. Biotechnol*., vol. 24, pp. 848-851, 2006.

[57] J. Folkman, E. Merler, C. Abernathy and G. Williams, "Isolation of a tumor factor responsible for angiogenesis," *J. Exp. Med*., vol. 133, pp. 275, 1971.

[58] J. Holash, P. Maisonpierre, D. Compton, P. Boland, C. Alexander, D. Zagzag, G. Yancopoulos and S. Wiegand, "Vessel cooption, regression, and growth in tumors mediated by angiopoietins and VEGF," *Science*, vol. 284, pp. 1994, 1999.

[59] C. G. Willett, Y. Boucher, E. di Tomaso, D. G. Duda, L. L. Munn, R. T. Tong, D. C. Chung, D. V. Sahani, S. P. Kalva and S. V. Kozin, "Direct evidence that the VEGF-specific antibody bevacizumab has antivascular effects in human rectal cancer," *Nat. Med.*, vol. 10, pp. 145-147, 2004.

[60] D. M. McDonald and P. L. Choyke, "Imaging of angiogenesis: from microscope to clinic," *Nat. Med.,* vol. 9, pp. 713-725, 2003.

[61] M. Hockel, K. Schlenger, B. Aral, M. Mitze, U. Schaffer and P. Vaupel, "Association between tumor hypoxia and malignant progression in advanced cancer of the uterine cervix," *Cancer Res.,* vol. 56, pp. 4509, 1996.

[62] M. Quintero, N. Mackenzie and P. Brennan, "Hypoxia-inducible factor 1 (HIF-1) in cancer," *Euro. J. Surg.l Onc.*, vol. 30, pp. 465-468, 2004.

[63] L. B. Harrison, M. Chadha, R. J. Hill, K. Hu and D. Shasha, "Impact of tumor hypoxia and anemia on radiation therapy outcomes," *The Oncologist*, vol. 7, pp. 492, 2002.

[64] K. A. Krohn, J. M. Link and R. P. Mason, "Molecular imaging of hypoxia," *J. Nuc. Med*., vol. 49, pp. 129S, 2008.

[65] S. Ashkenazi, S. W. Huang, T. Horvath, Y. E. L. Koo and R. Kopelman, "Photoacoustic probing of fluorophore excited state lifetime with application to oxygen sensing," *J. Biomed. Opt*., vol. 13, pp. 034023, 2008.

[66] S. Ashkenazi, “Photoacoustic lifetime imaging of dissolved oxygen using methylene blue,” *J. Biomed. Opt*., vol. 15, no. 4, pp. 040501, 2010.

[67] J. M. Yang, K. Maslov, H. C. Yang, Q. Zhou, K. K. Shung and L. V. Wang, "Photoacoustic endoscopy," *Opt. Lett.,* vol. 34, pp. 1591-1593, 2009.

[68] J. M. Yang, K. Maslov, R. Chen, H. C. Yang, Q. Zhou, K. K. Shung and L. V. Wang, "Volumetric photoacoustic endoscopy of internal organs: A phantom and in situ study," in *Proceedings of SPIE*, 2010, pp. 75640D.

[69] J. J. Alcoz, C. Lee and H. Taylor, "Embedded fiber-optic Fabry-Perot ultrasound sensor," *IEEE Trans. Ultrason. Ferroelectr. Freq. Contr*, vol. 37, pp. 302-306, 1990.

[70] P. Beard and T. Mills, "Extrinsic optical-fiber ultrasound sensor using a thin polymer film as a low-finesse Fabry-Perot interferometer*," Appl. Opt*., vol. 35, pp. 663-675, 1996.

[71] P. C. Beard, A. M. Hurrell and T. N. Mills, "Characterization of a polymer film optical fiber hydrophone for use in the range 1 to 20 MHz: A comparison with PVDF needle and membrane hydrophones," *IEEE Trans. Ultrason. Ferroelectr. Freq. Contr.*, vol. 47, pp. 256-264, 2000.

[72] P. Morris, A. Hurrell, A. Shaw, E. Zhang and P. Beard, "A Fabry–Pérot fiber-optic ultrasonic hydrophone for the simultaneous measurement of temperature and acoustic pressure," *J. Acoust. Soc. Am*., vol. 125, pp. 3611, 2009.

[73] E. Biagi, S. Fontani, F. Francini, L. Masotti, and M. Pieraccini. "Photoacoustic generation: all-optical fibre transducers," In *Proc. IEEE Ultrasonics Symp.*, 1996, pp. 921-924.

[74] P. A. Fomitchov, A. K. Kromine, and S. Krishnaswamy. "Photoacoustic probes for nondestructive testing and biomedical applications." *Appl. Opt.,* vol. 41, no. 22, pp. 4451-4459, 2002.

[75] L. Belsito, E. Vannacci, F. Mancarella, M. Ferri, G. P. Veronese, E. Biagi, and A. Roncaglia, "Fabrication of fiber-optic broadband ultrasound emitters by micro-opto-mechanical technology," *J. of Micromech. Microeng*., vol. 24, no. 8, pp. 085003, 2014.

[76] R. J. Colchester, C. A. Mosse, D. S. Bhachu, J. C. Bear, C. J. Carmalt, I. Papakonstantinou, and A. E. Desjardins, "Laser-generated ultrasound with optical fibres using functionalised carbon nanotube composite coatings," *Appl. Phys. Lett*., vol. 104, no. 17, pp. 173502, 2014.

[77] *http://press.thorlabs.com/articles/video-rate-scanning-confocal-microscopy-and-microendoscopy/protocol/* (Video-rate Scanning Confocal Microscopy and Microendoscopy).

[78] *http://www.ceramoptec.com/filephotos/pdf/OptranUVWF.pdf* (CeramOptec Optran UV, Optran WF).

[79] Kubono, Atsushi, and Norimasa Okui. "Polymer thin films prepared by vapor deposition." *Prog. Polymer Sci*., vol. 19, no. 3, pp. 389-438, 1994.

[80] V. Malba, V. Liberman, and A. F. Bernhardt. "Vapor deposition polymerization of polyimide for microelectronic applications," *J. Vacuum Sci. Tech. A*, vol. 15, no. 3, pp. 844-849, 1997.

[81] J. P. González, A. Lamure, and F. Senocq, "Polyimide (PI) films by chemical vapor deposition (CVD): Novel design, experiments and characterization," *Surf. Coat. Tech*., vol. 201, no. 22, pp. 9437-9441, 2007.

[82] S. Q. Tran, "Method of forming a composite coating with particle materials that are readily dispersed in a sprayable polyimide solution," U.S. Patent No. 5,753,306. 19 May 1998.

[83] S. Q. Tran, "Method of forming a hot film sensor system on a model." U.S. Patent No. 5,789,020. 4 Aug. 1998.

[84] D. Vak, S. S. Kim, J. Jo, S. H. Oh, S. I. Na, J. Kim, and D. Y. Kim, "Fabrication of organic bulk heterojunction solar cells by a spray deposition method for low-cost power generation," *Appl. Phys. Lett*., vol. 91, no. 8, pp. 081102, 2007.

[85] R. Green, A. Morfa, A. J. Ferguson, N. Kopidakis, G. Rumbles, and S. E. Shaheen, "Performance of bulk heterojunction photovoltaic devices prepared by airbrush spray deposition," *Appl. Phys. Lett*., vol. 92, no. 3, pp. 033301, 2008.

[86] C. Girotto, B. P. Rand, J. Genoe, and P. Heremans, "Exploring spray coating as a deposition technique for the fabrication of solution-processed solar cells," *Sol. Ener. Mat. Solar Cells*, vol. 93, no. 4, pp. 454-458, 2009.

[87] G. Susanna, L. Salamandra, T. M. Brown, A. Di Carlo, F. Brunetti, and A. Reale, "Airbrush spray-coating of polymer bulk-heterojunction solar cells," *Sol. Ener. Mat. Sol. Cells*, vol. 95, no. 7, pp. 1775-1778, 2011.

[88] B. K. Yu, D. Vak, J. Jo, S. Na, S. S. Kim, M. K. Kim, and D. Y. Kim, "Factors to be considered in bulk heterojunction polymer solar cells fabricated by the spray process." *IEEE J. Sel. Top. Quan. Elec*., vol. 16, no. 6, pp. 1838-1846, 2010.

[89] M. Noebels, R. E. Cross, D. A. Evans, and C. E. Finlayson, "Characterization of spray-coating methods for conjugated polymer blend thin films," *J. Mat. Sci*., vol. 49, no. 12, pp. 4279-4287, 2014.

[90] *http://www.thorlabs.us/newgrouppage9.cfm?objectgroup_id=8013* (5-axis Kinematic Mount).

[91] T. Shiina, K. Noguchi, and T. Fukuchi, "Polarization-independent optical circulator for high accuracy Faraday depolarization lidar," *Appl. Opt*., vol. 51, no. 7, pp. 898-904, 2012.

[92] J. Li, A. Taylor, I. Papakonstantinou, E. Zhang, and P. Beard, "Highly sensitive optical microresonator sensors for photoacoustic imaging," In *Proc. SPIE BiOS*, 2014, pp. 89430C-89430C.

[93] P. C. Beard and T. N. Mills, "Miniature optical fibre ultrasonic hydrophone using a Fabry-Perot polymer film interferometer," *Elec. Lett.,* vol. 33, no. 9, pp. 801-803, 1997.

[94] F. Pérennès, P. C. Beard, and T. N. Mills, "Analysis of a low-finesse Fabry-Perot sensing interferometer illuminated by a multimode optical fiber," *Appl. Opt*., vol. 38, no. 34, pp. 7026-7034, 1999.

[95] M. Lamont and P. C. Beard, "2D imaging of ultrasound fields using CCD array to map output of Fabry-Perot polymer film sensor," *Elec. Lett*., vol. 42, no. 3, pp. 187-189, 2006.

[96] A. Meyer, S. Gspan, S. Bernet, and M. Ritsch-Marte, “Binary optoacoustic holography with a spatial light modulator,” *J. Appl. Phys*., vol. 96, no. 10, pp. 5886-5891, 2004.

[97] M. D. Brown, T. J. Allen, B. T. Cox, and B. E. Treeby. "Control of optically generated ultrasound fields using binary amplitude holograms," In *IEEE Ultrasonics Symp*., 2014, pp. 1037-1040.

[98] S. Sethuraman, J. H. Amirian, S. H. Litovsky, R. W. Smalling, and S. Y. Emelianov, “Spectroscopic intravascular photoacoustic imaging to differentiate atherosclerotic plaques,” *Opt. Exp.*, vol. 16, no. 5, pp. 3362-3367, Feb. 2008.